DISSECTING CYTOSKELETAL DYNAMICS WITH ACTIVE MICROPOST ARRAYS

by

Yu Shi

A dissertation submitted to The Johns Hopkins University in conformity with the requirements for the degree of Doctor of Philosophy.

Baltimore, Maryland

January 2020

Abstract

The ability of animal cells to migrate, change their shape, and respond to applied force is due to their actomyosin cytoskeleton: a dynamic, cross-linked network of actin protein filaments and myosin motors. The cytoskeleton is at the heart of critically important problems in biology and medicine related to animal cells' mechanical sensing and function. Despite its importance, how these cytoskeletal building blocks assemble to give rise to cells' mechanics and behavior remains poorly understood, and a satisfying physical understanding of the cytoskeleton's complex biophysics and mechanical properties has proven elusive.

To probe the dynamics of cellular actomyosin networks, I used active micropost array detectors (AMPADs). I measured cytoskeletal fluctuations and rheology in 3T3 fibroblasts with high precision and statistical power and characterized the fluctuations of cells' actomyosin cortex and stress-fiber network in detail. I found that both structures display power-law viscoelastic behavior and highly intermittent fluctuations with fat-tailed distributions of amplitudes. Notably, this motion in the cortex is dominated by occasional large, step-like displacement events, with a spatial extent of up to several micrometers. I expanded these measurements and analyses to 3T3 fibroblasts on multiple substrate stiffnesses, as well as to additional cell types. Surprisingly, despite variations in traction force, the underlying non-Gaussian fluctuations persist in all cases measured to date. Overall, these findings for the cortex suggest that cells' actomyosin components robustly self-organize into marginally stable, plastic networks that give cells their unique biomechanical properties.

As a part of a larger project which studies mechanical and electrical coupling between cardiac fibroblasts, cardiac myofibroblasts and cardiomyocytes, I have also used AMPADs to characterize mechanical properties of neonatal rat ventricular cardiac fibroblasts and their phenotypical myofibroblast variant which are present during wound healing processes. I found the traction force and the spreading area increased upon transformation from fibroblasts to myofibroblasts, observed intercellular mechanical coupling between cardiac myofibroblasts pairs, and quantified the increase in traction force during neonatal cardiomyocytes beating under external pacing. These preliminary data on the characterization of the dynamics of cardiac cells have shown that AMPADs have great potential for use in studying the mechanical coupling between cardiac cells.

Advisor: Daniel H. Reich

Acknowledgement

I would like to thank Dr. Daniel Reich for all his guidance and understanding and patience throughout the time we have worked together. He provided me both academic and non-academic advice and set a role model for me of being a scientist, for which I will eternally be grateful.

My fellow lab members Katherine Xiang, Shankar Sivarajan and Chen-yu Huang have been great friends and a pleasure to work with. My former colleagues Ruogang Zhao, Craig Copeland, Alan Liu, Fan Xu and Prasenjit Bose have all provided me with instrumental teachings, and valuable advice and insights along the way. I also would like to thank Geran Kostecki, Shoshana Das, Seungman Park, Steven Henry and Christopher Porter for their assistance and insightful discussions.

I am grateful to my collaborator, Dr. John Crocker at the University of Pennsylvania for his guidance on experiments and modeling aspects of my research, and Dr. Christopher Chen at Boston University, Dr. Leslie Tung at the Johns Hopkins Department of Biomedical Engineering and Dr. Yun Chen at the Johns Hopkins Department of Mechanical Engineering for their interdisciplinary guidance and for providing me with opportunities for unique and exciting research.

I would like to thank my parents and all my friends for their support and encouragement over the years. Finally, I would like to thank my fiancée Lin Bai for her endless patience and understanding.

Table of Contents

List of Tables

List of Figures

behavior ($\sim\tau^{\alpha}$, with $\alpha > 1$). Red and black dashed lines show τ ranges discussed below. The black trace is the MSD for a post not coupled to a cell, and the red trace shows the background due to fluctuations in cellular optical density (See 3.4). Heat maps of: (B), MSD exponent α (for 5 s $\leq \tau \leq$ 10 s), and (C), MSD amplitude at τ = 10 s for cell-adhered posts. Gray hexagons show posts not engaged with the cell for the full measurement interval. Gray circles indicate background posts. Posts with MSD traces in (A) are outlined in red in (B). (D) Classification of microposts according to traction force: maximum traction force < 2 nN ("cortical" posts with low traction force) in green; average traction force > 5 nN ("stress-fiber" posts with high traction force) in blue; remainder of posts in yellow. (E) Scatter plot of MSD magnitude at τ = 10 s vs. average traction force. (F) MSD magnitude at τ = 10 s vs. MSD exponent α for cortical and stress fiber posts (omitting middle case open circles in (E)). Standard errors for points in (E) and (F) are smaller than the symbol sizes. (G) Myosin inhibition reduces displacement fluctuations in cortical posts. Error bars in (G) show ±SD. Average MSD magnitude at τ = 10 s for control cells (25 cells), and for cells following treatment with blebbistatin (10 cells), Y27632 (11 cells), or ATP depletion (4 cells); significance via unpaired t-test. ** $p < 0.01$; *** $p < 0.001$. 47

Figure 3.5 Subtracted MSD and its logarithmic time derivative, illustrating the determination of the MSD exponent α for two microposts. (A), (D) Raw MSD traces showing fits (red lines) to determine the noise floor as described in the Methods. (B), (E) MSD traces MSD_{Sub} after subtracting the noise floor from the raw MSDs. (C), (F) Logarithmic time derivatives of MSD_{Sub}. The MSD exponent α and its uncertainty were obtained from the average of the logarithmic time derivative in the range 5 s $\leq \tau \leq$ 10 s.

phalloidin (green) and nuclei were stained with Hoechst (blue). (D) Distribution of MSD exponent α, (E) MSD magnitude at τ = 10 s, (F) vector map of average traction force together with classification of microposts according to traction force as in **Figure 3.4** and **Figure 3.8**, and (G) corresponding scatter plot of MSD magnitude vs. traction force for an untreated 3T3 fibroblast cell. Corresponding plots are shown for (H-K) cells treated with blebbistatin, (L-O) Y27632, and (P-S) ATP depletion. The maps of the distributions of MSD exponent (D, H, L, P), MSD magnitude (E, I, M, Q) and MSD magnitude vs. traction force (G, K, O, S) follow the same conventions and scales as described in **Figure 3.4**and **Figure 3.6**. The standard errors in G, K, O and S are smaller than the symbol sizes. After inhibition of myosin activity, the MSD exponents, MSD magnitudes and traction forces all decreased, and stress fiber posts were not found. Quantification of effects on cortical posts: (T) MSD exponent α measured in the range 5 s ≤ τ ≤ 10 s , (U) MSD magnitude at τ = 10 s (reproduced from **Figure 3.4** G) and (V) average traction force for untreated control cells (25 cells), and for cells following treatment with blebbistatin (10 cells), Y27632 (11 cells), or ATP depletion (4 cells); significance via unpaired t-test. ** $p < 0.01$; *** $p < 0.001$. Error bars in *T*, *U* and *V* show ±SD. All analysis was done based on videos with 90 s length. 55

Figure 3.10 Assessment of impact of fluctuations in cellular optical density on microposts' trajectories and MSDs based on cell-coupled microposts that exhibited 300 s time segments with very small maximum deflections (Δx, Δy < 15 nm) from the posts' resting positions, and correspondingly small maximum traction forces (< 0.24 nN). (A) Pink traces: MSDs for 53 such 300 s segments. Red trace: MSD averaged over all 159 such segments in our sample. Black trace: MSD of representative background micropost not coupled to a cell.

Figure 3.15 (A) Spread of MSDs calculated for a single stress fiber post over each of the six 300 s intervals in the 1,800 s measurement window. (B) Simulation showing spread in six MSDs for a Gaussian random walk over the same time interval (Reproduced from **Figure 3.14** B). (C), (D) $L_{MSD} = [MSD(\tau)]^{1/2}$ for τ = 20 s and 100 s for the data shown in *A* and *B,* respectively. (E) Distribution of the non-Gaussian parameter, α_2, computed over the full 1,800 s interval for stress fiber posts (N_{cells} = 13). The distribution at τ = 20 s (black dashed line) for an 18,000 step Gaussian random walk is also shown for comparison. Error bars were estimated as $1/N$ for each bin in the probability distributions..... 71

Figure 3.16. Anti-parallel micropost motions reveal cortical avalanche dynamics. (A), (B) Examples of strongly anti-correlated steps in the 2D trajectories of nearest neighbor micropost pairs. The black arrows indicate each post's overall direction of motion. The trajectories are color-coded to indicate time. Circles indicate the posts' resting positions. The relative positions of the posts in the pair and the two adjacent posts are shown, but their separations are not to scale. (C), (D) Displacements for the posts in the pairs in Panels A and B projected onto the line of centers; experiment (red curves) and error function fit (blue curve). The time t = 0 was set at the peak of the 1st derivative for the bottom trace. (E) Step profiles averaged over 12 contracting (blue) and 19 expanding pairs (red). Dashed red and blue lines show fits to error functions to extract average step durations $t_{contract}$ = 9.5 ± 0.2 s and t_{expand} = 8.8 ± 0.1 s, and average step heights $h_{contract}$ = 8.2 ± 0.1 nm and h_{expand} = 8.8 ± 0.2 nm. The ratio of step sizes was restricted to the range $0.7 < h_2/h_1 < 1.4$, with both h_1 and $h_2 > 6$ nm. Dashed black line shows calculated viscoelastic creep response to a step stress at t = 0, with deflection $\propto t^{\beta}$, based on measured cell rheology (**Figure 3.1** E). (F) Scatter plot of step durations for pairs of posts, pooling the contracting and expanding

Chapter 1 : Introduction and Overview

1.1 Mechanotransduction

Mechanical forces are known for their role in regulating many physiologic and pathologic processes [1]. For instance, mesenchymal stem cells growing on different substrate stiffness will differentiate into different tissue types ranging from stiff bone tissues to soft neuron tissues [2], an example of an effect known as rigidity sensing. Such phenomena motivate scientists to study how mechanical forces are transduced into biochemical and functional responses.

Over the last few decades, enabled by developments in microscopy and microfabrication techniques, there has been increasing focus on understanding the process of how mechanical stimuli are converted into biological signals that guide cellular behavior, also known as mechanotransduction. Recently, studies have shown that cellular contractile forces generated by the cellular cytoskeletal networks are involved in regulating many fundamental cell functions such as proliferation, differentiation and migration [2-4]. These results suggest the importance of the cytoskeleton in regulating cellular behavior and imply a broader role for mechanotransduction in biology. Although the force generation mechanisms of cytoskeletal networks have been well studied, the detailed mechanism connecting the force generation machinery at the molecular scale to the cellular

scale is still not well understood and a combination of biology, engineering, and physics will be required to provide new insights into this field.

1.2 Actomyosin Networks as Active Matter

The cytoskeleton has long been recognized as a remarkable active material [5-7] with unusual viscoelastic behavior [8-10], and the seeming ability to change rapidly from fluid to solid and to adjust its stiffness over a wide range. In this section, I will introduce the idea of active matter systems and their characteristics, as well as discuss some of the findings from studying the cytoskeleton as an active matter system.

1.2.1 Active matter systems

In physics, self-propelled systems out of equilibrium are called active matter [5]. One of the characteristics of such systems is that their constituents are made of self-driven particles, which are capable of converting stored or environmental free energy such as ATP into particle motion [11]. Another characteristic of most of the active matter systems is that the direction of self-propelled motions of individual particles is determined in part by the self-orientation of the particle itself, instead of by external fields [12]. As a result of these unique characteristics, active matter systems typically possess highly correlated collective motion and internally generated mechanical stress.

A defining difference between active matter systems and other out of equilibrium systems is that each particle consumes energy to generate local force instead of taking energy injected externally. For instance, a bacterial swarm can be considered an active matter system, while colloids under external shear are not. Given the nature of their self-

driven motions, many biological systems are considered as archetypal examples of active matter systems, such as the cytoskeleton of living cells, bacterial suspensions [13], cell layers [14], and terrestrial, aquatic and aerial flocks. Active matter systems exhibit a wide variety of interesting phenomena, including qualitatively different emerging structures from individual constituents [15], anomalous fluctuational statistics [16], non-equilibrium order–disorder transitions [17], mesoscale self-organization [18] and unusual mechanical and rheological properties [19].

1.2.2 The cytoskeleton as active matter

The cellular cytoskeleton is a complex, dynamical structure. It is a network of semi-flexible biopolymers that supports the internal structural integrity of a cell. The cytoskeleton is constructed of three main components: intermediate filaments, microtubules and actin filaments. Intermediate filaments are stable, rope-like fibers with many long strands twisted together, typically with diameters of 10 nm and can grow up to more than hundreds of nanometers. They are distributed throughout the cytoplasm and provide mechanical supports for the cell. They can also form a meshwork called the nuclear lamina that supports the nucleus. Microtubules are typically 25 nm in diameter, are built from tubulin dimer subunits, and form tube-like structures. They can grow as long as 50 μm, are stiff, and are responsible for providing trafficking pathways for organelle transportation and for forming structures such as the centrosome during cell division. Actin filaments are flexible polymers with diameters of about 7 nm. They are made from G-actin (globular) proteins which assemble into a helical structure. Actin filaments form a variety of networks, including the cell cortex, which is a thin network underneath the plasma

membrane (actin cortex) that controls cell morphogenesis [20], and stress fibers, which are bundles made from multiple filaments that play an important role in cell adhesion and migration [21]. Both actin filaments and microtubules are highly dynamic and undergo disassembly and polymerization, and both have associated motor protein (kinesin and dynein for microtubules and myosin for actin filaments). In non-muscle cells, the actomyosin network is formed by F-actin (filamentous) bundles and myosin motors [22]. There are mainly three kinds of myosin with different functions in the actomyosin network of non-muscle cells: myosin I, myosin II, and myosin V. By consuming ATP, myosin I and V are involved in intracellular vesicle transport, while myosin II motors can apply traction force along actin contractile bundles. Usually, non-muscle myosin II A (NM2A) and II B (NM2B) are the most dominant myosin II isoforms [23]. One of the differences between these isoforms is their binding/unbinding rate: NM2A is faster and is mostly involved in contractile processes such as movement or remodeling of the actin cytoskeleton, while NM2B is slower and is typically involved in maintaining the tension of the cytoskeletal network. Since the primary focus of this thesis is on force generation within actomyosin networks, I will only refer to myosin II when mentioning myosin later on.

The actomyosin network can be viewed as an active matter system, and has been studied both in vitro [24-27] and in cells [28-32] experimentally and theoretically. In vitro studies provide a simplified model of the cellular actomyosin network that allows a more controlled way for understanding the underlying physics, while in vivo studies throw light on its mechanism in the context of cell biology. These studies reveal that the self-assembled structure of the actomyosin network and its self-propelled contractility are results of interplay between F-actin, myosin motors and actin binding proteins. For instance, Bendix

et al. [25] reconstructed an actomyosin network by mixing F-actin, muscle myosin II motors, and α-actinin cross-linkers, and reproduced bundled actin networks with various pore sizes. They also found that the contractility of the network is strongly regulated by myosin motor activity and the crosslinkers' density and binding affinity. Experimental approaches to illustrate these effects require the capability of measuring the dynamical fluctuations as well as the local network rheology with high spatial and temporal resolution. These techniques, known as microrheology, will be explained in the next section.

1.3 Probing Intracellular Dynamics with Microrheology

Rheology studies soft materials' ability to deform under external mechanical stress, deformation or flow. Typically, rheology is used to study solids or bulk liquids, such as gels, polymer solutions and colloidal suspensions, by applying sinusoidal deformation at a given frequency and measuring their response. The ratio of applied stress to deformation strain is defined as a material's shear modulus $G(\omega)$. The frequency dependences of $G(\omega)$ for conventional materials are simple: for a solid, it is independent of frequency and for a liquid, it is proportional to frequency. For materials with more complex microstructures, it will display viscoelastic behavior, which lies between that of a solid and a liquid and possesses more complicated frequency dependence. The origin of such behavior can arise from complex, time-dependent response of materials' microstructure under mechanical stress [33, 34].

However, studying the complicated viscoelasticity of intracellular mechanical properties requires a technique that can explore properties at the micrometer scale. One approach to do this is known as microrheology. The general principal behind microrheology is to track the motion of micrometer to nanometer sized probe particles embedded in the materials under some driving force, and then infer the local mechanical properties of the materials from the particles' motion. Microrheology has the advantage over traditional rheology of extracting heterogeneity of the measured material and enabling high frequency measurements [35, 36]. If an external force is applied to the particles, such as through a magnetic field or optical tweezers, then it is called active microrheology, whereas if the technique just monitors particle motions due to internal fluctuations, then it is known as passive microrheology. I will discuss the two techniques in detail for the rest of this section.

1.3.1 Passive microrheology

To introduce passive microrheology, it is convenient to think of Brownian motion. For particles in a viscous liquid driven by thermal fluctuations, their trajectories will follow a random walk, also known as Brownian motion. One of the most well-known ways to characterize dynamical trajectories is to calculate their mean square displacement (MSD), defined as $|\Delta r^2(\tau)| = <(\mathbf{r}(t+\tau) - r(t))^2>$, where **r**(t+τ) - **r**(t) is the displacement over lag time τ at time t. For particles doing random walks in three dimensions, their MSDs can be written as $|\Delta r^2(\tau)| = 6D\tau$, where D is the diffusion coefficient. In a fluid, the Stokes-Einstein equation $D = \frac{kT}{6\pi\eta a}$, where kT is the thermal energy, η is the viscosity of the

liquid, and a is the particle diameter [37], relates D to the fluid's viscosity. Following this idea, by observing the trajectories of injected micro-particles, one can measure a material's rheology.

For viscoelastic materials, the modulus G is a complex number and is also frequency dependent, and can be written as $G^*(\omega) = G'(\omega) + iG''(\omega)$, where G'(ω) and G''(ω) are the materials' storage and loss modulus, respectively. Following the relationship between modulus and viscosity, $G^*(\omega) = i\omega\eta^*(\omega)$, the complex viscosity can be written as $\eta^*(\omega) = \eta'(\omega) - i\eta''(\omega)$, with η'(ω) and η''(ω) corresponding to the material's loss and storage moduli G'(ω) and G''(ω). In practice, one can use a generalized Stokes-Einstein equation to extract the frequency dependence of materials' modulus $G(\omega)$ from passive microrheology measurements [38].

Intracellular microrheology is a more complex scenario, since the system is out of equilibrium, and non-thermal forces are involved. Under such conditions, the generalized Stokes-Einstein equation can no longer be used to extract cellular rheology properties. None the less, numerous passive microrheology measurements have been performed on various cell types [9, 30, 31]. These studies report that trajectories of tracer particles show a mean square displacement that is diffusive to super diffusive ($|\Delta r^2(\tau)| \propto \tau^\alpha$ where α >1), indicating the influence of non-thermal driving forces. In principal, since the probing particles are propelled by internal generated non-thermal forces, their trajectories will carry information about those forces. However, one needs to know the material's modulus to carry out the calculation, which cannot be measured by passive microrheology alone. Therefore, an alternative approach to measure cellular rheology that will not be influenced by cellular internal forces is needed.

1.3.2 Active microrheology

Active microrheology provides an approach to measure a material's rheology independent of internal non-thermal forces. The term "active" comes from external actuation of the probing particle. In active microrheology, a material's mechanical properties are determined by the response of these particles under external driving.

Over the last two decades, a large number of approaches to perform active microrheology of cells over a wide range of frequencies have emerged, including magnetic twisting cytometry [39], optical tweezers [30, 40], atomic force microscopy [41-44] and magnetic tweezers [45]. These studies reported that the cellular modulus can be well described by a sum of two power laws [31]:

$$G'(\omega) = A\cos(\pi\beta/2)\omega^{\beta} + B\cos(3\pi/8)\omega^{3/4}$$
$$G''(\omega) = A\sin(\pi\beta/2)\omega^{\beta} + B\sin(3\pi/8)\omega^{3/4}$$
$$\left|G^*(\omega)\right|^2 = G'(\omega)^2 + G''(\omega)^2.$$

Despite the qualitative similarity, the actual quantities vary significantly, as β ranges from 0.1 to 0.3, and the transition frequency between the two power laws as well as the modulus magnitude varies over orders of magnitude. This variation depends on cell types, probing particles and methods, as these factors can lead to different subcellular architecture being probed. By comparing several cell rheology experiments, D. Hoffman et al. [46] pointed out that the rheology exponent β at low frequencies falls into two narrow value ranges: β_2 = 0.13-0.17 for externally attached probes (magnetic twisting cytometry) and β_1 = 0.24-0.29 for internally injected probes (laser tracking microrheology) for the same population

of cultured epithelial cells. This is considered to be evidence showing that different microrheology approaches probe mechanically distinct subcellular structures.

1.4 Models for Understanding Cellular Dynamics

Early attempts to explain these phenomena drew on analogies with other systems, such as the sol-gel transition [47, 48], tensegrity architecture [49, 50], and the soft-glassy-rheology model of materials such as foams and emulsions [51, 52]. A new approach has sought to derive the cytoskeleton's mechanics from the physics of polymer networks [53] and the activity of embedded molecular motors. Here I am going to talk about one model in each approach that is most relevant to the scope of this thesis.

1.4.1 The Soft Glassy Rheology (SGR) Model

The SGR model is a phenomenological model that captures the dynamical properties of a class of soft metastable materials, such as foams, emulsions, slurries etc. The constituents of these materials are densely packed, which results in energy barriers orders of magnitude higher than the thermal energy. Therefore, without an external energy source, stress relaxation in these materials will be similar to such processes in glasses. When an external energy source is present, relaxation to equilibrium is possible but strongly hindered, therefore causing the system's energy landscape to be fractal. Thus, a common feature of these materials is that their microscopic constituents show "run and tumble" motion, which results in super-diffusive motion of the constituent particles. The

plastic deformations arising from the system's rearrangement can also yield power-law rheology [54].

In 2001, Fabry et al. [8] showed through magnetic twisting cytometry (MTC) that cells also possess power law rheology. Such phenomena were later found in other cell types through other active microrheology approaches [30, 55-57]. Although the measured modulus and power-law rheology exponents varied with methods, cell types and probes, the power-law dependence with frequency persists. Since then, numerous other phenomena found in soft glassy materials have been observed in cells, such as super-diffusive tracer fluctuations, dynamical heterogeneity, physical aging and shear-induced rejuvenation [8, 30, 38, 55, 58, 59]. However, one of the discrepancies between the soft glassy rheology model and cells is that the soft glassy rheology model predicts strain softening, which means that materials soften under the application of large forces, whereas strain stiffening is observed in cells [46].

1.4.2 Active Gel Model

Recently, an in-vitro cytoskeleton network consisting of purified actin, filamin and externally applied stress was created to reproduce phenomena similar to that is observed in cells [60]. Specifically, it shows weak power-law rheology, strain stiffening of the network modulus and a link between cellular rheology, applied stress and rheological frequency response. This bottom-up way of understanding actomyosin networks provided an inspiration for construction of the active gel model [61].

The active gel model starts by considering actin filaments and crosslinkers forming a viscoelastic gel [62, 63], with myosin motors providing "prestress" [49, 50] that stiffens the network. Myosin minifilaments' random, uncorrelated binding and unbinding [30, 38, 60, 64] would then lead to the fluctuations observed in these networks. The model also assumes the myosin motors' contraction follows a step function, where a constant force is engaged over a certain time τ_p, and then released, and that τ_p follows a Boltzmann distribution, which will decay exponentially with a characteristic persistence timescale τ_p^*. The Fourier transform of such an ensemble results in a force power spectrum $\left\langle F^2(\omega)\right\rangle \propto \frac{1}{1+(\omega\tau_p^*)^2}$, which decreases with frequency as ω^{-2} at high frequency and reaches a plateau at lower frequency. When combining with the measured cellular rheology $G(\omega)=\omega^{\beta}$, and the generalized Hooke's law $\Delta X(\omega)=F(\omega)/G(\omega)$, the active gel model also predicts that the MSDs of fluctuational motion will follow $\left\langle \Delta X^2(\tau)\right\rangle \propto \tau^{1+2\beta}$, which will be super-diffusive, consistent with experiments, as described above.

Despite its successes, however, the active gel model predicts a power-law viscoelasticity with an exponent of 0.75 based on semiflexible polymer networks [65], which does not correctly predict the observed power-law viscoelasticity of cells at lower frequency [8, 9, 31, 42, 66], and does not naturally account for the observed highly heterogeneous nature of intracellular fluctuations.

1.5 Avalanches and Cytoquakes

As discussed in the last section, the SGR model revealed similar dynamics between the cellular cytoskeleton and soft glassy materials, such as non-diffusive motion and power law rheology. In a recent simulation work on model foams, Hwang et al. [54] connected such phenomena with a fractal energy landscape of these systems. Interestingly, they also found that energy released during system reconfigurations followed a "fat-tailed" power law distribution.

In soft matter physics, systems with such power-law distributed sizes of rearrangements are called avalanches, in analogy to avalanches in snow and in sand piles. Size can refer to a variety of measurements of the systems' rearrangements, such as amplitude, spatial extent, energy dissipation, etc. For instance, the energy released during avalanches in sand piles follows a power-law tail [67]. Another example is in earthquakes, which share similar dynamical properties with avalanche systems, and where the distribution of earthquake magnitudes follows a power-law, which is known as Gutenberg-Richter Law [68]. In avalanche systems, the constituents are considered to be self-organized into a marginally stable state, where local disturbances can cause cascades of rearrangements, until a new stable state is reached.

Surprisingly, such phenomena were also found in the cytoskeleton. Alencar et al [69] found that displacements of single microbeads on the dorsal surface of smooth muscle cells follow a power-law distribution, similar to avalanche systems. They also found that large displacements showed temporal correlations resembling aftershocks in earthquakes described by Omori's law. Based on such similarities, they named such phenomena

"cytoquakes". This study [69] provides a new aspect of understanding fluctuations of cytoskeleton. One of the main results of this thesis is experimentally characterizing the spatiotemporal dynamics of such avalanche phenomena in cells.

1.6 Active Micropost Array Detectors and Experimental Overview

Over the last few decades, microfabrication has been widely used to probe mechanical properties of biomaterials. Bio-compatible substrates with different geometries have been developed to probe mechanotransduction in cells at various scales. Two of the most well-developed techniques to probe cellular scale mechanics are traction force microscopy (TFM) [70] and micropost array detectors (MPADs) [71, 72]. For the scope of this thesis, I will mainly introduce MPADs, their past applications, and explain why I choose them to measure cellular passive and active microrheology.

A micropost array detector consists of an array of polydimethylsiloxane (PDMS) micrometer-scale pillars, which are fabricated through replica molding. The microposts' tips are coated with fibronectin through contact microprinting, which enables the microposts to couple directly to the cellular cytoskeleton through focal adhesions (**Figure 1.1** when cells are cultured on the micropost arrays. Through beam bending theory, the microposts can be modeled as simple springs under small deflections [71, 72]. This allows one to map out a cell's traction force field by measuring the microposts' deflections from their resting positions. More recently, Sniadecki et al. [73] embedded magnetic nanowires

into the microposts to enable external actuation. Through applying a step magnetic field, they were able to exert external force stimuli to measure the cellular mechanical response.

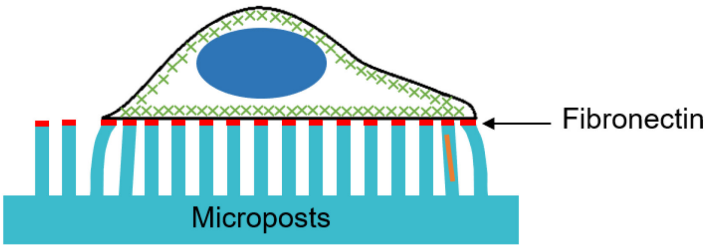

Figure 1.1 Schematics of cells on micropost array coated with fibronectin.

In TFM, on the other hand, one embeds tracer microbeads within a bulk substrate, and then probes cellular traction forces by measuring the beads' displacements [70]. The displacement field of the beads is then inversely converted into the traction force field of the cells. Since the tracers are affected non-locally, it is mathematically more complicated than the conversion between displacement and traction force in MPADs. Both TFM and MPADs have their own advantages: TFM allows cells to grow on a continuous substrate, while MPADs form a lattice of probes underneath cell and guarantee the independence between neighboring posts.

In this thesis, instead of using MPADs for measuring static cellular traction force, I sought to develop a system that can probe both cellular passive and active microrheology using active micropost array detectors (AMPADs), which are MPADs with embedded magnetic nanowires. Microposts with nanowires were actuated by a dual magnetic tweezer system to measure local cellular rheology while all the microposts served as probes for

measuring cellular fluctuations at high spatial and temporal resolution. Compared with other methodologies for performing microrheology, I choose AMPADs for the two following reasons: first, compared with other active microrheology techniques, AMPADs have the advantage of controlled coupling to cellular actomyosin networks via focal adhesions since the microposts' tips were coated with fibronectin; second, AMPADs provide mapping of cytoskeletal fluctuations of different subcellular architectures with high spatial resolution. Moreover, the choice of AMPADs over TFM is because the independent nature of the micropost probes allows one to study their correlations, and the capability of embedding magnetic nanowires inside the microposts allows one to perform active and passive microrheology with the same system.

1.7 Thesis Outline

Chapter 2 describes the main fabrication methods for producing and functionalizing magnetic micropost array detectors, and cell culturing and imaging methods for performing passive and active microrheology. Chapter 3 presents the data, analysis processes, results and interpretations for a study of fluctuations in actomyosin networks of 3T3 fibroblast cells on active micropost array detectors. Chapter 4 expands the study in Chapter 3 to different cell types and substrate stiffnesses. Chapter 5 shows the results from studying the actin cortical "avalanches" presented in Chapter 3 with nanometer-sized posts to reveal more detailed spatial information. Chapter 6 presents results on the dynamics and cell-cell interactions of cardiac fibroblasts, cardiac myofibroblasts, and cardiomyocytes derived from neonatal rats. Chapter 7 provides a summary and discussion of the whole dissertation.

Chapter 2 Methods and Techniques

2.1 Introduction

In this Chapter, I describe the experimental and fabrication techniques that were utilized to fabricate magnetic micropillar arrays and perform passive and active microrheology measurements. Magnetic nanowires were fabricated using electrodeposition and magnetic micropost arrays were fabricated by replica molding. Passive microrheology was performed using bright-field imaging at up to 100 frames per second and active microrheology was performed using magnetic tweezers. Images were analyzed via particle tracking and digital lock-in techniques to extract trajectories of the microposts' displacements. I will also describe cell culturing and staining techniques at the end of this chapter.

2.2 Magnetic micropost array fabrication

In this section, I describe protocols for fabrication of magnetic nanowires, fabrication of micropillar molds from masters, how to embed magnetic nanowires into micropillar arrays and how to functionalize the microposts' surfaces.

2.2.1 Magnetic nanowire fabrication

Nickel nanowires were fabricated via electrodeposition in nanoporous templates [74] (Whatman Nuclepore), using techniques described previously [75]. Briefly, the templates were 50 μm thick alumina filter membranes with pore diameters of 0.37 μm. Templates were first sputtered with a layer of copper to make them into working electrodes. A 5 μm layer of copper was first deposited into the pores to fill the branches in the pores near the ends, so that the desired metal, nickel, could later be deposited in the center of the template and have a consistent diameter. The height of nickel was 5 μm, so that the nanowires would fit into the microposts. After the electrodeposition, the sputtered copper layer as well as the deposited copper at the end of the template were removed with copper etching solution composed of 33.3 g/L $CuCl_2$ and 1 M HCl. The alumina template was then dissolved in 0.5 M KOH in a test tube for 4-6 hours. Magnetic nanowires were held by a magnet attached to the side of the tube while the KOH was replenished. The nanowires remained in KOH for another 4-6 hours to complete the template removal. In the end, the KOH solution was removed, and the nickel nanowires were stored in ethanol solution. The nanowires had lengths of 5 μm, diameters of 370 nm, with 10% uncertainty in each dimension and average low-field magnetic moments of $\mu = 0.15$ pA m^2, aligned along their long axes [76, 77].

2.2.2 Micropost mold fabrication

Microposts array molds were fabricated using SU-8 master templates provided by Dr. Christopher Chen's group at Boston University [78] and Dr. Jianping Fu at the University

of Michigan [79]. PDMS was mixed with curing agent at the ratio of 10:1 and then degassed by centrifuging at 10^4 ms^{-2} for 3 minutes. 30-50 mL of PDMS were cast into micropost masters in a 50 mm square polystyrene weighing dish (Southern Labware). The PDMS was degassed again with a vacuum desiccator for 20 minutes to remove air bubbles produced during casting and baked in an oven at 70 °C overnight. The cured molds were peeled off from the master. To make the molds' surface hydrophilic, they were treated with oxygen plasma under a pressure of 450 mTorr at 100 W for 90 s. The molds were moved to a vacuum desiccator with a few drops of tridecafluoroctyltrichlorosilane on a cover glass. The molds were left under vacuum (P = 25 Torr) for 12 hours after which time these were ready to use. This "silanization" process formed a layer of silanes on the molds to facilitate the removal of micropost arrays from the mold after casting.

2.2.3 Non-magnetic micropost array fabrication

22 mm x 22 mm cover glasses were ultraviolet (UV) ozone treated for 7 minutes to oxidize the surface and promote bonding to PDMS. PDMS was mixed with curing agent at the ratio of 10:1 then degassed by centrifuging at 10^4 ms^{-2} for 3 minutes. A drop of degassed PDMS was added to the top of the cover glass, and a micropost mold was inverted onto the PDMS drop. Cover glasses were baked in an oven at 70 °C overnight to allow the PDMS to cure. The molds were then peeled off from the cover glasses in 100% ethanol.

Under small deflections (less than the post diameter) [80], PDMS microposts' effective spring constant follows beam bending theory as $k = \frac{3E\pi d^4}{64L^3}$, where E is the Young's modulus of the material, d is the post's diameter and L is the post's height.

Therefore, the spring constant of the microposts can be modified by using molds with different post heights. (**Table 2.1**, **Table 2.2**). The silicon masters have < 1% variation in the micropost diameter d [78], leading to an estimate of ≤ 4% variation in k, as $k \propto d^4$ from elementary beam bending theory.

Wafer #	Post Height (μm)	Spring Constant (nN/ μm)
4	5.7	22.3
5	6.1	18.2
6	6.4	15.7
7	7.1	11.5
10	9.1	5.5

Table 2.1 Dimension and spring constant of 1.83 μm diameter microposts.

Wafer #	Post Height (μm)	Spring Constant (nN/ μm)
2	2.48	9.9
3	3.46	3.6
5	4.77	1.4

Table 2.2 Dimension and spring constant of 0.8 μm diameter microposts.

2.2.4 Fabrication of magnetic microposts

A magnetic nanowire solution (10^6 /mL in ethanol) was sonicated for 5 minutes and then vortexed for a few seconds to prevent the nanowires from aggregating. 30 μl of nanowire solution was deposited for each mold. A rare-earth bar magnet was applied underneath the mold to draw the nanowires down into the holes in the mold. The nanowire solution drop was left to evaporate for 20 – 30 minutes to prevent the nanowires from flowing out of the holes again before another drop was added. In total, 180 μL of nanowire

solution was added onto each mold, and then the molds were left on the magnet for 30 minutes to allow the ethanol to completely evaporate.

PDMS was poured over the negative molds and a UV ozone-treated cover glass was added on top and pressed against the mold slightly. The molds were degassed in a vacuum desiccator for 5 minutes while remaining on top of the magnets. The substrates were baked at 65 °C on a hot plate for 1 hour with the bar magnets underneath, and then flipped with the cover glass on the bottom and baked at 70 °C overnight in an oven (without magnets). The molds were peeled from the substrates in 100% ethanol, leaving the magnetic micropost arrays on the cover glasses.

2.2.5 Functionalization of micropost arrays

PDMS was mixed with curing agent at the ratio of 30:1 and cast onto a silicon wafer to fabricate stamps with flat surfaces. The stamps were sonicated in 100% ethanol for 5 minutes to clean the surface every time before use and then blown dry with nitrogen gas. 100 µL of 50 µg/mL fibronectin solution was added on top of each stamp. A pipette tip was used to spread out the solution evenly across the stamp's surface. Stamps were left to absorb fibronectin for 1 hour and then washed with DI water twice to remove unabsorbed fibronectin. The stamps were blown dry with nitrogen gas after which time these were ready to be used.

Once wetted, micropost arrays could not be left to dry since surface tension from evaporating liquids is strong enough to collapse the microposts. Because the functionalization process requires dried substrates, the microposts were dried with a critical point dryer as described previously [75]. Excess PDMS around the micropost arrays was

cut off to allow full contact between the stamps and the substrates. The substrates were then UV ozone treated for 7 minutes in order to activate their surface. Stamps with fibronectin were pressed gently against the substrates and submerged in 100 % ethanol for sterilization. The stamps were peeled gently with a tweezer and released from the substrates. The substrates were washed with 70% ethanol and DI water 3 times and then transferred into 0.2% W/V Pluronics F-127 for 30 minutes. This process blocked PDMS regions not coated with fibronectin, so that cells would only adhere to the top surfaces of the microposts. Finally, the microposts were washed with DI water twice and stored in phosphate-buffered saline (PBS) at 4 °C.

2.3 Imaging for passive microrheology

In this section, I describe the process of seeding cells on microposts and how to optimize the microscope for passive microrheology imaging. I will also briefly introduce the process for tracking microposts' trajectories.

2.3.1 Imaging setup for micropost arrays

Measurements of the 1.83 μm diameter microposts' motion were made on a Nikon TE-2000E inverted microscope, using a 40x, NA = 0.6, extra-long working distance air objective (Nikon Plan Fluor). When imaging the 0.8 μm diameter microposts' motion, an additional 1.5x magnifier was applied. Illumination was provided via a stock 100 W halogen illuminator and a long-working distance condenser with NA = 0.52. Bright field movies were recorded with 4.5 ms exposure time to avoid auto-correlation between

neighboring fames at sampling frequencies up to 100 frames/s with a Prosilica GX-1050 CCD camera (Allied Vision Technologies) using the StreamPix software suite (Norpix). For optimum resolution of the microposts' positions, the condenser aperture was maximized and the maximum illuminator intensity achievable without saturating the camera was applied. The camera's digital gain was turned off to minimize camera noise. To enable these high illumination intensities without affecting cell viability, ultraviolet (UV) (Edmund Optics #64-667) and infrared (Edmund Optics #47-303) filters were used to restrict the incident light to the wavelength range 425 nm $< \lambda <$ 700 nm. The microscope's built-in green interference filter (GIF) was also applied. Cell viability was tested with 3T3 fibroblasts, which were found to remain proliferative following 18 hours exposure to our experimental observation conditions.

To avoid focus drift caused by thermal fluctuations and to maintain cell viability for long-term imaging, an on-stage incubator and heating plate were used to keep the culture dish and its surroundings at 37 °C. Another rectangular on-stage environmental control chamber was used and filled with 5% premixed CO_2 gas at 200 cm^3/min influx (**Figure 2.1**). We removed air bubbles underneath the substrates by pressing them with a tweezer to minimize the substrates' drift and then allowed them to stabilize for 30 minutes in the on-stage incubator prior to imaging. (See Appendix for a more detailed protocol.)

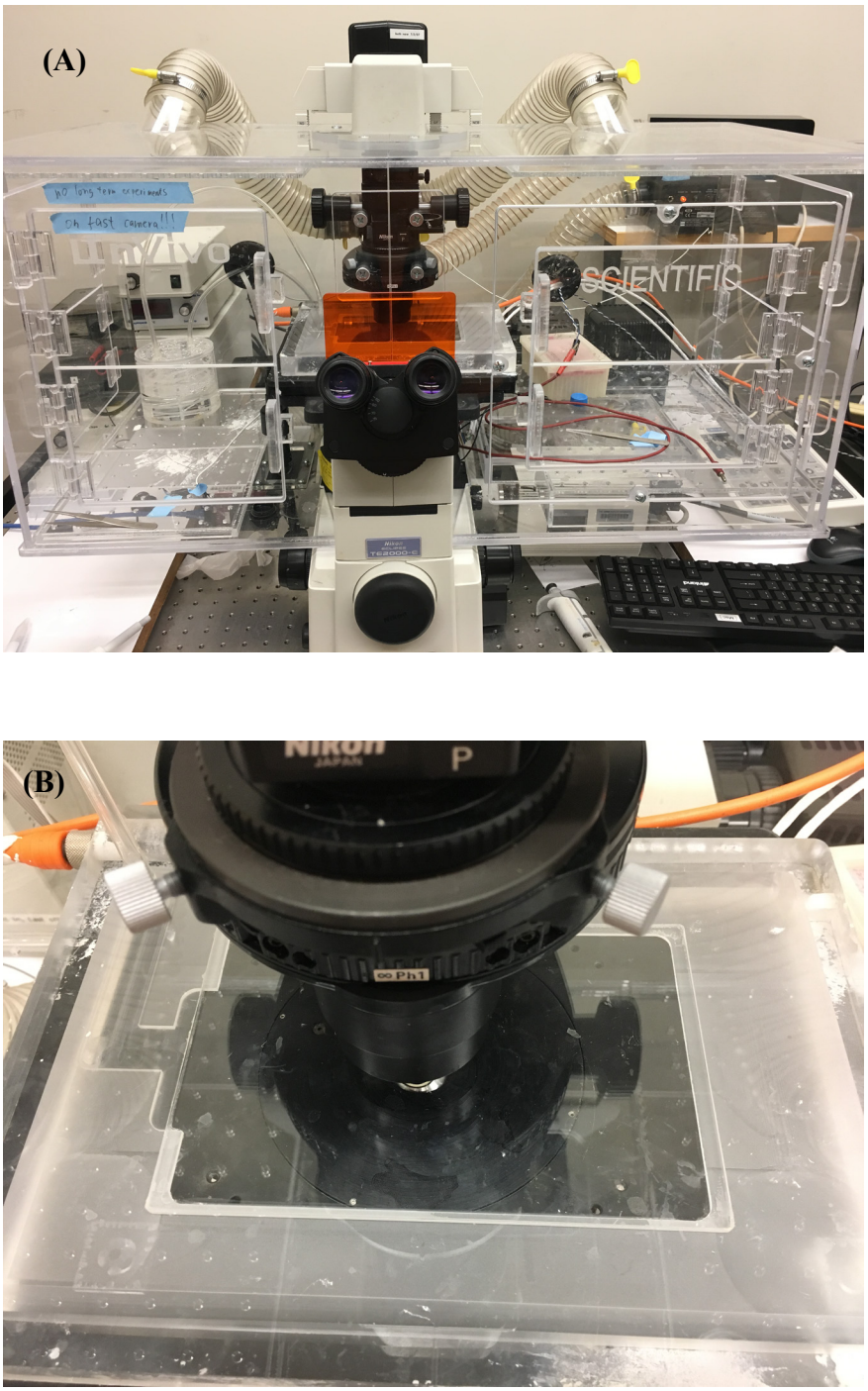

Figure 2.1 Photo of (A) on-stage incubator and (B) on-stage environmental control chamber

2.3.2 Micropost tracking

The microposts' positions vs. time were determined using an implementation of a centroid-based particle tracking algorithm [81] written in Igor Pro (Wavemetrics). Each frame was processed with a Mexican-hat filter, which is composed of a 2D Gaussian filter with size of 3 pixels, and an averaging filter with the size of microposts' diameter. The results from the averaging filter are subtracted from the results from the Gaussian filter, to obtain convoluted images with enhanced contrast and subtracted background (**Figure 2.2**). A square mask centered at the initial guess position of microposts center with size slightly larger than the diameter of the microposts is created, and the center position is recalculated based on the intensity-weighted center of all pixels within the mask (centroid fitting). The mask is shifted towards the new fitted center, and this process is repeated recursively until the difference between the guessed (generated from the undeflected positions of the microposts based on the hexagonal lattice) and fitted center is less than 0.5 pixel. To account for frame-to-frame drift, the average displacement in each frame relative to the initial frame of all microposts not in contact with cells (background posts) was subtracted from all individual micropost trajectories. The undeflected positions of posts in contact with cells were determined by interpolation based on the positions of the background posts in the corresponding rows and columns of the AMPAD array [82].

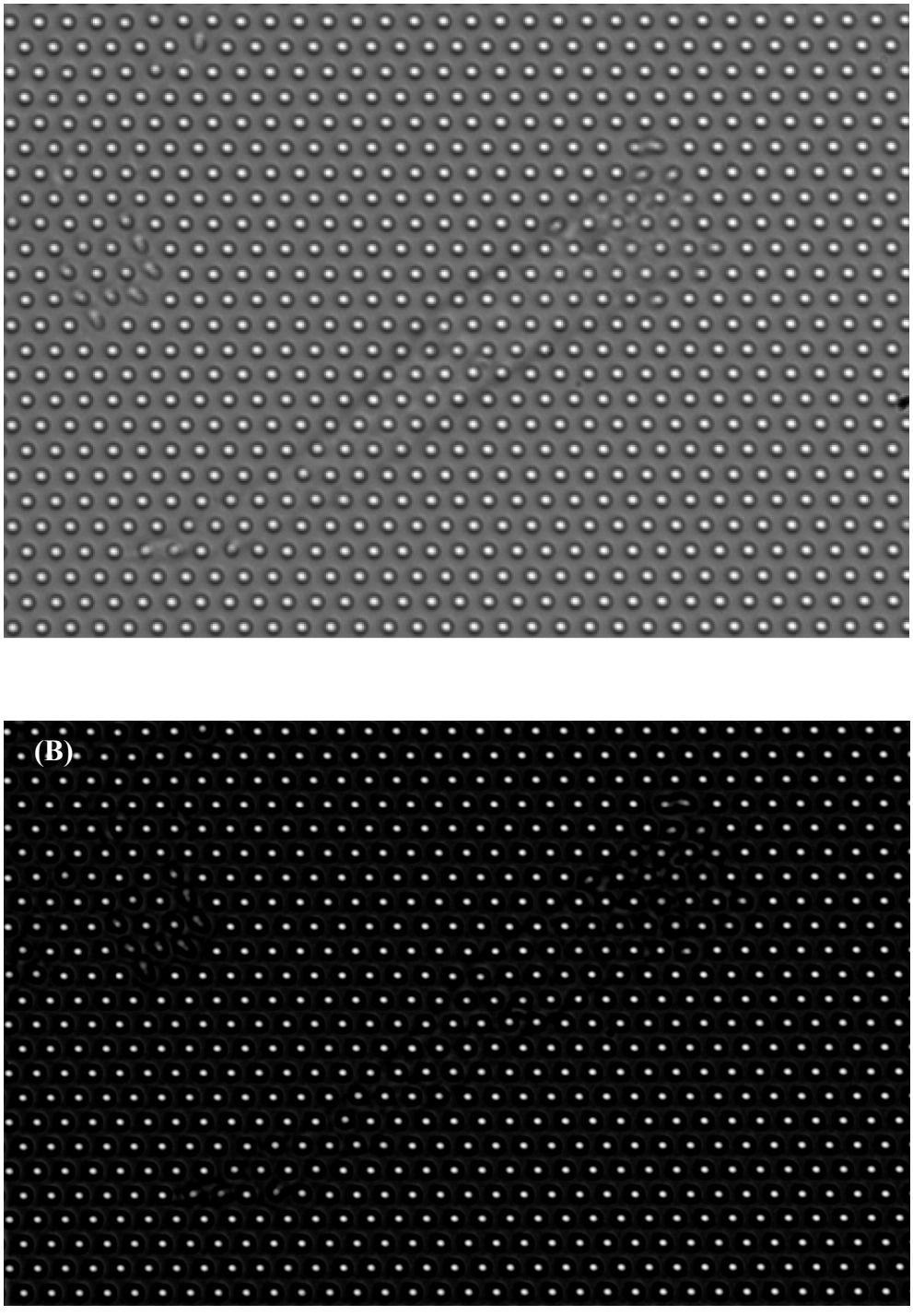

Figure 2.2 (A) Bright field image of a 3T3 fibroblast on micropost arrays. (B) Preprocessed image after applying Mexican-hat filter.

2.4 Imaging for active microrheology

In this section I describe the experimental process for conducting cellular local active rheology measurements using a dual magnetic tweezer system. The process for extracting magnitude and phase information out of a sinusoidal signal will also be discussed.

2.4.1 Magnetic tweezers and local cellular rheology measurements.

In order to actuate microposts with embedded magnetic nanowires, a magnetic tweezer was used to apply an AC magnetic field. Two solenoids filled with iron cores were each mounted on 3-axis micromanipulator stages. The iron cores had finely sharpened pole tips and were maintained every 3 months by removing rust with a sanding machine and coating the tips with PDMS. The pole tips were positioned 0.5 mm apart and 0.8 mm above the microposts arrays, which provided an approximately spatially uniform magnetic field that could be localized on an individual cell. We used a custom-built sample dish with an indented lid to enable the tweezer tips to be brought within 1 mm of the cells without touching the culture media (**Figure 2.3**, **Figure 2.4**). The culture media filled the space between the sample and a glass window in the lid to eliminate any image distortion associated with an air-liquid interface in the optical path. The solenoids were connected in series and were driven by digitally synthesized waveforms from a National Instruments PCIe-6231 DAQ card controlled by the StreamPix software and amplified by a Kepco BOP 50-2M power supply. Sinusoidal magnetic fields of amplitude 10 mT were used to produce magnetic torques with amplitudes 1.5 nN·µm on the nanowires that led to effective forces F_{mag} with amplitude 250 pN applied to the portion of the cell adherent to the magnetic

microposts [82, 83]. Videos were recorded at f_S = 100 frames/s and Hall sensors attached at the back of the magnetic tweezer's iron cores monitored the magnetic field, which was recorded synchronously with each video frame via the DAQ card. The frequency f of the magnetic field was varied in the range 0.1 Hz ≤ f ≤ 135 Hz. A second sinusoidal field at a fixed reference frequency f_R = 7 Hz was applied simultaneously with that at f to enable a ratiometric measurement of the response to account for temporal variations in the cell-post coupling (Discussed in the next section.) [84]. Measurement times were 180 s for f ≤ 0.1 Hz, 60 s for 0.1 Hz < f ≤ 10 Hz, and 30 s for f > 10 Hz with 30 s before and after switching frequencies to ensure stability in measurements. The measurement process was automated using a script in Streampix. The cells were subsequently removed from the AMPAD arrays with trypsin/EDTA, and the measurements were repeated to obtain the background frequency-dependent viscoelasticity of the individual magnetic microposts alone, to account for any post-to-post variations. (A detailed protocol can be found in the Appendix.)

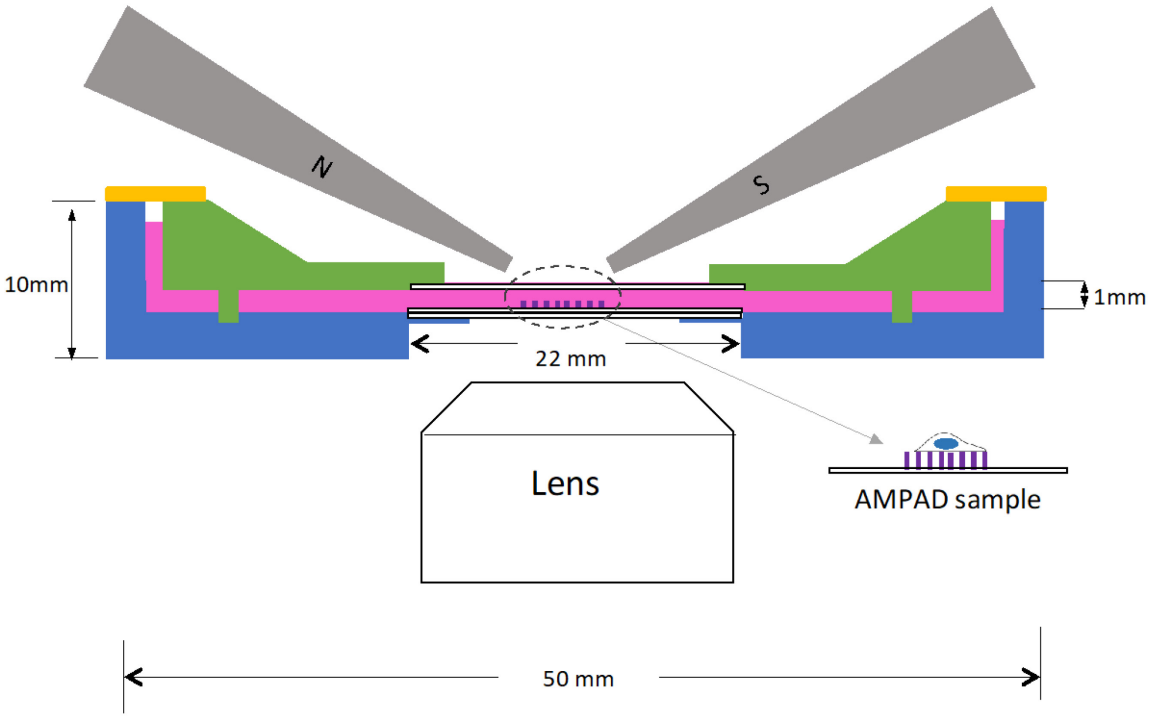

Figure 2.3 Rheology measurement schematic. A custom 50 mm diameter culture dish was fabricated out of acetal plastic (blue). A standard square coverslip (22 mm width × 0.17 mm thick) (shown in outline) was glued with PDMS into a cutout in the dish to allow optical access. An AMPAD substrate with adhered cells and mounted on a similar coverslip was fit into the cutout on top of the first coverslip. An acetal lid (green) allowed the magnetic tweezer tips (gray) to be brought within 1 mm of the cells without contacting the culture media (pink). The lid had a coverslip glued into it to allow illumination, and the culture media completely filled the volume between the dish and the lid. The lid had four integrated, 2 mm diameter posts in a square pattern that fit into corresponding indentions in the dish to prevent motion of the lid. A PDMS ring (orange) was used to cover the open area between the edge of the lid and the dish to reduce media evaporation.

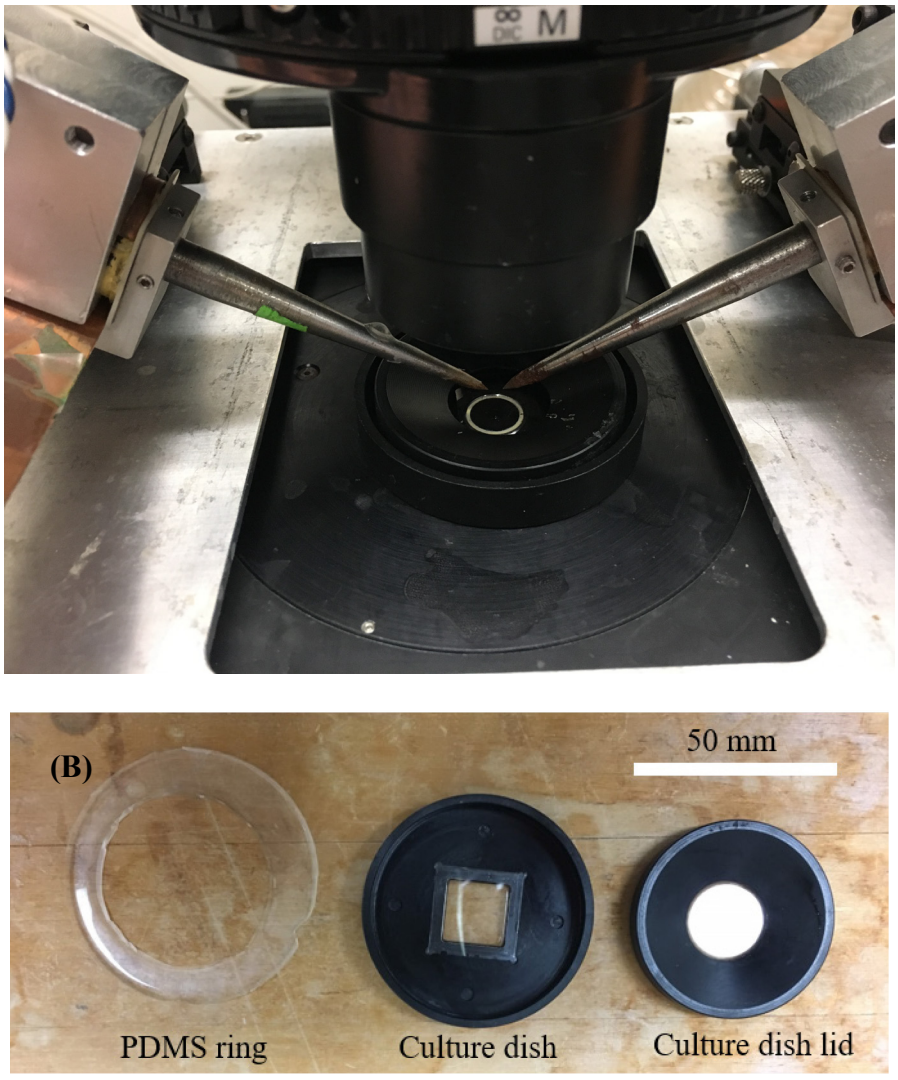

Figure 2.4 Photo of (A) dual magnetic tweezer system and (B) components of customized dish for AC actuation measurements.

2.4.2 Analysis of magnetically actuated cellular rheology measurements

The amplitudes and phases of the magnetic microposts' response at the frequencies f and f_R were found via digital lock-in analysis [85] of the microposts' positions $\mathbf{r}(t)$ determined from the image sequences as described in Section 2.3.2 Particle tracking.

Due to the finite exposure time, the AC amplitude extracted from the digital lock-in analysis was reduced in a frequency-dependent way due to its averaging effect, as shown in the formula below.

Suppose we have a sinusoidal signal written as $f(t) = A\cos(\omega t)$. In our case, A is the deflection magnitude of the magnetic micropost and ω is the angular frequency of the magnetic field. Considering that the finite exposure time will give the amplitude of *f(t)* averaged over the exposure window, then the recorded signal intensity S over a finite exposure time T_e is:

$$\mathrm{S} = \frac{1}{T_e}\int_{n\Delta t}^{n\Delta t+T_e} A\cos(\omega t)dt = \frac{A}{T_e\omega}\{\sin[\omega(n\Delta t+T_e)]-\sin[\omega(n\Delta t)]\}$$

$$=\frac{2A}{\omega T_e}\sin\frac{\omega T_e}{2}\cos[\omega(n\Delta t+\frac{T_e}{2})]=\frac{\sin\alpha}{\alpha}A\cos[\omega(n\Delta t+\frac{T_e}{2})]\ ,$$

where $\alpha = \omega T_e / 2$. Therefore, the amplitude is reduced by a prefactor $\frac{\sin\alpha}{\alpha}$ and the phase is shifted by α.

Another phase shift arose from the fixed lag time t_{lag} between the camera exposure window and the sampling of the magnetic field by the DAQ card. This was measured to be t_{lag} = 0.02 s by imaging an LED driven by the DAQ card.

Data at frequencies above the Nyquist frequency $f_{Ny} = f_S/2$ = 50 Hz (f_S is the sampling frequency) were measured via aliasing, *i.e.* at apparent frequencies f_k. Notably, this procedure will introduce an additional phase shift, as demonstrated below:

Suppose a sinusoidal signal can be written as $S = A\cos(2\pi ft + \varphi)$, where f is the measured frequency and φ is the phase shift. Since $f_s t = n$ is the number of frames captured by the camera, it is an integer. Then when 50 Hz < f < 100 Hz

$$\begin{aligned} f_k &= f_s - f \\ S &= A\cos(2\pi ft + \varphi) \\ &= A\cos(2\pi(f_s - f_k)t + \varphi) = A\cos(2\pi f_s t - 2\pi f_k t + \varphi) \\ &= A\cos(2\pi f_k t - \varphi + 2\pi n) = A\cos(2\pi f_k t - \varphi) \end{aligned} .$$

This indicates that the phase is inverted from φ to $-\varphi$ when measured at the apparent frequency f_k over the range of 50 Hz < f < 100 Hz. Similarly, when f > 100 Hz

$$\begin{aligned} f_k &= f - f_s \\ S &= A\cos(2\pi ft + \varphi) \\ &= A\cos(2\pi(f_k - f_s)t + \varphi) = A\cos(2\pi f_k t - 2\pi f_s t + \varphi) \\ &= A\cos(2\pi f_k t + \varphi - 2\pi n) = A\cos(2\pi f_k t + \varphi) \end{aligned} ,$$

Therefore, no additional phase is introduced when measured at apparent frequency if f > 100 Hz.

To estimate the resolution of the digital lock-in analysis, we applied it to all microposts (magnetic and non-magnetic) under an AC magnetic field. As shown in **Figure 2.5**, the measured amplitude of microposts scattered within a circle of 0.5 nm, thus indicates the AC amplitude resolution $\delta r < 0.5$ nm.

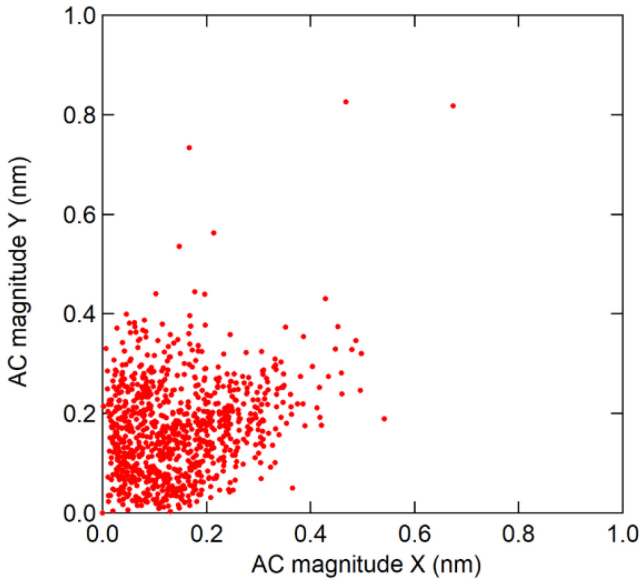

Figure 2.5 AC magnitude captured by digital lock-in for all microposts (magnetic and non-magnetic) under AC magnetic field. As shown in the figure, the noise floor is approximately 0.4 nm)

Since the local cellular stiffness and the mechanical coupling between the post and the cytoskeleton can vary with time, the measured AC fluctuational magnitude $x(\omega)$ can fluctuate with time, as shown in **Figure 2.6** A . To account these observed temporal fluctuations in $x(\omega)$, the ratio

$$x(\omega) = \frac{x_s(\omega)}{x_R(\omega_R)} \cdot \overline{x}_R(\omega_R)$$

was computed [84], where $x_s(\omega)$ was the response at the variable frequency f and $x_R(\omega_R)$ was the response at the reference frequency f_R over the same measurement interval. The ratio of those two signals was multiplied by $\overline{x}_R(\omega_R)$, the average of $x_R(\omega_R)$ over all the measurement intervals, to keep the average of $x(\omega)$ unchanged. This ratiometric approach

yielded greatly reduced fluctuations in $x(\omega)$ compared with those in $x_s(\omega)$ (**Figure 2.6** B), without affecting the relative variation in $x(\omega)$ across different frequencies.

The magnetic force $F(\omega)$ was determined from the measured magnetic field $B(\omega)$, using the nanowires' magnetic moment and the nanowires' and microposts' dimensions [82]. The equivalent stiffness was then calculated as $k(\omega) = F(\omega)/x(\omega)$. The posts' stiffness $k_{post}(\omega)$ was determined from the data obtained following removal of the cells by trypsinization, and the resulting cell stiffness computed as $k_{cell}(\omega) = k(\omega) - k_{post}(\omega)$ **Figure 2.6** C-D illustrates this process for one magnetic micropost associated with cell, and **Figure 2.6** E demonstrates that background magnetic posts showed very little differences in measured stiffness before and after cell removal. Below $f = 50$ Hz, $k_{cell}(\omega)$ was dominated by the storage modulus, and so we made power law fits to $|k_{cell}(\omega)|$ up to 20 Hz. The resulting exponents were not sensitive to varying this cutoff in the range 5 – 20 Hz. There was a ~30% systematic uncertainty in the measurement of the magnitude of the stiffness due to variations in the magnetic torque applied by the nanowires. This is dominated by the ~25% uncertainty in the nanowires' magnetic moment due to polydispersity in their volume (see above), and there is an additional variation of up to ~6% in the magnetic torque due to possible misalignment of each nanowire from vertical (up to 20°). We also found that the component of micropost motion perpendicular to the magnetic field $y(\omega)$ was typically less than 10% of the motion $x(\omega)$ parallel to the field. However, we note that the measurements of the power-law dependence of $k_{cell}(\omega)$ were insensitive to this effect.

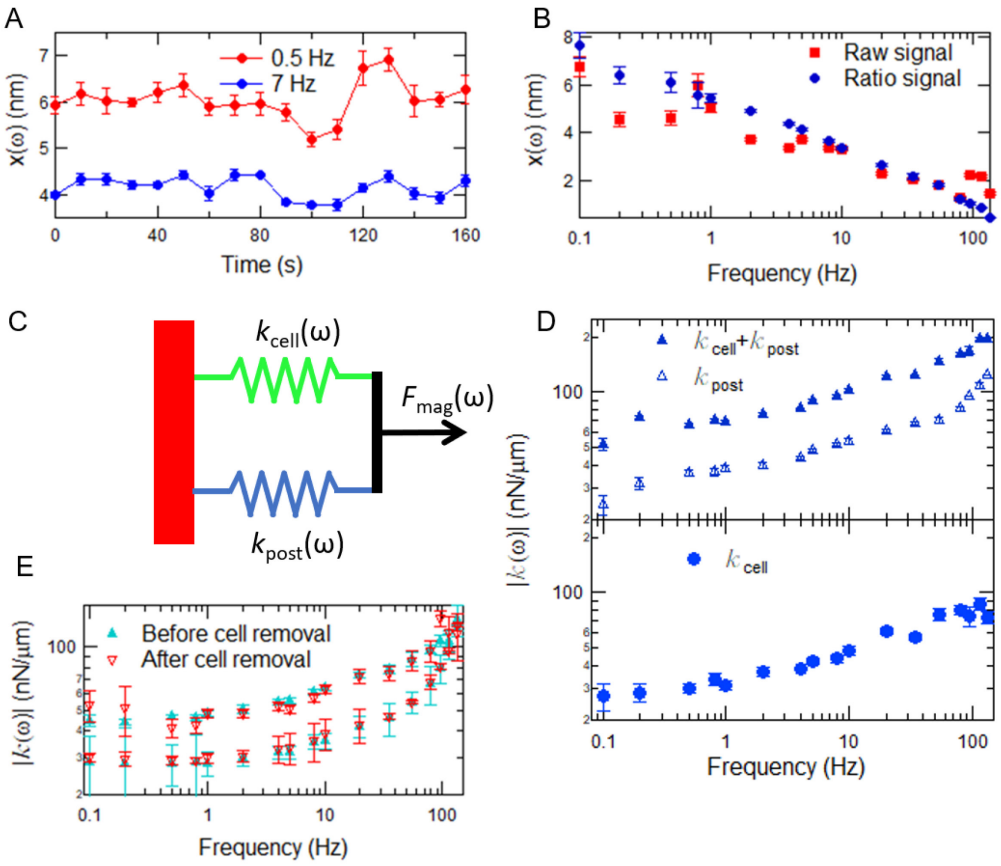

Figure 2.6 Determination of cellular rheology from AMPAD measurements. (A), (B) The ratio between responses at two different driving frequencies improves measurements of cytoskeletal rheology. Magnetic microposts' AC response $x(\omega)$ (A) to simultaneously applied sinusoidal signals at 0.5 Hz (red) and 7 Hz (blue) showed correlated variation over time. These temporal variations led to significant noise in measurements of the frequency dependence of $x(\omega)$ (B, red symbols). An approach that measured the ratio $x(f)/x(f_R)$ (B, blue symbols) with f_R = 7 Hz greatly improved the measurements of the cytoskeletal rheology. (C) A cell-coupled magnetic micropost behaves as two viscoelastic units coupled in parallel in response to F_{mag}. (D) Upper panel: Frequency dependence of the equivalent stiffness $|k(\omega)|= |F(\omega)/x(\omega)|$ of a post coupled to a cell (solid triangles) and of the same post after removal of the cell trypsin/ETDA (open triangles) measured via magnetic active microrheology. Lower panel: The cellular stiffness $|k_{cell}(\omega)|$ is given by the difference between the above two data sets. (E) The frequency dependence of the stiffness of two magnetic microposts that were not coupled to cells, before (solid triangles) and after (open triangles) treatment of the AMPAD array with trypsin/ETDA to remove cells from other parts of the array. These measurements showed that the properties of the microposts were not affected by the cell removal process.

2.5 Lévy dynamics analysis

To analyze the fluctuations observed in the actin cortex, we calculated probability distribution histograms $P(|\Delta x|)$ at fixed lag times τ for the x-components of 1,800 s duration displacement traces. Histograms were generated with a constant number of points per bin for each τ (200 bins for $\tau < 10$ s, 100 bins for 10 s $< \tau <$ 100 s and 40 bins for $\tau \geq$ 100 s) and converted into probability density by dividing by the resulting 6bin widths. Each probability distribution was then fit to a Lévy stable distribution to extract the tail exponent μ. To optimize the fits, we minimized the relative differences between the experimental data and the computed distribution

$$\chi^2 = \sum \left(\frac{y_{Experimental} - y_{Model}}{y_{Experimental}}\right)^2 \quad ,$$

using the pattern search algorithm in MATLAB (Mathworks). The model was generated using MATLAB's `makedist` command to generate a symmetric stable distribution with zero mean and tail exponent `alpha` = μ-1, where `alpha` is the notation for the tail exponent used in MATLAB. Note that with our notation $\mu = 3$ corresponds to a Gaussian distribution.

Error bars on the tail exponents were estimated as the range of μ where χ^2 increased from its minimum value by the factor $(1 + 1/N_{\text{free}})$, where N_{free} is the number of free parameters [86].

2.6 Cell Culture and Staining

2.6.1 3T3 cell culture

NIH 3T3 fibroblasts (ATCC) were cultured in high glucose Dulbecco's modified Eagle medium (DMEM) (Corning Cellgro) containing 10% bovine serum (ThermoFisher Scientific), 100 units/mL penicillin, and 100 mg/mL streptomycin (Life Technologies) at 37 ℃ in 5% CO_2. For measurements, the cells were suspended via trypsin/EDTA and then seeded onto AMPAD devices in 35 mm culture dishes at a concentration of 10^4 cells/mL. The cells were incubated overnight in the above culture conditions to enable them to adhere and spread on the microposts. During measurements imaged by microscopy, the cells were maintained at 37 ℃ with a microscope enclosure incubator (InVivo Scientific), together with a stage-mounted heating plate (TC-500, 20/20 Technology). Passive measurements of cell dynamics were carried out at 5% CO_2 in the incubator's environmental sub-chamber. Magnetic actuation measurements were done in CO_2-independent medium (Life Technologies) supplemented with 4% L-glutamine, 10% bovine serum (ThermoFisher Scientific) and 100 units/mL penicillin, and 100 mg/mL streptomycin (Life Technologies), as the environmental sub-chamber could not accommodate the magnetic tweezers.

2.6.2 Neonatal rat cardiac fibroblast culture

Primary isolated cardiac fibroblasts were extracted from neonatal rats by our collaborators in Dr. Tung's Lab in the JHU Biomedical Engineering Department. Cells between p2 and p4 (second and forth passage) were cultured in Medium 199 (Gibco) and 10% fetal bovine serum (ThermoFisher Scientific) and 1% penicillin. Since fibroblasts can

transform into the myofibroblast phenotype during incubation, to define the two phenotypes clearly, cells were cultured with 0.1% TGF-β to promote the cardiac myofibroblast phenotype and 1% SD-208 (a TGF-β receptor blocker) to promote the cardiac fibroblast phenotype at 37℃ and 5% CO_2 for over 48 hours before seeding.

2.6.3 HEK and U2OS culture

Human embryonic kidney (HEK) cells (ATCC) were cultured with minimum essential medium eagle (Quality Biological) with 10% fetal bovine serum and 1% penicillin. Human bone osteosarcoma epithelial cells (U2OS, gift from Dr. Trina Schroer, JHU) were cultured with high glucose DMEM (Corning Cellgro) with 10% fetal bovine serum and 1% penicillin. Both cell types were cultured at 37℃ and 5% CO_2.

2.6.4 Immunofluorescent Imaging

For immunofluorescence microscopy, cells were fixed in Formalin solution (Sigma-Aldrich), permeablized in 0.1% Triton-X 100 and stained for F-actin with TRITC-phalloidin (Invitrogen) and for nuclei with Hoechst (Life Technologies). Images were taken with a 40x water immersion objective on a Leica SP8 confocal microscope. Two images of a single focal plane were averaged to reduce background noise.

2.6.5 Pharmacological treatments.

For myosin inhibition studies, we first measured cells' baseline mechanical fluctuations by imaging microposts for 90 s at 100 frames/s and then switched to media

with either 60 μM blebbistatin or 50 μM Y27632. After 30 minutes incubation, the cells' fluctuations were re-measured for an additional 90 s. The cells were then fixed and stained for f-actin and nuclei for morphological comparison to untreated controls via immunofluorescence microscopy. For ATP depletion studies, mechanical fluctuations were measured for 90 s as above, before and after 30 min. incubation in DMEM with 50 mM 2-D-deoxyglucose and 0.05% NaN3 (Alfa Aesar, Ward Hill, MA) [84, 87].

2.7 Statistics

The data for pharmacological treatments (**Figure 3.4** G and **Figure 3.9** 6T-V) were analyzed via unpaired T-tests.

The comparison of the MSD exponent in cortical (α_c) and stress fiber posts (α_f) shown in **Figure 3.11** and **Figure 4.11** were done using a paired T-test based on the average MSD exponent of the cortical and stress fiber posts in each individual cell.

To measure the significance of cell-to-cell variations in α_c for the cortical posts in 3T3 fibroblasts on k = 15.7 nN/μm substrate, shown in **Figure 3.11** C (whether α_c from different cells can be treated as if from the same distribution), we applied a one-way ANOVA test. The same testing was done for cell-to-cell variations in α_f for the stress fiber posts.

Since the height and duration of avalanches did not follow a normal distribution, T-test will be heavily affected by the outliers and remain inaccurate. Therefore, to compare the distribution of detected avalanche heights and durations for 3T3 fibroblasts on different substrate stiffnesses and different cell types as shown in **Figure 4.26** we used a Kolmogorov–Smirnov test (K-S test).

Chapter 3 : Probing fat-tailed fluctuations in the cytoskeleton

3.1 Introduction

In this chapter, I describe micromechanical measurements of NIH 3T3 fibroblasts using active micropost array detectors (AMPADs). These results have been published in [88]. As described in Chapters 1 and 2 above, these microfabricated supports provide a closely spaced array of deformable microposts directly coupled to the cells' actomyosin machinery [71, 78, 83, 89-91]. The posts' motion can be tracked at high speed with nanometer precision, and they also include embedded magnetic nanowires that can be used to measure the cytoskeleton's mechanical response to applied force. We found that most posts under the cell are adhered to the basal actomyosin cortex, while a subset of peripheral posts are adhered to contractile actomyosin stress fibers; the two can be readily distinguished by mean traction force. The motion of cortical posts resembles weakly polarized, two-dimensional random walks with intermittent large steps, while stress-fiber posts display motion that is both highly and persistently anisotropic. Both populations of posts report power-law viscoelasticity resembling earlier studies mentioned in Section 1.3.2 [8, 9, 31, 66, 92], and super-diffusive position fluctuations that superficially resemble those in studies of cytoplasmic tracers [31, 38, 87, 93-96] as mentioned in Section 1.3.1. Closer examination of the data, however, reveals that the mean-squared displacements of

both types of posts display broadly distributed amplitudes and super-diffusive behavior that is not naturally explained by the active gel model. We find that the amplitude distribution is fat-tailed, due to intermittent, large step-like displacements resembling avalanches and earthquakes in physical systems as mentioned in Section 1.5 [69]. Our regular array of detectors also allows us to determine the spatial extent and symmetry of the largest avalanche-like rearrangements in the cortex [97, 98], which are both spatially and temporally complex, resembling those in plastic solids [54, 99]. As described in Section 1.4.2, a recent simulation work on soft glassy materials [54] suggests a physical interpretation of our cell data wherein myosin contractile units [91] self-organize into marginally stable tensile and plastic networks, whose physics gives rise to cells' avalanches, super-diffusive motion and power-law rheology [54, 97, 100].

3.2 AMPAD Arrays Probe Cellular Motion at the Nanoscale.

A schematic of a micropost array with a cell attached is shown in **Figure 3.1** A. The arrays contain flexible polydimethylsiloxane (PDMS) microposts that deflect in response to an adherent cell's fluctuating forces and/or strains. As mentioned in Section 1.6 the microposts' tips were coated with fibronectin to enable cells to form integrin-based focal adhesion linkages to the posts [71, 78, 83], which in turn mechanically coupled the microposts directly to the cells' actomyosin network. Magnetic nickel nanowires embedded in approximately 1% of the microposts enabled actuation of those posts with an external magnetic field $B(t)$ [82, 83] to probe the cells' rheology via forces $F_{mag}(t)$ applied

by the "magnetic" posts to the cell. **Figure 3.1** B shows a confocal image of NIH 3T3 cells attached to a micropost array composed of 1.8 μm diameter posts with 4 μm spacing in a hexagonal pattern. Brightfield movies of the microposts were recorded at up to 100 frames/sec, and a centroid particle-tracking algorithm [81] was used to track the positions of the microposts with spatial resolution of < 2 nm. (See Section 2.3 for detailed description.) As shown in **Figure 3.1** C, microposts coupled to a cell showed dynamic fluctuations significantly larger than the noise observed on "background" posts that were not engaged with a cell. These fluctuations were observable over a wide range of time scales, from 100 ms to 1,800 sec (the duration of data collection for each cell) (**Figure 3.2**). While many research groups use fluorescence microscopy to facilitate image analysis of micropost motion against the background of the cell, we favor brightfield imaging for its much higher signal to noise and resulting spatial and temporal resolution. While motion of refractile objects within the cell can in principle contribute to the observed motion of nearby posts, control measurements reveal that contributions from such effects are detectable but contribute only ~3 nm of root mean square (RMS) deflection over 60 s timescales. (See Section 3.5 for detailed discussion.)

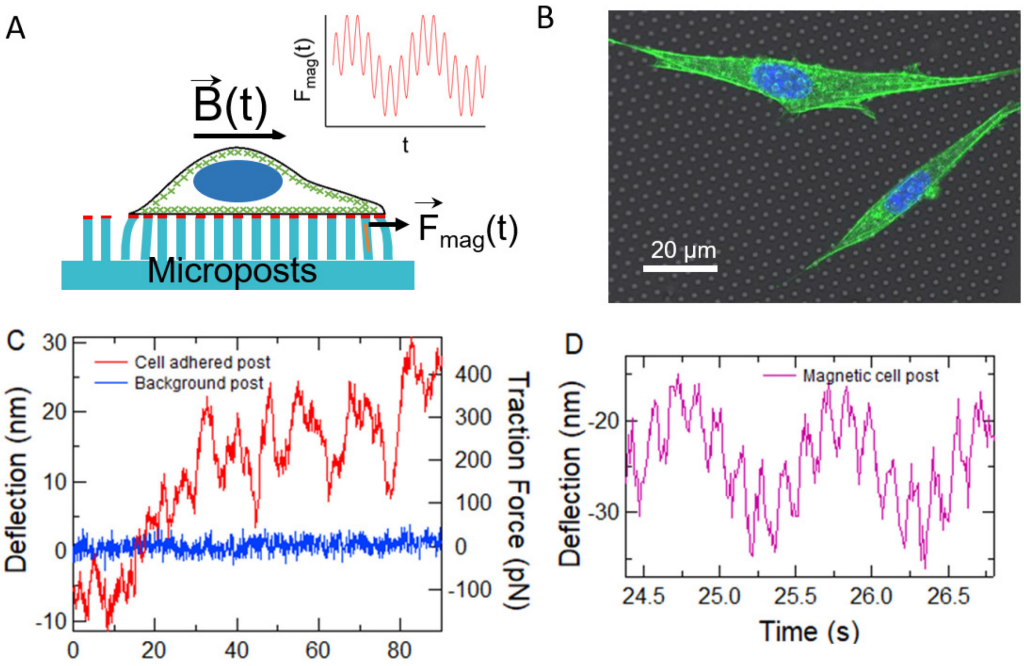

Figure 3.1 Microposts can be used to measure cytoskeletal dynamics and viscoelasticity. (A) Cell on a flexible micropost array; Micropost tips are coupled to the actomyosin cytoskeleton (green) via fibronectin (red). Posts with magnetic nanowires (orange) exert a double-sinusoidal force $F_{mag}(t)$. (B) Composite white-light image of post array with fluorescence of 3T3 fibroblasts immunostained for actin (green) and nuclei (blue). Actin stress fibers are concentrated near the cells' periphery. (C) Typical displacements of a cell-adhered (red) and a non-adhered post (blue). (D) Deflection of a cortex-adhered magnetic post, driven at 1 Hz and 7 Hz).

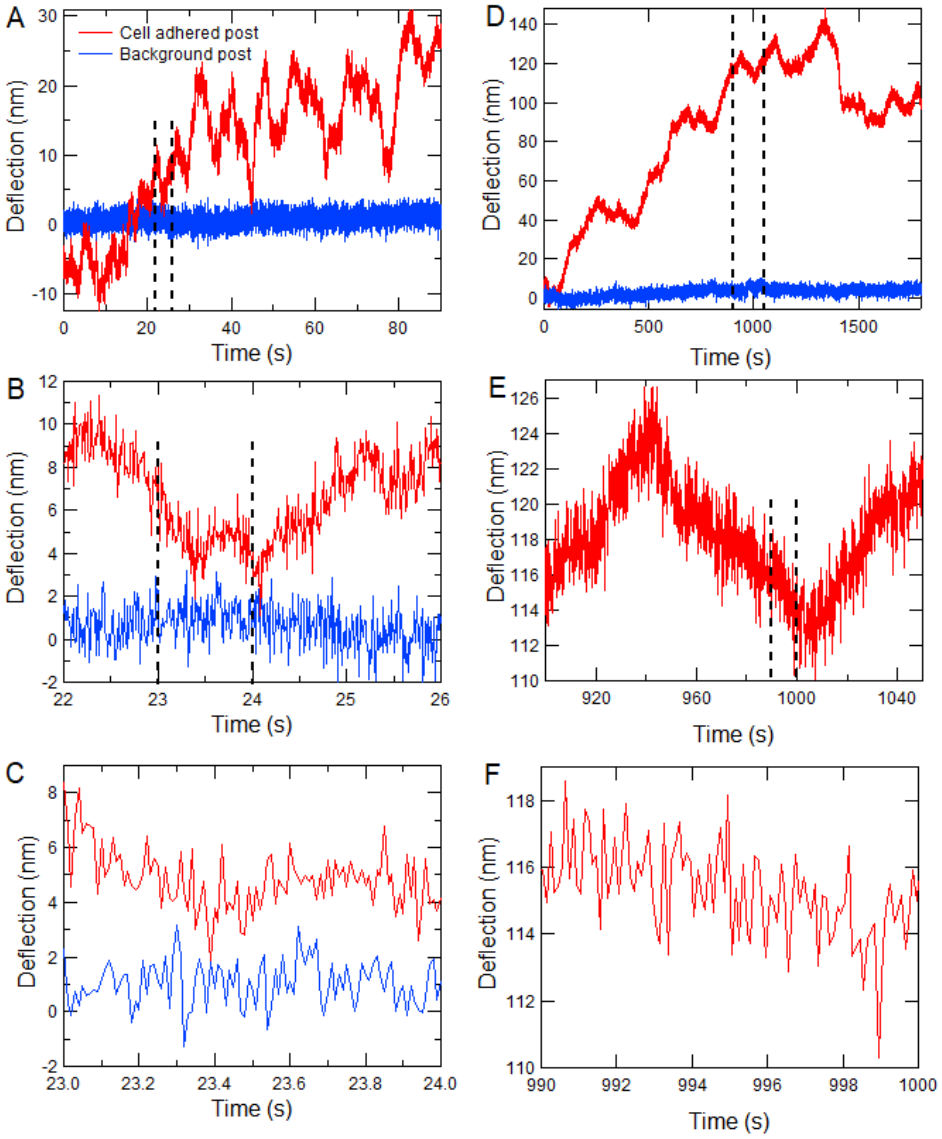

Figure 3.2 Micropost deflection traces reveal cytoskeletal fluctuations over a wide range of time scales. (A) Fluctuations of the x-component of the positions of microposts underneath and outside of a cell, measured at 100 frames/s, reproduced from Fig. 3.1C. (B) Expanded view of a portion of the traces shown in A. (C) Further expansion of a portion of the traces shown in B illustrating the high spatial resolution ($\delta x < 2$ nm) of these measurements. (D) Fluctuations of micropost positions over an 1,800 s time period, measured at 10 frames/s. (E) Expanded view of a portion of the cell-associated micropost's trace in D. (F) Further expansion of a portion of the trace shown in E, illustrating that these longer-duration measurements are sensitive to cytoskeletal fluctuations down to the 0.1 s scale.

3.3 Spatially Resolved Measurements of Cellular Power-law Rheology.

Characterizing an active matter system like the cytoskeleton requires that one probe both the fluctuations and the mechanical response to applied stress, or rheology [5]. We drove the magnetic microposts with sinusoidal magnetic fields from a dual magnetic tweezer system [45], and used digital lock-in techniques [85] to measure the amplitude and phase of the posts' resulting time-dependent motion to < 0.2 nm in amplitude. These measurements showed significant amplitude fluctuations over long timescales (**Figure 2.6** A), an effect previously attributed to time-dependence in the cell's coupling to the probe [84]. To remove such confounding effects, we applied two sinusoidal signals simultaneously, one at a frequency that was scanned over a wide range, and another which served as a constant-frequency reference (**Figure 3.1** D). Measurements of the ratio of the two signals' amplitudes [84] gave significant reduction in uncertainty for the frequency dependence of the microposts' mechanical response (**Figure 2.6** B). A detailed description of the methods used here can be found in Section 2.4.

Since both the microposts and the attached cell contribute to the response to magnetic actuation, the system effectively behaves as two viscoelastic units connected in parallel (**Figure 2.6** *C*), one of which contains the cellular contribution and other that of the post. To extract the cellular stiffness, we measured the viscoelastic response of magnetic microposts while coupled to cells, and then measured each magnetic micropost's stiffness separately after removing the cells from the AMPAD arrays via treatment with trypsin/EDTA (**Figure 2.6** *D*). The cellular stiffness was computed from the difference

between the two measurements. Control measurements showed no measurable difference in background post stiffness before and after trypsinization (**Figure 2.6** *E*).

The resulting measurements of the frequency-dependent cellular stiffness $k_{cell}(\omega)$ are shown in **Figure 3.3** A and B. We found a weak power law response, $|k_{cell}(\omega)| = A\omega^{\beta}$, extending over at least the frequency range 0.1 Hz to 20 Hz. The magnitude of the cellular stiffness, A, varied by over an order of magnitude, while the value of the power law exponent β was found to be independent of the stiffness magnitude. Notably, the exponent of the observed power laws for posts at the cell periphery and in the cell interior were indistinguishable, with $\beta_{peripheral} = 0.12 \pm 0.02$, and $\beta_{interior} = 0.13 \pm 0.02$. This near-elastic response is consistent with previous measurements of cells [8, 31, 66, 87, 94, 101]. As we discuss below, the peripheral posts were largely associated with actin stress fibers, while interior posts were coupled to the actin cortex. We also observed some additional stiffness [8, 31, 58, 94, 102-104] at the highest frequencies probed; such effects have been hypothesized by several authors to be due to actin filament fluctuations [102-104].

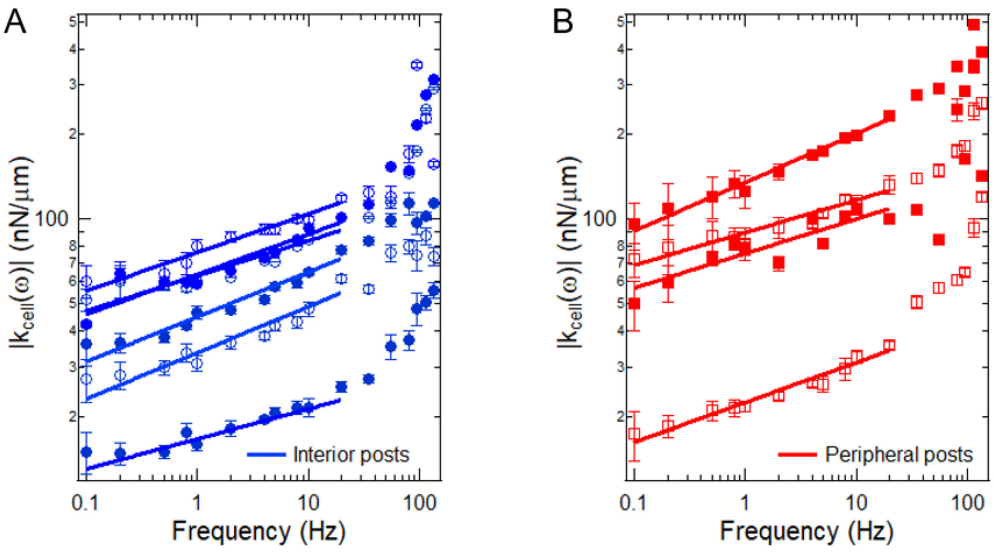

Figure 3.3 The computed local cellular rheology is a weak power law function of frequency (symbols); (A) interior posts in blue, (B) peripheral posts in red. As shown in Fig. 3.4, peripheral posts are associated with stress fibers and interior posts with the cortex. Error bars were determined as described in chapter 2.4. Solid lines are fits of the form $|k_{cell}(\omega)|=A\omega^{\beta}$ with $\beta_{interior} = 0.13 \pm 0.02$ (N = 6) and $\beta_{peripheral} = 0.12 \pm 0.02$ (N = 4) (± SE for each case).

3.4 Cellular Fluctuations are Super-diffusive and Associated with Different Cytoskeletal Structures.

We characterized the motion of the microposts in response to internally generated cellular forces via the posts' mean-squared displacements (MSDs) $|\Delta r^2(\tau)| = \langle(\mathbf{r}(t+\tau) - \mathbf{r}(t))^2\rangle$, where τ is the lag time. **Figure 3.4** A shows a representative set of MSD traces from posts whose locations underneath a cell are indicated in **Figure 3.4** B. For a range of lag times, roughly 1 s < τ < 20-100 s, the MSD curves rise above the short-time noise floor that arises from measurement error, and display power law behavior, $|\Delta r^2(\tau)| \propto \tau^{\alpha}$, with the exponent α typically being greater than 1. To extract the MSD exponent α for each post, we obtained the post's noise floor by fitting the MSD trace for $\tau \leq 1$ s to the form $MSD = C + D\tau^q$, and subtracted the constant C from the MSD traces to obtain the "subtracted MSD," MSD_{Sub}. . We only computed MSDs for τ up to 1/5 of the video length to ensure sufficient averaging for each data point. Video lengths of 1,800 s (at 10 frames/s) were used to ensure that the MSDs were recorded accurately for τ up to 360 s. We then calculated the logarithmic time derivative $\frac{d\log(MSD_{Sub})}{d\log\tau}$, and averaged its value between 5 s $\leq \tau \leq$ 10 s to obtain α and its uncertainty, as shown in **Figure 3.5**.

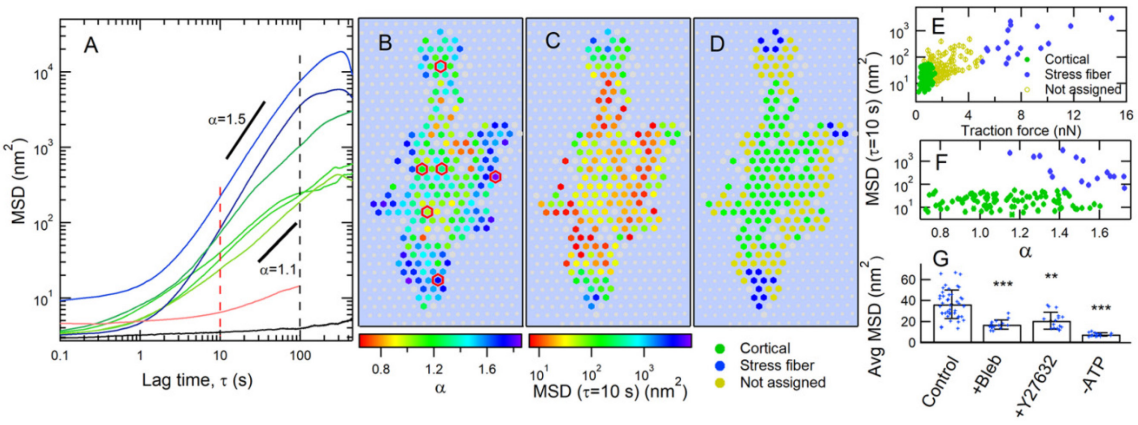

Figure 3.4 Cell fluctuations show spatial variation of amplitude and super-diffusive exponent. (A) MSD vs lag time τ for individual microposts typically show super-diffusive behavior ($\sim\tau^{\alpha}$, with $\alpha > 1$). Red and black dashed lines show τ ranges discussed below. The black trace is the MSD for a post not coupled to a cell, and the red trace shows the background due to fluctuations in cellular optical density (See 3.4). Heat maps of: (B), MSD exponent α (for 5 s $\leq \tau \leq$ 10 s), and (C), MSD amplitude at τ = 10 s for cell-adhered posts. Gray hexagons show posts not engaged with the cell for the full measurement interval. Gray circles indicate background posts. Posts with MSD traces in (A) are outlined in red in (B). (D) Classification of microposts according to traction force: maximum traction force < 2 nN ("cortical" posts with low traction force) in green; average traction force > 5 nN ("stress-fiber" posts with high traction force) in blue; remainder of posts in yellow. (E) Scatter plot of MSD magnitude at τ = 10 s vs. average traction force. (F) MSD magnitude at τ = 10 s vs. MSD exponent α for cortical and stress fiber posts (omitting middle case open circles in (E)). Standard errors for points in (E) and (F) are smaller than the symbol sizes. (G) Myosin inhibition reduces displacement fluctuations in cortical posts. Error bars in (G) show ±SD. Average MSD magnitude at τ = 10 s for control cells (25 cells), and for cells following treatment with blebbistatin (10 cells), Y27632 (11 cells), or ATP depletion (4 cells); significance via unpaired t-test. ** $p < 0.01$; *** $p < 0.001$.

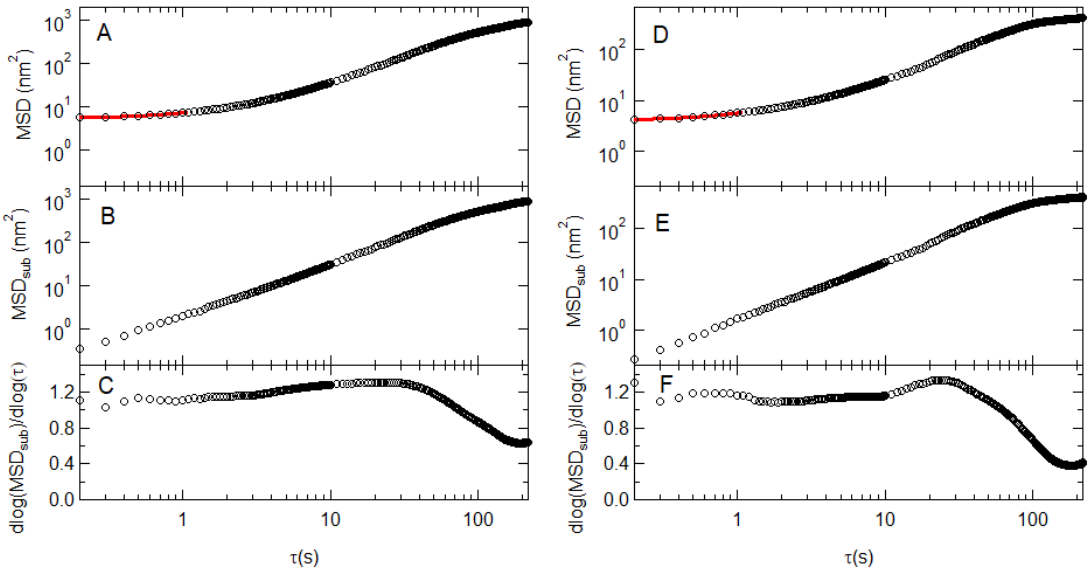

Figure 3.5 Subtracted MSD and its logarithmic time derivative, illustrating the determination of the MSD exponent α for two microposts. (A), (D) Raw MSD traces showing fits (red lines) to determine the noise floor as described in the Methods. (B), (E) MSD traces MSD_{Sub} after subtracting the noise floor from the raw MSDs. (C), (F) Logarithmic time derivatives of MSD_{Sub}. The MSD exponent α and its uncertainty were obtained from the average of the logarithmic time derivative in the range 5 s ≤ τ ≤ 10 s. The MSDs were computed at 0.1 s intervals in τ, but above τ = 10 s, they are only plotted every 1 s.

There is a large dispersion of both power-law exponents and MSD amplitudes, which does not appear to be due to statistical undersampling, as each MSD is computed from 18,000 measurements. Such super-diffusive behavior in a mostly elastic material indicates the presence of internal nonthermal driving sources [38, 87]. The values of the MSD exponent α correlate with micropost position within the cell, as shown in **Figure 3.4** B, with the largest MSD exponents typically located at the cell periphery. The corresponding map of the MSD amplitude variations is shown in **Figure 3.4** C, where again posts with larger MSD amplitude were more likely to be peripherally located. These trends

were replicated over all untreated cells studied; additional examples are shown in **Figure 3.6**.

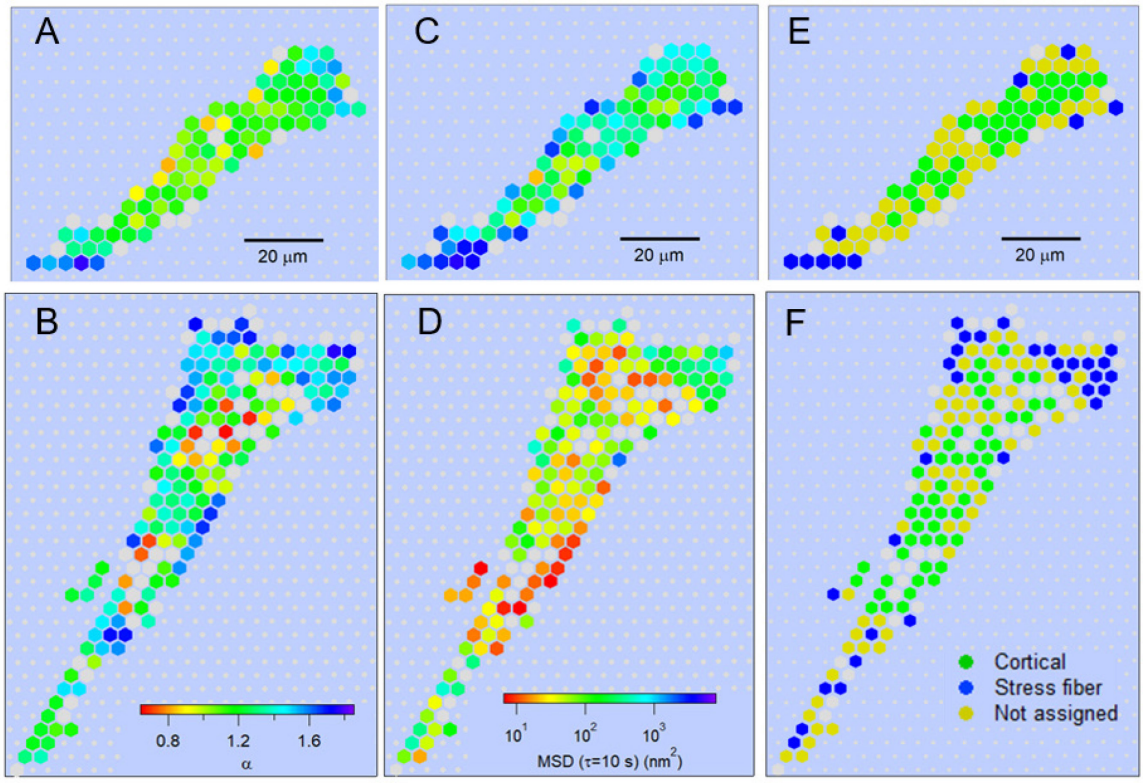

Figure 3.6 Spatial dependence of the MSD exponent and magnitude, and average AMPAD traction force for two additional cells beyond that shown in Fig. 2. (A), (B) MSD exponent α for each micropost under a cell, measured in the range 5 s $\leq \tau \leq$ 10 s. (C), (D) MSD magnitudes at τ = 10 s. As in Fig. 2, colored hexagons show the MSD exponent or magnitude for posts coupled to cells, grey hexagons indicate posts that were engaged with the cells for only part of the measurement interval, and grey circles indicate background posts. (E), (F) Classification of microposts according to traction force: maximum traction force < 2 nN (cortically associated posts with low traction force in green); average traction force > 5 nN (stress fiber-associated posts with high traction force in blue); remainder of posts in yellow.

Due to the length of the observation period (30 min), it was necessary to account for the effects of cell motility. Only microposts that were engaged mechanically with the cells for the full observation period are shown in the color maps in **Figure 3.3** and **Figure**

3.6, and were included in the subsequent analysis. To identify posts not engaged by cells, we analyzed the MSDs of background posts far from cells and found that MSD exponents $\alpha < 0.5$ provided a robust criterion. As measurement times up to 1,800 s were used, cell motility could lead to microposts being engaged with a cell over only part of the measurement window. To identify such posts, we calculated the MSD of each post separately for the first third and the last third of each video, and determined the corresponding MSD exponents α_1 and α_3 for those intervals in the range $5\ s \leq \tau \leq 10\ s$, using the approach described above. Only microposts that were engaged with a cell for both of the above intervals (i.e., had both α_1 and $\alpha_3 > 0.5$) were included in subsequent analysis. Examples of micropost traces corresponding to these various conditions are shown in **Figure 3.7** A-C. To separate the cell-coupled microposts into subpopulations associated with different components of the cytoskeleton, we used the average traction force on each post, measured over the full measurement window, and calculated based on the spring constant of the microposts, $k = 15.7\ nN/\mu m$. We identified as stress fiber posts those with average traction forces larger than 5 nN, and as cortical posts those with maximum traction force less than 2 nN. Examples of time traces for microposts that satisfied these two conditions, as well as for one rejected by this method are shown in **Figure 3.7** D-F.

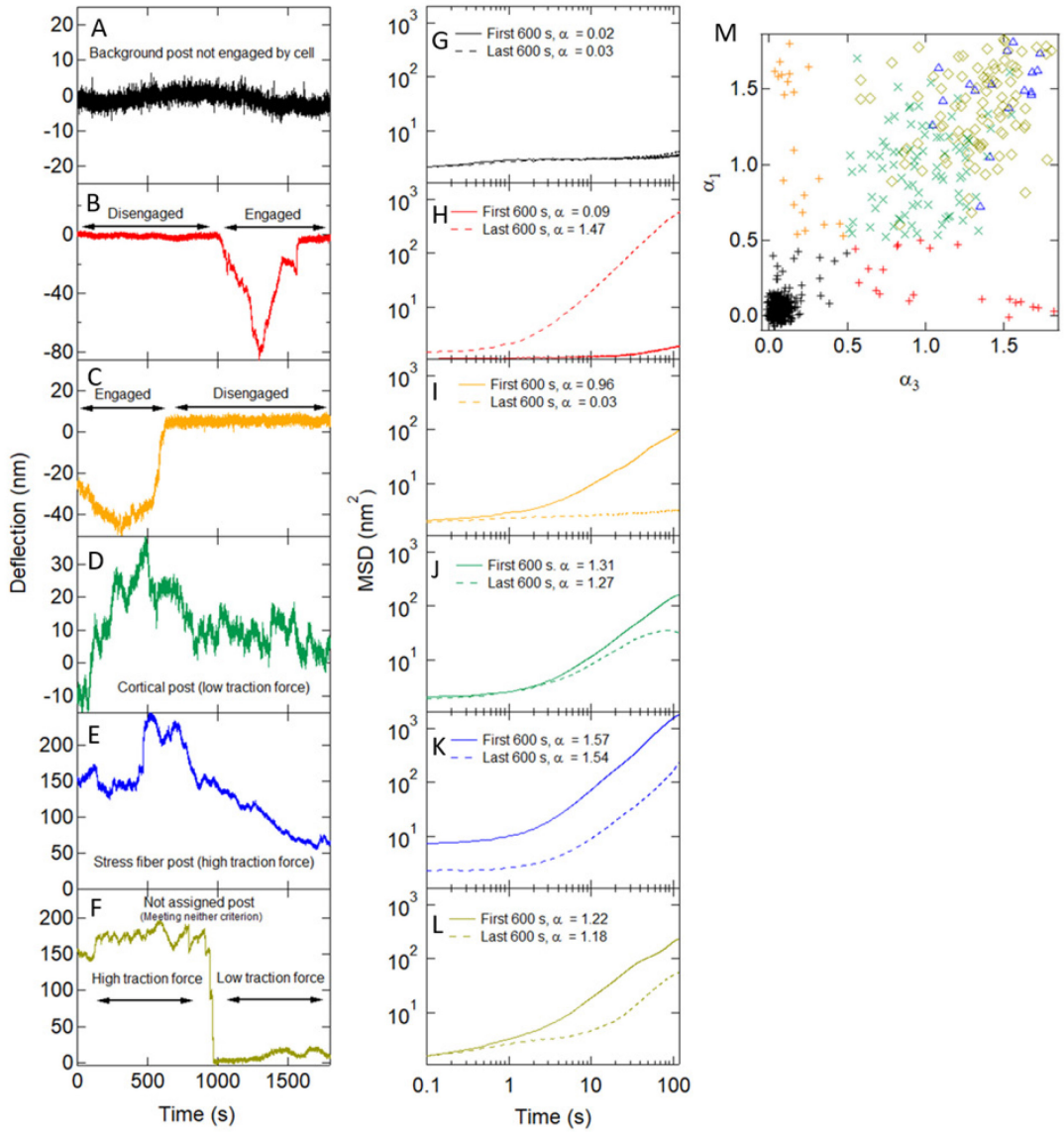

Figure 3.7. Effects of cell motility on micropost dynamics. (A-C) Illustration of the identification of microposts that were engaged with a 3T3 fibroblast over the full 1,800 s measurement interval via the requirement that the MSD exponents α_1 and α_3 computed over the first and final thirds of the interval, respectively, both be > 0.5. Only the x-component of the microposts' deflections ***r***(t) is shown. (A) A "background" micropost that was never in contact with the cell. Such posts are shown as gray circles in **Figure 3.4** and **Figure 3.6**, **Figure 3.8**, **Figure 3.9**, and **Figure 3.10**. (B) A micropost engaged with the cell only in the latter part of the measurement interval. (C) A micropost initially engaged with the cell, but subsequently released. Microposts such as those shown in B and C are shown as gray hexagons in **Figure 3.4 6,8,9 and 10**, and were excluded from subsequent analysis. (D-F) Illustration of the categorization of cell-engaged microposts based on their average traction force. (Shown as colored hexagons in **Figure 3.4**, **Figure 3.6**,**Figure 3.8**, **Figure 3.9** and **Figure 3.10**) (D) A cortical micropost with maximum

traction force < 2 nN. (E) A stress fiber micropost with average traction force > 5 nN. (F) A micropost that met neither the cortical nor the stress fiber criteria. Posts such as this were excluded from the subsequent analysis to provide clean separation between the cortical and stress fiber samples, and in particular, to exclude microposts such as the one shown here that made transitions from the high traction force (stress-fiber associated) state to the low traction force (cortically associated) state. (G-L) MSDs computed over the first and final thirds of the measurement intervals for the traces shown in Panels A-F. The MSD exponents α_1 and α_3 are given in the figure legend. Error bars on α_1 and α_3 are $\pm$ 0.01. (M) Scatter plot showing the classification of the microposts under a single cell vs. the MSD exponents α_1 and α_3. The symbol colors correspond to the behaviors illustrated in A-F, and also in **Figure 3.4** D-F, although **Figure 3.4** shows a different cell. Standard errors in *M* are smaller than the marker size.

Given the range of actomyosin structures present in a cell, in order to analyze our cellular fluctuation data, it is important to identify which cytoskeletal components individual microposts were probing. We found that average traction force magnitude provided a reliable, independent parameter with which to bifurcate our micropost dataset into two groups, those coupled to stress fibers and those coupled to the cortex, and that the fluctuation metrics (MSD amplitude and exponent) showed strong correlation with this bifurcation. This procedure is illustrated in **Figure 3.4** D-F. We segmented the microposts for each cell into a subpopulation with average traction forces larger than 5 nN, and a subpopulation with maximum traction force less than 2 nN. The high-traction force posts were concentrated at the cell edges, and the low-traction force posts were more centrally located (**Figure 3.4** D and **Figure 3.6** E, F, and **Figure 3.8**), as is typically seen for contractile cells on such substrates [71, 78, 83, 90]. The correlations of the fluctuation metrics with the traction force-based discriminator are illustrated in **Figure 3.4** E and F.

Chemical interventions confirmed the biophysically distinct character of the two micropost sub-populations, and also confirmed that the fluctuations we observed were

actomyosin-driven. Following ATP depletion or treatment with the myosin inhibitor blebbistatin (methods were described in Section 2.6.5) or the cell-permeable Rho-associated protein kinase (ROCK) inhibitor Y27632, microposts in the high-traction force category were no longer found (**Figure 3.9**), consistent with the known ablation of stress fibers under these conditions [66, 105]. The amplitudes of the low-traction force (cortical) posts' MSDs were reduced by all three treatments (**Figure 3.4** G and **Figure 3.9**), although the fluctuations were not fully ablated. The data for pharmacological treatments (**Figure 3.4** G and **Figure 3.9** T-V) were analyzed via unpaired t-tests. Confocal microscopy of the distribution of subcellular actin structures further supported the identification of the stress fiber-associated and cortically-associated micropost groups, as the cells' peripheries typically showed densely stained actin bundles (**Figure 3.1** B), consistent with the presence of actin stress fibers, while the central regions showed more diffuse actin staining, characteristic of the actin cortex. The peripheral high-density actin bundles were not visible following each of the chemical interventions (**Figure 3.9**). Overall, these observations confirm that our experiments probed active cytoskeletal dynamics, and that we can separate the posts into biophysically distinct stress-fiber associated and cortically associated cytoskeletal categories (discarding posts having an intermediate traction force).

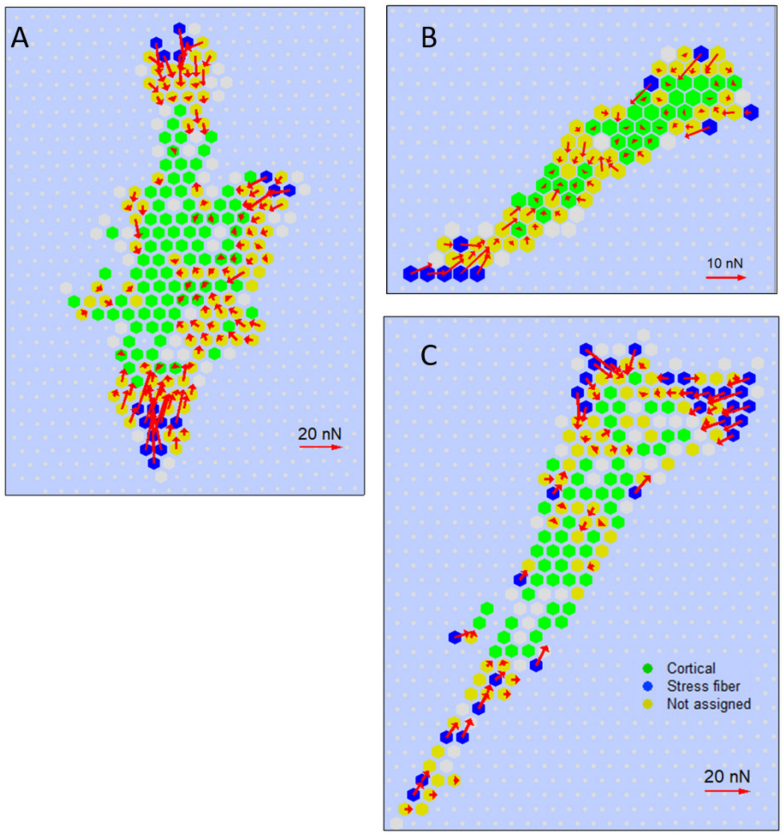

Figure 3.8 Vector maps of the average traction forces (red arrows) for (A) the cell shown in **Figure 3.4**, and (B), (C) the cells shown in **Figure 3.6**. The posts are color coded as in those figures according to our classification based on traction force: maximum traction force < 2 nN (cortical posts with low traction force in green); average traction force > 5 nN (stress fiber posts with high traction force in blue); remainder of posts in yellow.

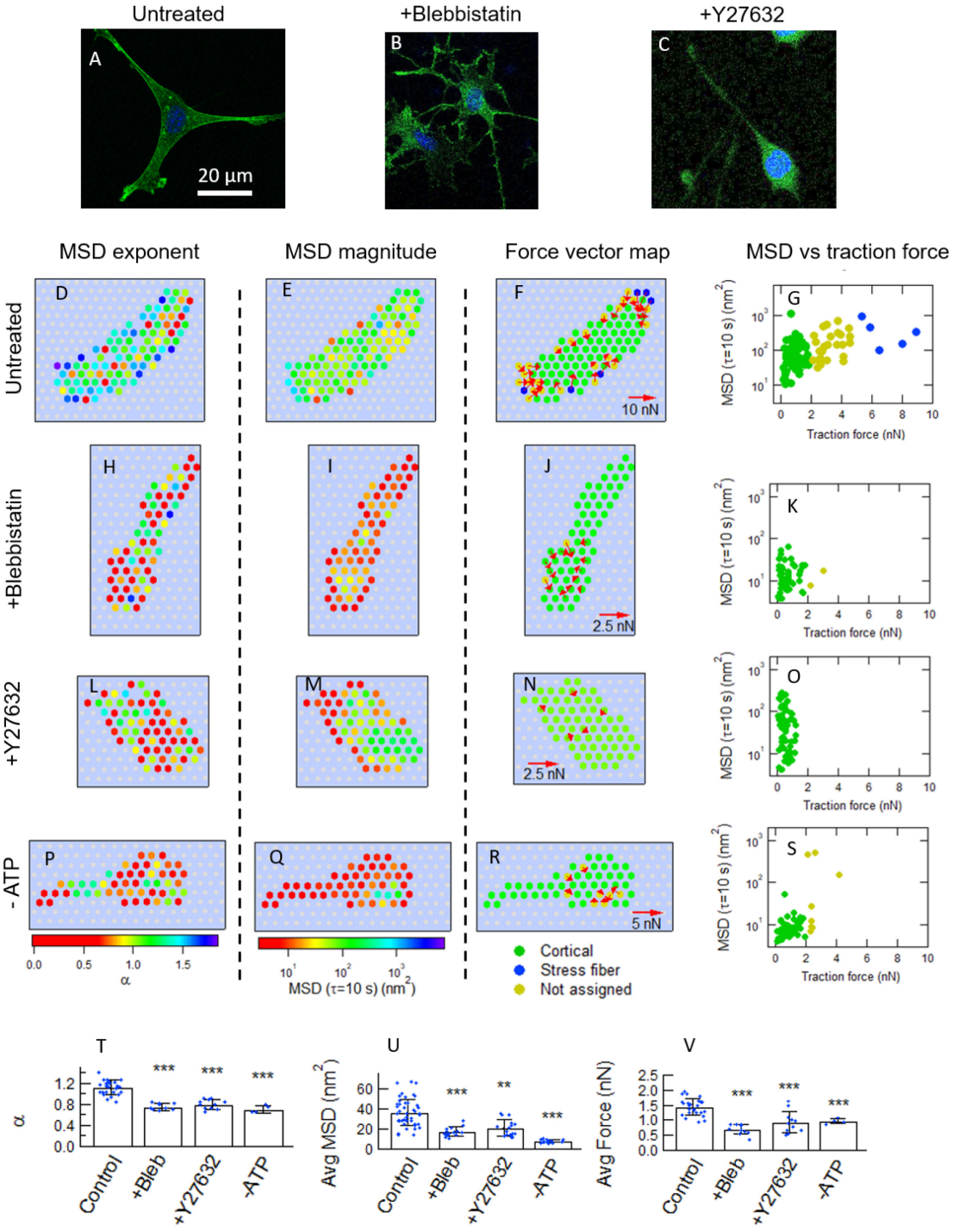

Figure 3.9 Influence of myosin inhibition on micropost MSDs. (A) Untreated, (B) Blebbistatin-treated and (C) Y27632-treated 3T3 fibroblasts showed morphology changes, with actin distributed more evenly across the cell instead of concentrated more at the cell periphery as was found in untreated cells (see also **Figure 3.1** B). Actin was stained with

phalloidin (green) and nuclei were stained with Hoechst (blue). (D) Distribution of MSD exponent α, (E) MSD magnitude at $\tau = 10$ s, (F) vector map of average traction force together with classification of microposts according to traction force as in **Figure 3.4** and **Figure 3.8**, and (G) corresponding scatter plot of MSD magnitude vs. traction force for an untreated 3T3 fibroblast cell. Corresponding plots are shown for (H-K) cells treated with blebbistatin, (L-O) Y27632, and (P-S) ATP depletion. The maps of the distributions of MSD exponent (D, H, L, P), MSD magnitude (E, I, M, Q) and MSD magnitude vs. traction force (G, K, O, S) follow the same conventions and scales as described in **Figure 3.4**and **Figure 3.6**. The standard errors in G, K, O and S are smaller than the symbol sizes. After inhibition of myosin activity, the MSD exponents, MSD magnitudes and traction forces all decreased, and stress fiber posts were not found. Quantification of effects on cortical posts: (T) MSD exponent α measured in the range $5 \text{ s} \leq \tau \leq 10 \text{ s}$, (U) MSD magnitude at $\tau = 10$ s (reproduced from **Figure 3.4** G) and (V) average traction force for untreated control cells (25 cells), and for cells following treatment with blebbistatin (10 cells), Y27632 (11 cells), or ATP depletion (4 cells); significance via unpaired t-test. ** $p < 0.01$; *** $p < 0.001$. Error bars in *T*, *U* and *V* show ±SD. All analysis was done based on videos with 90 s length.

3.5 Assessment of impact of fluctuations in cellular optical density.

As we measured the microposts' positions via white light imaging through the cells, there could be some spurious contributions to the microposts' apparent fluctuating motion and MSDs due to fluctuations in the local optical density of the cell over each micropost, arising from internal cellular rearrangements, such as organelle trafficking. To isolate and assess the impact of this effect we used posts which appeared to be transiently disconnected from the cytoskeleton, by virtue of their having very small traction force in both the x and y direction, as in those intervals any confounding contributions to fluctuations in their apparent positions due to optical density effects should be most apparent. Specifically, we searched the set of microposts that the discrimination system described above, identified as engaged with and hence under the cell for the full 1,800 s window for 300 s time

segments during which a micropost's deflections from its resting position, Δx and Δy, were both always < 15 nm (i.e., maximum traction force < 0.24 nN). The high-traction force microposts were excluded from this analysis. We found 159 such time segments over our set of 14 cells (~1% of the full micropost data set) (**Figure 3.10**). Based upon their low traction force, we identified these posts as not mechanically coupled to the cytoskeleton during that 300 s interval. This identification was confirmed by repeating the analysis but substituting a fictitious resting position for the micropost displaced a small distance from the true location and counting how many posts/intervals still satisfied the Δx, Δy < 15 nm condition. When the resting location was displaced by just 50 nm, the number dropped from 159 to ~10, which we took to be the "accidental rate" to pass the above screen.

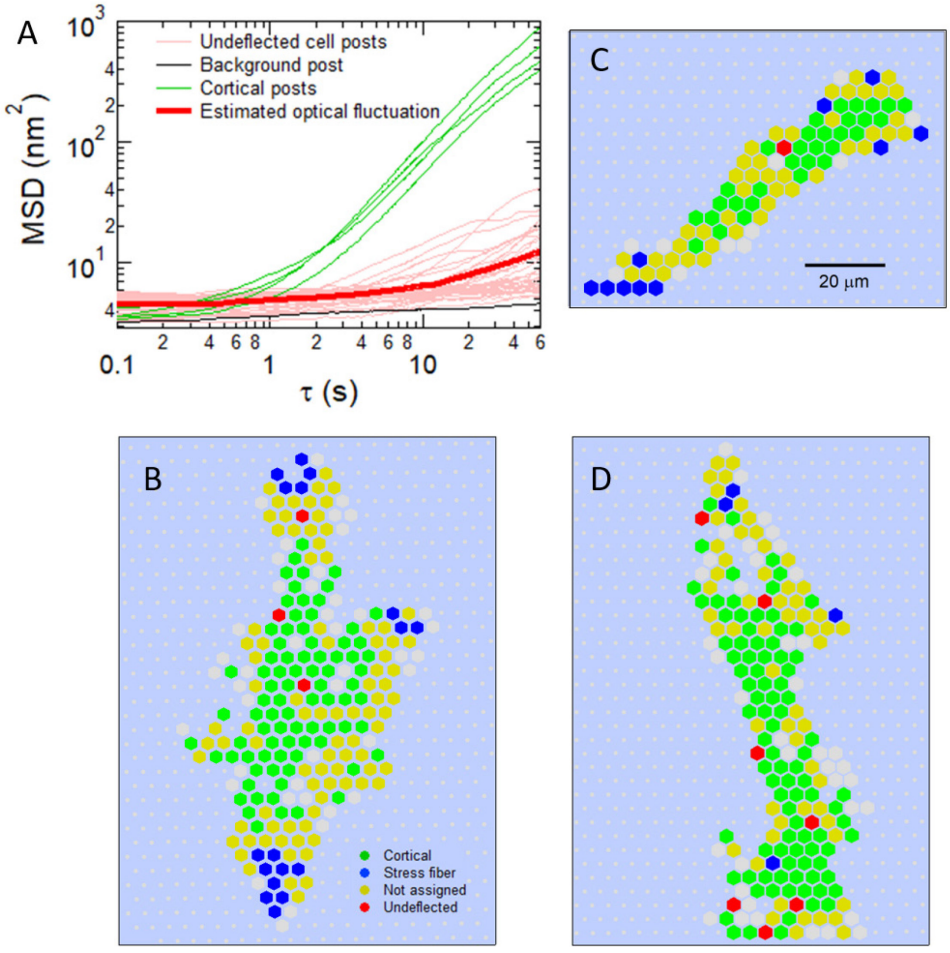

Figure 3.10 Assessment of impact of fluctuations in cellular optical density on microposts' trajectories and MSDs based on cell-coupled microposts that exhibited 300 s time segments with very small maximum deflections (Δx, $\Delta y < 15$ nm) from the posts' resting positions, and correspondingly small maximum traction forces (< 0.24 nN). (A) Pink traces: MSDs for 53 such 300 s segments. Red trace: MSD averaged over all 159 such segments in our sample. Black trace: MSD of representative background micropost not coupled to a cell. Green traces: MSDs for representative cortical microposts computed over 300 s intervals. By minimizing effects due to micropost displacement on the MSDs, this measurement sets an upper bound on the contribution of optical density fluctuations to < 10% of the MSD signal for lag times $\tau > 10$ s. (B-D) Examples of locations of microposts (red hexagons) included in this measurement, illustrating their distribution throughout the cells.

The MSDs for a representative sample comprising 53 of these time segments are shown in **Figure 3.10**. A, together with the average MSD computed for all 159 segments (also shown in **Figure 3.4**. *A* as the red curve). The fluctuations reflected in these MSDs provide a measure of the optical noise added to the position determination of the posts (centroiding) due to the cellular rearrangements over the microposts. While these time segments do show MSDs that are above the noise floor as measured by background posts far from a cell, as expected for optical noise, the average MSD for these segments is below 20 nm^2 at $\tau = 100$ s and the largest one is only ~40 nm^2. These deflections are more than a factor of 10 smaller than for typical low-traction force posts for lag times $\tau > 10$ s. Thus, such optical density fluctuation effects appear to be at most a small contribution to the microposts' MSDs.

We also considered effects that could arise if the optical centroiding noise were highly heterogeneous, in which case the noise could be greater for posts under thicker parts of the cell (containing more refractile sub-cellular components), and smaller or negligible for posts under very thin parts of the cell. In this case the actual population of decoupled, low-traction force posts/time segments could be much larger than 1% of the data, and the

"control" posts analyzed above merely a subset of such posts in optically thin cell regions. However, this effect is ruled out by the observation that the "control" posts were randomly distributed under the cells, in both thick and thin regions (**Figure 3.10** B-D). Notably, 24 of the 159 control posts/segments were found at the cells' edges, a potential region of high intracellular activity.

Another confounding possibility could be due to apparent post deflections from travelling actin polymerization waves, which have been observed in the basal cortices of many cultured cell types [106, 107]. While these are typically observed using confocal or TIRF microscopy, they can also be detected in white-light DIC microscopy [108] in very thin cell processes. Examination of the images in the latter indicate that the refractive contrast from the actin waves is much less than other cellular components such as lipid granules and organelles. Since such components were already shown in this analysis to contribute negligible optical noise to the post deflections, we can conclude that the effect from actin waves (if present in our cells) would also be negligible.

3.6 Assessment of the role of caging effects on micropost MSDs.

The micropost tips used to track cellular fluctuations in this experiment feel an elastic restoring force to return to their resting locations, unlike the free, intracellular tracers used by other researchers e.g. [87]. In principle, such a restoring force can "cage" the microposts' trajectories, resulting in the MSDs rolling over at long times. However, based

on the following arguments, such effects are not the origin of the unusual forms of the MSDs we observe.

First, at the frequencies and timescales we probed, the magnetically actuated microrheology measurements (**Figure 3.1** E and **Figure 3.3**) show that the cells are stiffer than the posts. Specifically, from the separate measurements of the posts after removal of the cells via trypsinization (**Figure 2.6** D,E) we found that cells' stiffness varied from 1-3 times that of the posts (with an average of 2X) at the lowest frequency probed, 0.1 Hz. From the weak frequency dependence observed, we estimate that the post stiffness would not begin to dominate that of the cytoskeleton until one reaches mHz frequencies i.e., timescales longer than several hundred seconds, and then only for the softest cell responses we observed.

Second, single-post MSDs intermittently show both apparent caging and non-caging behavior, (See **Figure 3.14** below), resembling free tracer results [87]. Specifically, **Figure 3.14** shows that even for MSDs averaged over 300 s intervals, some trajectories show plateaus starting as early at 10 s lag time, while other MSDs for *the same post* show no plateau out beyond 100 s. As discussed in the main text, this appears to be a consequence of the anomalous statistics and intermittent dynamics of cytoskeletal fluctuations. Notably, for free tracer data, as in Fig. 6 of Ref. [87] the MSDs also show non-reproducible plateaus. Taken together these results suggest that the differences between free tracer MSDs and our posts due to caging effects, while presumably becoming prominent at very long times, are small in the 10-100 sec range.

Finally, RMS deflections of our microposts from their resting locations suggest that our MSDs are not caged at 100 s lag time. In a simple "cage diffusion" model, the RMS

deflection of the post from its resting location, σ, is related to the plateau of the caged MSD, having amplitude 4 σ^2. While this analysis cannot be made quantitative in the face of post-to-post heterogeneity, the caging plateau implied by RMS deflections of our micropost ensemble is a factor of several times higher than the apparent plateaus seen in some of our single-post MSDs, again confirming that caging effects to our posts would not become dominant until timescales longer than we consider in this study.

3.7 Micropost Mean Squared Displacements are Highly Variable.

Typical MSDs for both cortical and stress-fiber adhered microposts are displayed in **Figure 3.11** A and **Figure 3.11** B. As seen by other authors for cytoplasmic tracers [87], the MSDs of different posts show striking variations in amplitude and time dependence. Power-law fits reveal that the MSD exponents for both cortical and stress fiber associated posts, α_c and α_{sf}, showed significant dispersion both within a given cell and from cell to cell, as illustrated in **Figure 3.11** C for four representative cells and **Table 3.1** for the entire dataset. As a measure of such dispersion, we note that the average standard deviations are $\delta\alpha_c = 0.20 \pm 0.02$ (mean ± SD, $N_{cells} = 14$) for the cortical posts, and $\delta\alpha_{sf} = 0.17 \pm 0.04$ (mean ± SD, $N_{cells} = 13$) for the stress fiber-associated posts.

We found that the cell-to-cell variations in α_c for the cortical posts are significant via a one-way ANOVA test with $p < 0.001$ over the full data set. For the stress-fiber associated posts we find variations in α_{sf} are also significant via one-way ANOVA with $p = 0.045$ for a sample consisting of all nine cells with >2 such posts. The exponent α_{sf} is

greater than α_c across the population as confirmed by a paired t-test based on the averaged exponent for each individual cell, excluding the cell (Cell 8 in Table S1) with no stress fiber posts, $p < 0.001$ ($N = 13$). On the basis of these features of the data we chose to report the exponent values for each subcellular structure's associated posts as the average of the cell-averages, rather than averaging all the individual posts directly. This approach yields $\bar{\alpha}_c = 1.17 \pm 0.02$ (SE, $N_{cells} = 14$) and $\bar{\alpha}_{sf} = 1.47 \pm 0.02$ (SE, $N_{cells} = 13$), respectively.

The observed dispersion in α_c and α_{sf} is not an experimental artifact arising simply from undersampling. To illustrate this we show in **Figure 3.11** C the dispersion of exponents around $\alpha = 1$ for a simulated Gaussian random walk that has the same number (18,000) of samples as the experimental trajectories, and which shows a very tight convergence compared to the data. While a simple random walk is not the correct physical model for the cortex, this comparison highlights the anomalous statistics and resulting poor convergence of the post displacement data.

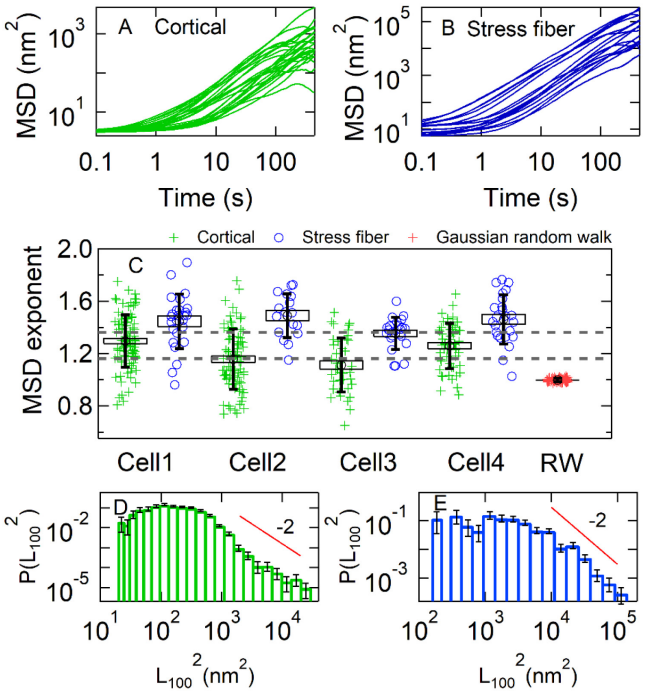

Figure 3.11. Spread of MSDs for (A) cortical and (B) stress fiber-associated microposts for a single cell (Cell 2 in Panel *C*) Traces are only shown for one third of the cortical posts for Cell 2 in Panel A for clarity. (C) Dispersion in MSD exponents α for four different cells, showing variation both within and between cells. Green crosses (blue circles) show MSD exponents for cortical (stress fiber) microposts. The dashed gray lines show the range $\alpha_c = 1.26 \pm 0.09$ (mean ± SD) expected if $\alpha = 1 + 2\beta$, given our measured values and cell-to-cell variation of β. Red crosses show data for the dispersion in α for a simulated Gaussian random walk (RW). Boxes show standard errors and vertical bars show standard deviations. See **Table 3.1** for information on full data set. (D), (E) Histograms of MSD magnitude at $\tau = 100$ s (black dashed line in Fig. 2*A*) in cortical posts (D) and stress fiber posts (E). Solid lines are power laws with exponent -3. Error bars were estimated as $1/\sqrt{N}$ for each bin in Panels D and E.

	α_c	SD for α_c	$N_{\text{cortical posts}}$	α_{sf}	SD for α_{sf}	$N_{\text{stressfiber posts}}$
Cell 1	1.29	0.20	98	1.45	0.17	26
Cell 2	1.16	0.23	84	1.49	0.12	17
Cell 3	1.11	0.21	41	1.35	0.19	23
Cell 4	1.26	0.17	54	1.46	0.21	24
Cell 5	1.19	0.21	26	1.59	0.14	8
Cell 6	1.05	0.23	20	1.51	0.16	2
Cell 7	1.19	0.19	25	1.50	0.21	12
Cell 8	1.19	0.16	49	N.A.	N.A.	0
Cell 9	1.21	0.18	64	1.54	0.04	2
Cell 10	1.19	0.19	24	1.32	0.14	3
Cell 11	1.10	0.21	97	1.50	0.14	2
Cell 12	1.25	0.22	21	1.52	0.15	12
Cell 13	1.15	0.26	58	1.53	0.25	8
Cell 14	1.16	0.21	42	1.44	0.19	32

Table 3.1 Summary of data for MSD exponents α_c and α_{sf} for cortically associated and stress-fiber associated microposts, respectively. Data for individual posts are shown for Cells 1-4 in **Figure 3.11**. Standard deviations (SD) and the number of posts of each type are listed for each cell. The average values are $\bar{\alpha}_c = 1.17 \pm 0.02$ (±SE, $N_{cells} = 14$) and $\bar{\alpha}_{sf} = 1.47 \pm 0.02$ (±SE, $N_{cells} = 13$), respectively, and the average standard deviations are $\delta\alpha_c = 0.20 \pm 0.02$ (±SD, $N_{cells} = 14$) for the cortical posts, and $\delta\alpha_{sf} = 0.17 \pm 0.04$ (±SD, $N_{cells} = 13$) for the stress fiber-associated posts.

In the active gel model [38, 60, 64, 87] such active fluctuations are the result of myosin mini-filaments binding, sliding and unbinding randomly in space, time and

orientation. Making simple assumptions for the myosin activity, the resulting MSD exponent is predicted to have a value equal to $\alpha = 1 + 2\beta$, even when the motion is the result of a small number of actomyosin binding events. Based on our measured values of β, one would therefore expect $\alpha_c = 1.26 \pm 0.09$ (mean ± SD). This range for α_c is shown as dashed lines **Figure 3.11** C and corresponds to the observed cell-to-cell variations in β. The cell-averaged value of the cortical exponents $\bar{\alpha}_c = 1.17 \pm 0.02$ (SE, $N_{cells} = 14$) is consistent with the $\alpha = 1 + 2\beta$ prediction to within experimental uncertainty. In contrast, the stress fiber exponent values for individual cells differ from the expected range $\alpha_{sf} = 1.24 \pm 0.09$ (mean ± SD), as does the value averaged across all cells, $\bar{\alpha}_{sf} = 1.47 \pm 0.02$ (SE, $N_{cells} = 13$, $p < 0.001$). Notably, the standard deviation of the cortical MSD exponents, $\delta\alpha_c = 0.2$, is significantly larger than expected given the small standard deviation of β values ($2\delta\beta = 0.09$). This appears to be incompatible with prediction of the active gel model with a simple picture of temporally and spatially uncorrelated actomyosin filaments deforming a network with power-law viscoelasticity.

In addition to the exponent, we can analyze the distribution of MSD amplitudes at $\tau = 100$ s, $L_{100}^2 = \text{MSD}(\tau = 100 \text{ s})$, as shown in **Figure 3.11** D and **Figure 3.11** E. For both the cortical and stress-fiber posts the distributions of L_{100}^2 are highly non-Gaussian with a "fat tail" at large amplitudes, with a form that is comparable to an eye-guide having a power-law form with an exponent of -2. Power-law tails can lead to poor convergence to the mean when averaging data together; formally, the mean $\langle x \rangle$ of power-law distributed numbers diverges [109] in the case of a power-law tail where $P(x) \sim x^{-a}$, for $a \leq 2$. The fat tails that we observe in **Figure 3.11** D,E are, notably, comparable to that threshold,

suggesting that the dispersion of MSD amplitudes may be a consequence of non-Gaussian statistics [109] in the microposts' fluctuations.

3.8 Microposts Display Rare Large Displacements and non-Gaussian Random Motion.

The extreme variability of different cellular tracer MSDs is often attributed to cell "heterogeneity." That is, the fat tails of large MSD amplitudes in **Figure 3.11** D and **Figure 3.11** E are typically supposed to be due to a population of microposts that sample parts of the cytoskeleton that are correspondingly softer or have higher amplitudes of myosin activity. In what follows, we analyze the fluctuations of single post trajectories, and find clear evidence in the cortex, at least, that anomalous statistics, and not heterogeneity, are responsible for the large dispersion observed in micropost MSDs.

First, we compute a dimensionless anisotropy index of the two-dimensional trajectories of each post via a principal component analysis (as a dimensionless measure, this is in principle insensitive to the heterogeneous amplitudes of different MSDs). Each post's 1,800 s trajectory was broken into 20 segments of 90 s duration and the two-dimensional moment of inertia tensor I of the trajectory [110] for each segment was computed. As illustrated in **Figure 3.12** A, the ellipse defined by the two eigenvalues λ_1 and λ_2 of I yields a anisotropy index $\lambda_1/\lambda_2 \geq 1$ for a post's motion during that interval. **Figure 3.12** B shows the probability distribution for the anisotropy index of the cortical micropost trajectories. The distribution shows that most trajectories are essentially isotropic (as compared to a simulated isotropic random walk), but that there is a highly

anisotropic subset forming a power law tail at large λ_1/λ_2, with an exponent of roughly -3. To understand the nature of the highly anisotropic trajectories in **Figure 3.12** B, we display typical post trajectories with different anisotropies in **Figure 3.12** C. These typically show random and isotropic motion, with amplitude of a few nm (corresponding to λ_2), superimposed on a large unidirectional displacement (corresponding to λ_1) that spans several tens of seconds of time.

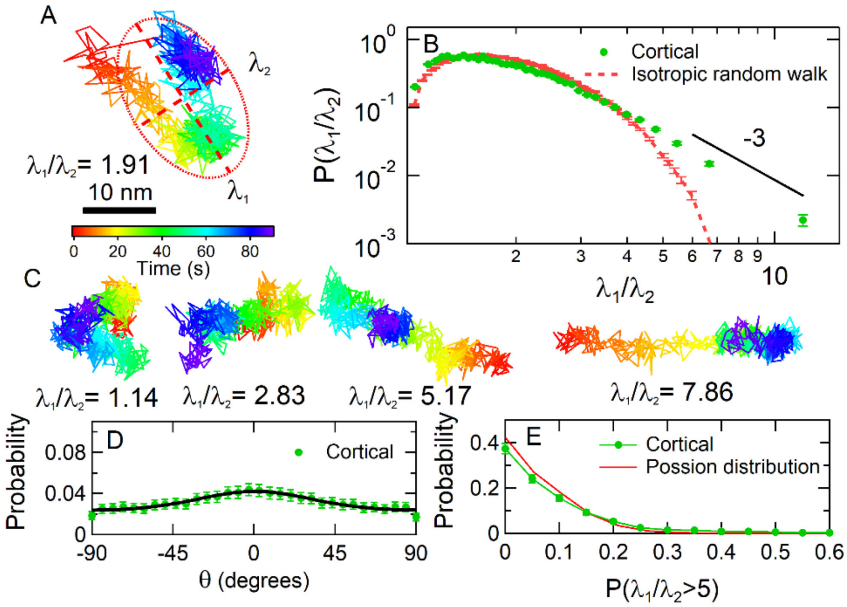

Figure 3.12 Cortical cell fluctuations showed anisotropy. (A) An example of a displacement trajectory of a micropost over a 90 s interval. The red ellipse with semimajor axis λ_1 and semiminor axis λ_2 illustrates the computation of the anisotropy index λ_1/λ_2 for this trajectory via principal component analysis ($\lambda_1/\lambda_2 = 1.91$ in this case.). (B) Probability distribution of the anisotropy index λ_1/λ_2. Eyeguide highlights a power-law tail for highly anisotropic trajectories. (C) Examples of posts with a range of λ_1/λ_2. (D) Probability distribution of the angle between the major axis of the fitted ellipse's long axis and the direction of the micropost's average traction force $\boldsymbol{F}$. The solid line is a fit with full width $2\sigma = 107°$. (E) Probability distribution of the fraction of a post's fluctuations with $\lambda_1/\lambda_2 > 5$, measured over 1,800 s in 90 s intervals. Error bars were estimated as $1/\sqrt{N}$ for each bin in the probability distributions.

To understand whether the orientation of the major axis of the trajectories (and the large displacements) are randomly presented or due to subcellular structures, we show in **Figure 3.12** D the probability distribution of the angle between the major axis of the trajectory and the post's static cellular traction force, and parametrize the widths of the probability distribution by fitting the data to a version of the von Mises circular normal distribution function with period π plus a constant offset,

$$P(\theta) = A\frac{e^{\kappa \cos 2(\theta-\theta_0)}}{\pi I_0(\kappa)} + B.$$

Here $I_0(\kappa)$ is the modified Bessel function of order 0, and the full width of the peak in $P(\theta)$ is $2\sigma = 1/\sqrt{\kappa}$. We found that the major axis of the trajectory is only weakly aligned with the mean traction direction, as shown in **Figure 3.12** D, suggesting that it is not due, for example, to the abrupt release of traction from a micropost. To assess whether these large displacements are concentrated among a subset of posts, or are clustered in time, we show in **Figure 3.12** E the probability distribution for the fraction of time when a single post's motion displays highly anisotropic motion ($\lambda_1/\lambda_2 > 5$); overall, 9.5% of the 90s-long micropost trajectories satisfied the criterion. The experimental distribution in **Figure 3.12** E closely resembles a Poisson distribution with an expectation value of 0.095, indicating that the large displacement events occur randomly over time and among different cortex-associated posts. The corresponding analysis of stress fiber-associated posts (**Figure 3.13**), in contrast, shows that their motion is both highly anisotropic, persistent in direction and aligned with the same posts' mean traction direction.

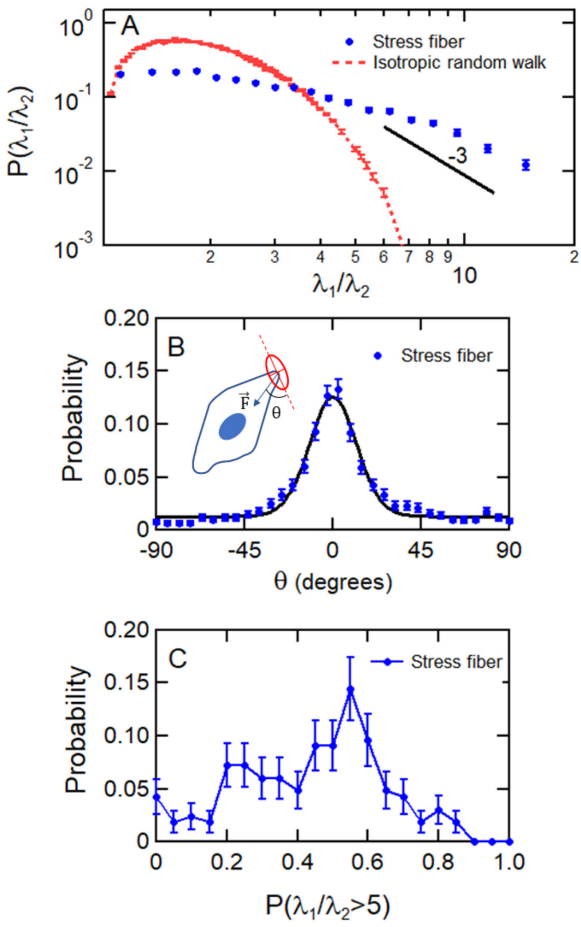

Figure 3.13. Stress fiber-associated microposts showed strong and persistent anisotropic motion in comparison to cortical posts (**Figure 3.12**) (A) Probability distribution of the anisotropy index λ_1/λ_2. Eyeguide highlights a power-law tail for highly anisotropic trajectories. (B) Probability distribution of the angle between the major axis of the fitted ellipse's long axis and the direction of the micropost's average traction force **F** (corresponding to **Figure 3.12** D). The solid line is a fit with full widths $2\sigma = 24°$. (C) Probability distribution of the fraction of a post's fluctuations with $\lambda_1/\lambda_2 > 5$. Measured over 1,800 s in 90 s intervals. (corresponding to **Figure 3.12** E). Error bars were estimated as $1/\sqrt{N}$ for each bin in the probability distributions.

We next examined the time-dependence, if any, of the amplitudes of the fluctuations of individual cortical microposts (**Figure 3.14**). Specifically, to understand the statistical fluctuations in a single trajectory, we divided each 1800 s trajectory into six trajectories of 300 s each, and computed the MSD for each (**Figure 3.14** A). Notably, the

resulting MSDs, show a significant spread in amplitude and power-law exponent, even when drawn from a single micropost trajectory, as compared with the MSD of a simulated Gaussian random walk with the same number of steps (**Figure 3.14** B). The MSD amplitudes ($L_{MSD} = [MSD(\tau)]^{1/2}$) were strongly time-dependent, an effect which is more pronounced at $\tau = 100$ s than at $\tau = 20$ s (**Figure 3.14** C), compared to the Gaussian random walk (**Figure 3.14** D). A standard way of characterizing such intermittent or "bursty" data is via a non-Gaussian parameter, $\alpha_2 = \frac{\langle x^4 \rangle}{3\langle x^2 \rangle^2} - 1$, which was calculated for each post, based on segmenting each 1,800 s trajectory into 20 s and 100 s intervals. Here, $\langle x^2 \rangle$ and $\langle x^4 \rangle$ are the 2nd and 4th moments of the set of 90 displacements for each of the 20 s intervals and the set of 18 displacements for the 100 s intervals contained in each post's 1,800 s trajectory, respectively. [111]. The distribution of non-Gaussian parameters for each cortical micropost for $N_{cells} = 14$ untreated 3T3 cells, is shown in **Figure 3.14** E, and shows a fat tail compared to that expected for a Gaussian process (which is calculated based on trajectories with the same length), presumably due to the contribution of the aforementioned large displacements. Corresponding data for the stress-fiber microposts, which show qualitatively similar behavior, are shown in **Figure 3.15**. We note that, as with the dimensionless anisotropy index, the non-Gaussian parameter would not be affected by static post-to-post variations in fluctuation amplitude.

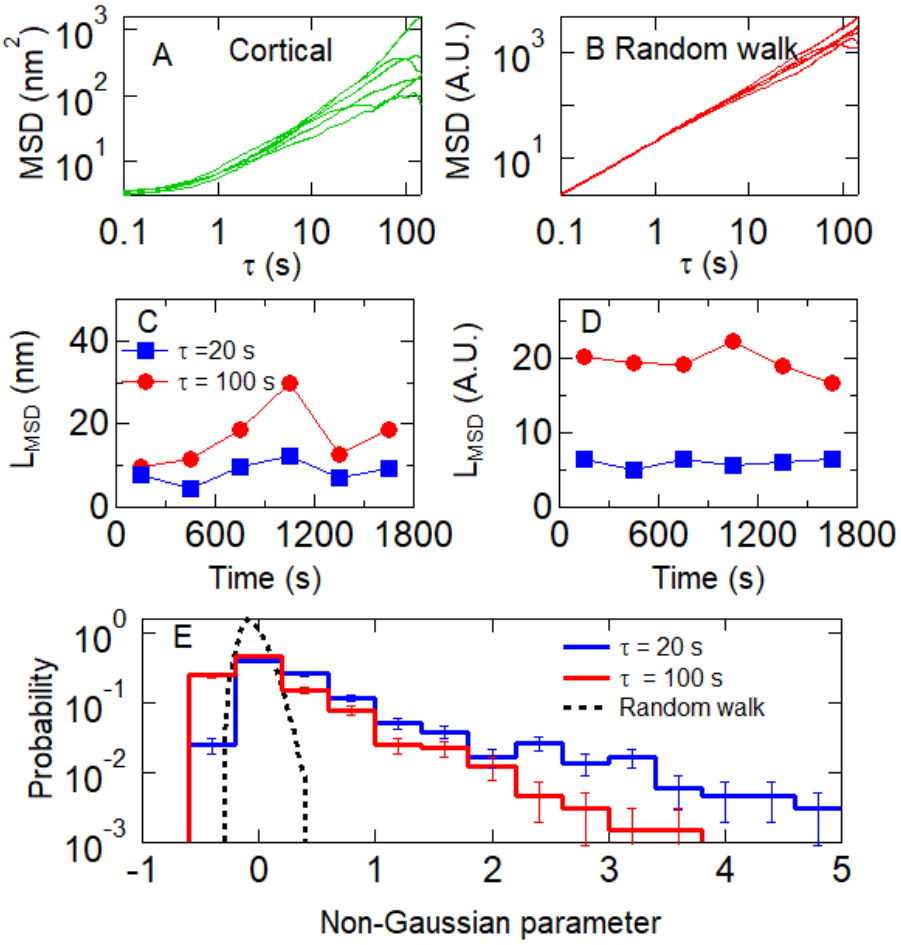

Figure 3.14. Spread of MSDs calculated for (A) a single cortical post over each of the six 300 s intervals in the 1,800 s measurement window. (B) Simulation showing spread in six MSDs for a Gaussian random walk over the same time interval. (C), (D) $L_{MSD} = [MSD(\tau)]^{1/2}$ for τ = 20 s and 100 s for the data shown in Panels A and B. (E) Distribution of the non-Gaussian parameter, α_2, computed over the full 1,800 s interval for cortical posts for N_{cells} = 14 cells. The distribution at τ = 20 s (black dashed line) for an 18,000 step Gaussian random walk is shown for comparison. Error bars were estimated as $1/\sqrt{N}$ for each bin in the probability distributions.

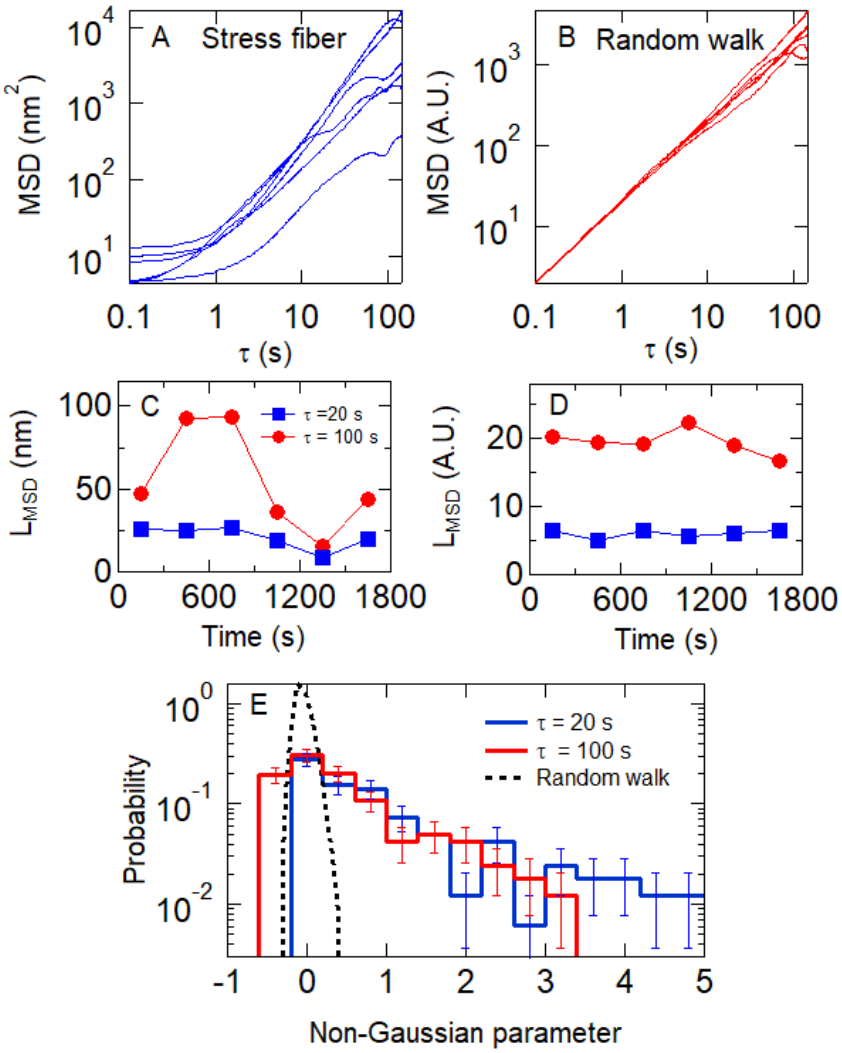

Figure 3.15 (A) Spread of MSDs calculated for a single stress fiber post over each of the six 300 s intervals in the 1,800 s measurement window. (B) Simulation showing spread in six MSDs for a Gaussian random walk over the same time interval (Reproduced from **Figure 3.14** B). (C), (D) $L_{MSD} = [MSD(\tau)]^{1/2}$ for τ = 20 s and 100 s for the data shown in *A* and *B,* respectively. (E) Distribution of the non-Gaussian parameter, α_2, computed over the full 1,800 s interval for stress fiber posts (N_{cells} = 13). The distribution at τ = 20 s (black dashed line) for an 18,000 step Gaussian random walk is also shown for comparison. Error bars were estimated as $1/\sqrt{N}$ for each bin in the probability distributions.

In summary, detailed analysis of single post trajectories reveals the signature of large displacement events, occurring randomly in time and space. The largest displacements, according to the anisotropy analysis, as implied in **Figure 3.12** B, have a

power-law distribution of amplitudes, λ_1, with a form roughly varying as $P(\lambda_1) \sim \lambda_1^{-3}$, (the marginal case leading to a non-convergent second moment). This distribution corresponds mathematically to the power-law tail seen in the MSD amplitudes, and leads to both the observed intermittency and large dispersion of MSD amplitudes and exponents. Combined with the super-diffusive character of the MSD time-dependence, these findings are suggestive of a highly non-Gaussian process consisting of random large jumps in time having a fat-tailed distribution of amplitudes [109, 110, 112]; here perhaps superimposed upon a background of normal Gaussian fluctuations.

3.9 The Cortex Displays Avalanche-Like Displacements or "Cytoquakes."

In physical systems, intermittent and collective motions of particles, having a power-law distribution of sizes, are generically called avalanches, like their namesakes in snow or sand. In this context, "size" might refer to different measures of the event, including its amplitude, its spatial extent, or the energy released, as these measures are typically found to be correlated. Were the cortical cytoskeleton prone to such avalanche-like instabilities, e.g. due to intermittent reconfigurations of tensile stress within the network, it would naturally explain the origin of the large displacement events we observe. In this picture, the energy released by the avalanches would scale as the work done on the posts and on the cortex (i.e. $\Delta E \sim (k_{\text{cell}} + k_{\text{post}})(L_{100})^2$). We have already seen that the probability distribution $P((L_{100})^2)$ has a fat tail approximating a power-law with an exponent of -2. In earthquakes (one example of avalanche-like dynamics), energy release

follows a similar power-law distribution, termed the Gutenberg-Richter law [113, 114]. Indeed, the largest post displacement events we observe are comparable in frequency and amplitude to those seen in a study of the temporal dynamics of individual membrane-bound tracer beads on human airway smooth muscle cells, by Alencar *et al.* [69], who coined the term "cytoquakes" to describe them. Alencar *et al.* also showed that the cytoquakes have power-law temporal correlations (Omori's law) resembling those in earthquakes.

To explore this picture further, we must examine whether the displacements we observe correspond to spatially extended reconfigurations (which we will henceforth call avalanches) and analyze their temporal behavior in greater detail. The parallel and spatially organized high-resolution measurements of cytoskeletal fluctuations enabled by the AMPAD arrays are ideally suited to such analysis. We searched for and isolated the largest spatially extended avalanche events in our dataset by cross-correlating the motions of pairs of nearest-neighbor posts, (separated by 4 μm). Specifically, we screened the cortical post deflection data set, divided into 90 second intervals, for occurrences of large deflections that were anti-parallel to each other and aligned with the two posts' line of centers, and which were nearly coincident in time. We broke the 1,800 s observation window of each cell into 90 s intervals, and first calculated the Pearson correlation coefficient for all near-neighbor, cortically associated micropost pairs. For each pair, the posts' deflections $\vec{r}_1(t)$ and $\vec{r}_2(t)$, measured relative to the posts' undeflected positions $\vec{R}_{01}$ and $\vec{R}_{02}$, respectively, were projected onto the line connecting the undeflected positions, $\vec{R}_{12} = \vec{R}_{01} - \vec{R}_{02}$. The Pearson coefficient of the parallel components of the posts' motion, $u_1 = \left|\vec{r}_1\right| \cos\theta_1$ and $u_2 = \left|\vec{r}_2\right| \cos\theta_2$, was calculated over the N = 900 video frames in each 90 s interval as

$$P = \frac{\sum_{i=1}^{N}(u_{1,i} - \bar{u}_1)(u_{2,i} - \bar{u}_2)}{\sqrt{\left(\sum_{i=1}^{N}(u_{1,i} - \bar{u}_1)^2\right)\left(\sum_{j=1}^{N}(u_{2,j} - \bar{u}_2)^2\right)}},$$

where $\bar{u} = \frac{1}{N}\sum_{i=1}^{N} u_i$ is the average over the interval, θ_1 is the angle between $\vec{r}_1(t)$ and $\vec{R}_{12}$, and θ_2 is the angle between $\vec{r}_2(t)$ and $\vec{R}_{12}$. Pairs with $P < -0.7$ on an interval were then further selected based on their motions parallel and perpendicular to $\vec{R}_{12}$ within that interval. Pairs with either perpendicular displacement $\Delta v = v_{\max} - v_{\min} > 30$ nm for either post, where $v_{\max}$ and $v_{\min}$ are the maximum and minimum values over the 90 s interval of the component of the post deflection $v = |\vec{r}|\sin\theta$ perpendicular to $\vec{R}_{12}$, or with parallel displacement $\Delta u = u_{\max} - u_{\min} < 20$ nm for either post were discarded. Application of these criteria to 14 cells (from 3 independent trials) and to 25 additional cells with single 90 s data ensembles (from 5 independent trials) with a total of 4848 near-neighbor low-traction force post pairs yielded a dataset of 359 micropost pairs with highly anti-correlated motion directed largely along their line of centers.

We identified from within this dataset events containing synchronized steps in the deflection traces of both posts within a pair that were opposite in direction (i.e., anticorrelated). The parallel components of the posts' trajectories $u(t)$ were smoothed via boxcar averaging over a 10 s range, and then the 1st derivative du_s/dt of the smoothed traces $u_s(t)$ was computed. Peaks in the 1st derivative traces with absolute value $|du_s/dt| > 4$ nm/s were identified using the Igor Pro software's built-in peak finder, and their positions were then refined by fitting the du_s/dt data with a 2nd order polynomial over an 8 s interval

centered on the initially identified peak. These yielded measurements of the peak positions that were accurate to 0.1 s. This accuracy was determined from uncertainties in the parameters of the polynomial fits, which were estimated from the range for each parameter where χ^2 increased from its minimum value by the factor $(1 + 1/N_{\text{free}})$, where $N_{\text{free}} = N_{\text{data-points}} - N_{\text{model-parameters}}$ is the number of free parameters [86]. Pairs with synchronized steps were then identified as those where peaks from each post were within 5 s of each other. We also required that the steps lasted for at least 5 data points (0.5 seconds) to prevent inclusion of errors in tracking the microposts' positions. This restriction, combined with the threshold on velocity for step detection described above, enabled us to pick out step events with large amplitudes while excluding effects due to low frequency noise. We note that this introduced a lower bound for possible step detection (0.5 s duration), whereas the threshold on velocity may have excluded some long-duration events. Therefore, our observed anti-correlated motions likely do not represent the overall time scale distribution of avalanche-like events that may exist in cells. We found 68 synchronized step events via this method. As a statistical control, we screened for similar events on cortical posts that were not nearest neighbors. Over our set of 14 cells with 1,800 s data ensembles and 25 additional cells with single 90 s data ensembles, we observed 4,848 nearest-neighbor cortical micropost pairs. Within this data set, we found 68 avalanche events that were large enough to span across two posts, while on a matched control ensemble we found only 2, ($p < 10^{-5}$). (Unfortunately, the much smaller set of stress fiber-associated microposts did not contain enough near-neighbor pairs to give sufficient statistical power for a similar analysis.)

Two typical avalanche events are shown in **Figure 3.16** *A* and **Figure 3.16** *B*. We did not observe any temporal correlation between pairs of events, such as expected if contractile events were followed by expanding events on the same pair of posts. Significantly, cells with myosin inhibited by blebbistatin or Y27632 yielded no avalanches ($p < 10^{-5}$). To assess the possibility of dipolar deformations, we searched for near neighbor micropost pairs with highly correlated (same direction) parallel motion ($P > 0.7$, $\Delta u > 20$ nm, $\Delta v < 30$ nm). This yielded 437 candidate pairs, but none showed synchronized correlated steps. We also searched for highly anti-correlated tangential motion within pairs ($P < -0.7$, $\Delta u < 30$ nm, $\Delta v > 20$ nm). This yielded 17 candidate pairs, of which none showed synchronized anti-correlated steps. This statistical analysis provides an independent verification of large-scale reconfiguration of the cortex, in addition to the power-law distribution of single post displacements discussed earlier. The motion of the post trajectories in a single avalanche is quite irregular (as opposed to being linear and directed), consistent with their being driven by multiple microscopic rearrangements of the cytoskeleton that are distributed over space and time (rather than a single rearrangement). The observation that avalanches only display anti-correlated motion parallel to the line of centers is consistent with our expectations that the displacement field should nonetheless display roughly quadrupolar symmetry [38, 115] at the longest length scales (as expected for a two-dimensional viscoelastic sheet), and also rules out several possible confounding explanations, like cortical de-adhesion, or out of plane motion (e.g. endocytosis or microvillus formation). See **Figure 3.17** for details. We also note that waves of actin polymerization [102-104] would be expected to give correlated, parallel transverse

displacements of pairs of posts, which we do not observe, suggesting that they are not responsible for our step-like displacements.

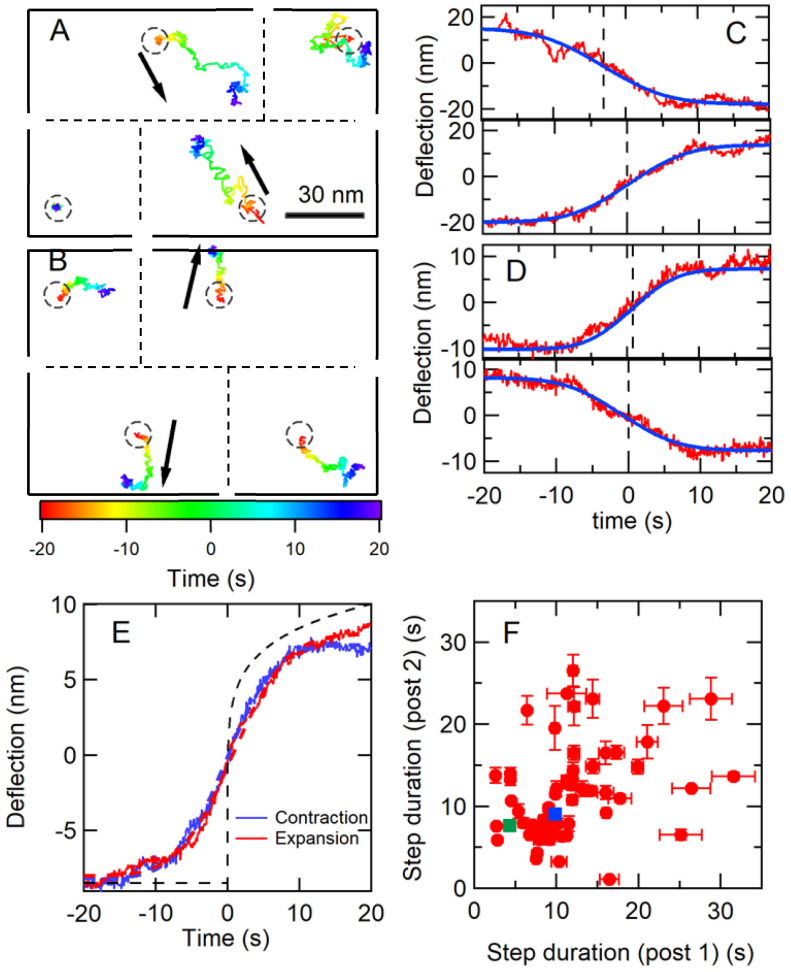

Figure 3.16. Anti-parallel micropost motions reveal cortical avalanche dynamics. (A), (B) Examples of strongly anti-correlated steps in the 2D trajectories of nearest neighbor micropost pairs. The black arrows indicate each post's overall direction of motion. The trajectories are color-coded to indicate time. Circles indicate the posts' resting positions. The relative positions of the posts in the pair and the two adjacent posts are shown, but their separations are not to scale. (C), (D) Displacements for the posts in the pairs in Panels A and B projected onto the line of centers; experiment (red curves) and error function fit (blue curve). The time $t = 0$ was set at the peak of the 1st derivative for the bottom trace. (E) Step profiles averaged over 12 contracting (blue) and 19 expanding pairs (red). Dashed red and blue lines show fits to error functions to extract average step durations $t_{contract} = 9.5 \pm 0.2$ s and $t_{expand} = 8.8 \pm 0.1$ s, and average step heights $h_{contract} = 8.2 \pm 0.1$ nm and $h_{expand} = 8.8 \pm 0.2$ nm. The ratio of step sizes was restricted to the range $0.7 < h_2/h_1 < 1.4$, with

both h_1 and h_2 > 6 nm. Dashed black line shows calculated viscoelastic creep response to a step stress at t = 0, with deflection $\propto t^{\beta}$, based on measured cell rheology (**Figure 3.1** E). (F) Scatter plot of step durations for pairs of posts, pooling the contracting and expanding pairs. Determination of error bars on individual points is described in Section 2.5. The blue and green squares correspond to the data in Panels C and D, respectively. The lack of close correlation (Pearson coefficient = 0.4) suggests that avalanches proceed through multiple, non-synchronous events.

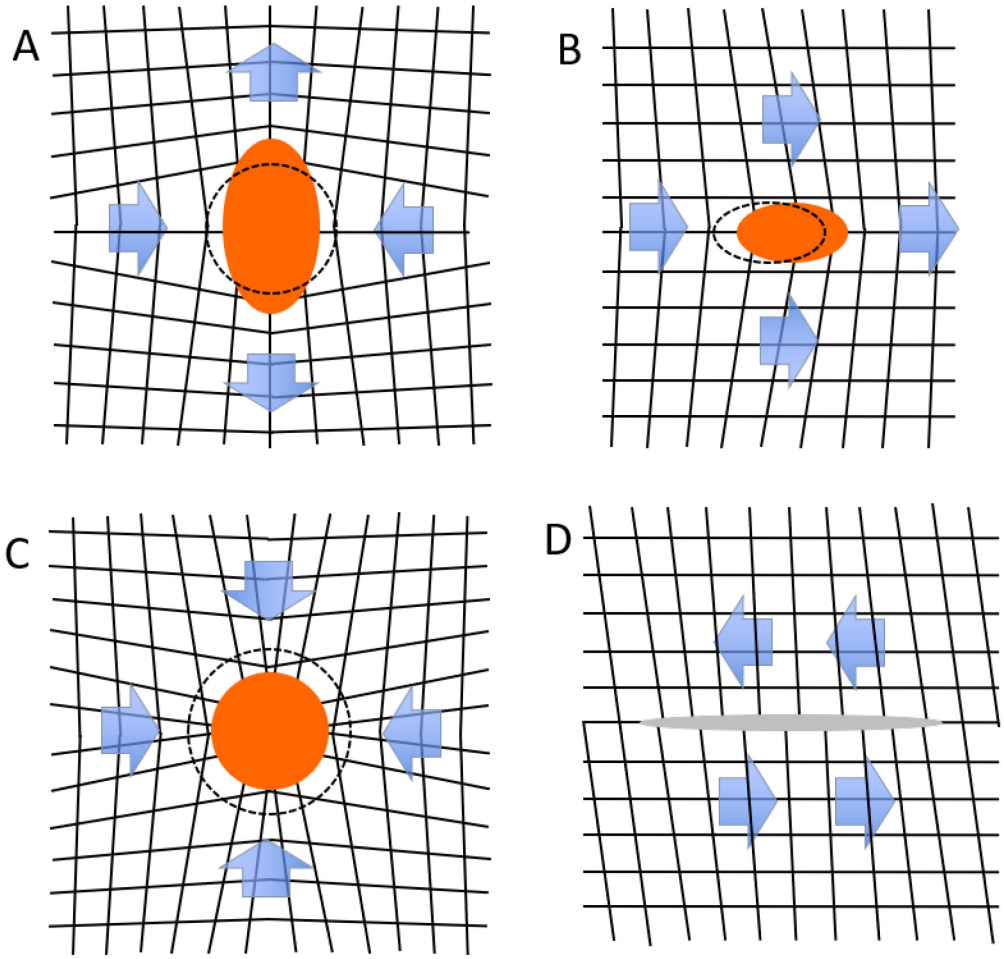

Figure 3.17. Schematic of the possible symmetries of cortical avalanches. Different strain fields (grid lines) can result from a localized rearrangement in a two-dimensional sheet; the shape change is represented by an initial shape/position (dashed line) and the final configuration (orange solid). (A) A local shape change with a quadrupolar symmetry (circle to ellipse) gives rise to a "stresslet" strain field with regions of anti-parallel contraction and expansion (arrows), closely resembling our two-post data. This mode requires no external force, torque or local compression. (B) The lateral displacement of small region creates a "stokeslet" strain field consisting of parallel displacements. This mode requires a body force from outside the plane; in the cell case this could consist of abrupt de-adhesion of a small region from the substrate. The lack of our observations of

such “parallel” two-post displacements rules out such mechanisms. (C) The compression (or expansion) of a small region leads to a “monopole” strain field, and anti-parallel contraction (or expansion). This mode either requires physical compressibility of the network, or out of plane deformation. This mode does not naturally account for why expansion and contraction events in our data are equal in number and show identical amplitudes and dynamics but is consistent with the observed anti-parallel motion. (D) In an externally sheared sheet, a “fault line” (gray domain) can locally relax the network, giving rise to a “rotlet”-like strain field. This is a common mode in earthquakes but produces displacements that are transverse to the line of centers, which we do not observe.

To parameterize the avalanches, we fit the unsmoothed trajectories $u(t)$ centered over a ±20 s range about the peak positions in du/dt with error functions $f(t) = A + h \cdot erf(\frac{t - t_0}{\Delta t})$, where $erf(x) = \int_{-x}^{x} e^{-z^2} dz$, to obtain each step’s characteristic duration Δt and height h (**Figure 3.16** C and **Figure 3.16** D). Uncertainties in the fit parameters were estimated using χ^2, as described above in Section 2.5. To obtain a measure of the average shape of a step, we selected events with height ratios in the range $0.7 < h_2/h_1 < 1.4$ for the two posts in the pair, and also with h_2 and $h_1 > 6$ nm. From the population of 68 events, this yielded 19 expanding and 12 contracting events. Surprisingly, the average amplitude and functional form of expanding and contracting events are indistinguishable (**Figure 3.16** E), and both types were seen with roughly equal probabilities. This is unexpected, as the activity of myosin filaments is strictly contractile; experiments with in vitro actomyosin gels [60] show contractile events in the network due to myosin binding and sliding activity on actin filaments, followed by abrupt network expansion events when the myosin unbinds the actin. Notably, the shape of these events is qualitatively different from that expected for the response to a single step in stress, which can be computed from the measured power-law rheology (dashed line in **Figure 3.16** E) [116, 117], and is inconsistent with a single microscopic rearrangement event. Moreover, the deflection durations for pairs of neighboring posts were only weakly correlated (**Figure 3.16** F), and the deflection occurrence times were non-coincident in time by 1-2 seconds compared to a 0.1 s uncertainty. Taken together, all these observations strongly suggest that the avalanches display spatio-temporally complex evolution, e.g., a series of rearrangement

events distributed overs space and time, rather than motion that is abrupt in time, with a regular quadrupolar form occurring coincidentally in time everywhere, as seen in gels [60].

3.10 Discussion

In this chapter, we have shown that AMPADs are a new tool to understand the dynamics and rheology of the cytoskeleton. This system combines key features comparable to other leading techniques, with a regular array of probes that can map the mechanical response, as is possible with AFM [41-44], and measure cellular fluctuations and local rheology simultaneously with high temporal resolution and ligand specificity, as with magnetic twisting cytometry [8, 84, 101]. In this study, the use of AMPADs has allowed us to make a detailed examination of the mechanics of the cell cortex and stress fibers. We find that the cortex displays both power-law rheology and intermittent fat-tailed fluctuations that are correlated into large avalanche-like displacements spanning at least 4 μm in spatial extent. In isolation, it would be difficult to imagine how a system consisting of simple building blocks could display all these phenomena. However, recent studies describe and explain the origin of rearrangements having a power-law amplitude distribution [100], super-diffusive motion and power-law rheology [54], and avalanches [97] in gels, emulsions and sandpiles, respectively, under deformation. The key features these models have in common is that these systems self-organize into a state where many degrees of freedom are near a point of instability, called a marginal solid, and are capable of plastic rearrangements when deformed. The resulting behavior is similar to the common notion of avalanches, in which motion along one unstable degree of freedom can trigger (destabilize) others in a complex chain reaction to form an avalanche [97]. In these solid

materials, power-law rheology is due to stress relaxation due to plastic rearrangements driven by super-diffusive fluctuations [54].

Our cell results suggest a new way of thinking about the architecture of cytoskeletal networks, as our observations could be naturally explained if the cytoskeleton's constituents self-organize into a mechanically marginal state, akin to jammed [97, 99, 100] and soft-glassy materials [51, 52, 54, 99, 100]. In the cortex, single myosin mini-filaments have been found to self-assemble with other proteins into "contractile units" (CUs) during the cell spreading process that have complex, non-linear mechano-chemical behavior [91] that can be modeled by a collection of two-state molecular motors [118]. In the fully spread cells we studied, we hypothesize that CUs and actin filaments robustly self-organize into tensile networks which are both plastic and whose steady states are marginally stable [97], where a small local rearrangement can trigger an avalanche of structural reconfiguration that arrests only when the network reaches a new marginally stable state. The super-diffusive fluctuations that are characteristic of such avalanche dynamics in turn drive plastic rearrangements [54], which as in soft-glassy matter would then lead to the previously unexplained power-law rheology of the cytoskeleton.

As we have shown, high-resolution measurements of cells' active matter dynamics can offer a new window into cellular biophysics. With its combination of integrated, high precision and spatially correlated measurements of cytoskeletal fluctuations and local, magnetically driven measurements of cellular rheology, the approach described here has enabled the elucidation of the complex spatial and temporal correlations in the active dynamics of the actomyosin cortex. These results suggest that the physics of jammed materials and plastic deformation may be the origin of cytoskeletal active mechanics,

fluctuations and rheology, with significant implications for future models of the cortex, and for efforts to connect molecular-scale machinery to cellular-scale behavior and dynamics.

Chapter 4 Cortical avalanches exist across multiple substrate stiffnesses and cell types

4.1 Introduction

In the previous chapter, I demonstrated the existence of non-Gaussian statistics and avalanche-like fluctuations in the actin cortex in 3T3 fibroblasts. In this chapter, I describe an expansion of the analysis in the previous chapter to 3T3 fibroblasts on other substrates with different stiffnesses as well as to other cell types. We found that the phenomena previously discussed persist across the cell types and substrate stiffnesses measured, suggesting that the non-Gaussian fluctuations are an intrinsic feature of the cellular actin cortex.

I would like to thank Katherine Xiang and Shankar Sivarajan for their contributions to the data acquisition and analysis described in this chapter.

4.2 Traction force variation across substrate stiffness and cell types

As described in Section 2.2.3, the PDMS microposts' effective spring constants follow beam bending theory as $k = \frac{3E\pi d^4}{64L^3}$ under small deflections. Therefore, by changing the microposts' height L one can change the substrate stiffness easily, as shown

in **Table 2.1**. We cultured 3T3 fibroblasts on micropost substrates composed of posts with 1.8 μm diameters arranged in a hexagonal lattice with 4 μm center-to-center spacing, and measured each cell for 30 minutes. The posts' height varied from 9.1 μm to 5 μm, with corresponding stiffness ranging from 5.5 nN/μm to 22.3 nN/μm.

To compare the mechanical response of cells across different substrate stiffness, we first measured the cellular traction force, defined as $\vec{F} = k\Delta\vec{r}$, where $\Delta\vec{r}$ is the deflection of a post from its resting position. The resting position is determined by interpolation from the hexagonal lattice defined by the nearby unengaged posts [71-73]. **Figure 4.1** A shows the distribution of traction forces for a 3T3 fibroblast on a substrate with k = 5.5 nN/μm. To quantify the traction force on a per-cell basis, we then averaged the traction force magnitude on each post across each cell $\left\langle \left|\vec{F}\right| \right\rangle = \frac{1}{N}\sum k\left|\Delta\vec{r}\right|$. As presented in **Figure 4.1** B, we see some tendency for the average traction force to increase with substrate stiffness, consistent with previous results on these substrates [79].

We also studied a variety of cell types. Since we found only modest variations in traction force for the same cell type on different substrate stiffnesses, we chose substrates based on experimental considerations, i.e. to ensure that posts with the largest deflections (typically those under cell edges) had small enough displacements to allow accurate determination of their deflections with our particle tracking algorithms and to allow determination of the traction forces applied to them from linear beam bending theory. We first studied neonatal rat cardiac fibroblasts (CFs) and cardiac myofibroblasts (CMFs), which were transformed from the fibroblast phenotype under the presence of TGF-β growth factor. To prevent spontaneous transformation of CFs to CMFs, we cultured CFs with SD-208 to block them from effects of any TGF- β in the ambient culture media [119].

Both cell types were cultured on substrates with stiffness of k = 22.3 nN/μm. As shown in **Figure 4.1** C, we found that both CFs and CMFs showed significantly larger traction forces compared with 3T3 fibroblasts ($p<0.05$, $N_{CF} = 8$, $N_{CMF} = 10$ and $N_{3T3} = 8$). we also found the averaged traction force in CMFs is significantly higher ($p<0.05$, $N_{CF} = 8$ and $N_{CMF} = 10$) than for CFs, which is consistent with previous results [120] (A more detailed comparison of contractility in CFs and CMFs will be discussed in Section 6.2). We next assessed two representative non-fibroblast cell types, Human Embryonic Kidney (HEK) and Human Bone Osteosarcoma Epithelial Cells **(**U2OS). Compared with 3T3 fibroblasts on substrates of corresponding stiffness (k = 15.7 nN/μm for HEK and k = 5.5 nN/μm for U2OS) (**Figure 4.1** C), HEK cells showed similar average traction forces while the traction forces for U2OS cells were higher ($p<0.05$, $N_{U2OS} = 11$ and $N_{3T3} = 19$).

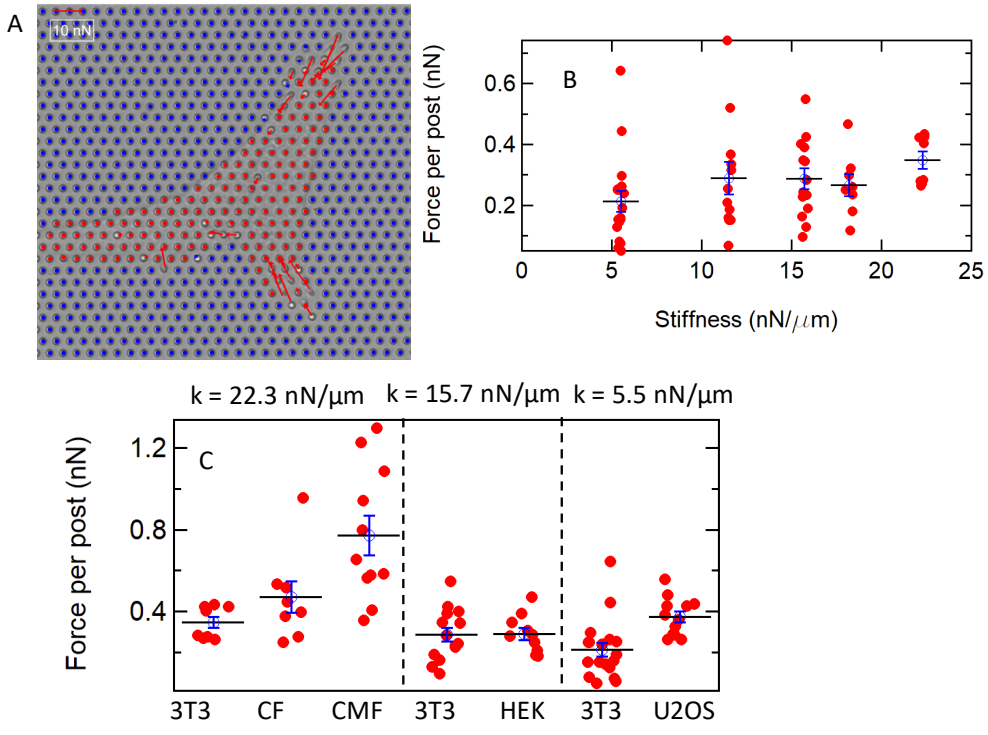

Figure 4.1 (A) traction force map of a 3T3 fibroblast cell on k = 5.5 nN/μm substrate. The red arrows indicate cellular traction force vectors. Blue dots show background posts not in

contact with the cell. (B) Dependence of traction force per post on substrate stiffness. Each data point is the average traction force ($\left\langle \left| \vec{F} \right| \right\rangle = \frac{1}{N} \sum k \left| \Delta \vec{r} \right|$) for an individual cell. (C) Dependence of traction force per post on cell type. Each cell type is compared with 3T3 fibroblasts on the corresponding substrate stiffness.

4.3 Variation in fluctuations across cell types and substrate stiffness

To assess cytoskeletal dynamics, we recorded each cell for 30 minutes and measured each post's fluctuations. In **Figure 4.2** A, we show sample deflection traces of two posts for a cardiac myofibroblast (CMF) on a k = 22.3 nN/μm substrate, with the red trace indicating a cell-associated post and the blue trace showing a post outside of the cell. We then characterized the fluctuations of the cell-associated posts through their mean square displacements (MSDs), calculated as $|\Delta r^2(\tau)| = \langle (\mathbf{r}(t+\tau) - \mathbf{r}(t))^2 \rangle$, where $\mathbf{r}(t+\tau) - \mathbf{r}(t))$ is the deflection over lag time τ. In **Figure 4.2** B, we show sample MSD curves against lag time on a log-log scale. We parameterized these MSD curves using their magnitude at τ = 10 s and the MSD exponent in the range 5 s $\leq \tau \leq$ 10 s (as described in Section 3.4). **Figure 4.2** C and D show the distribution of these two parameters over the whole cell. As illustrated, microposts underneath the cell periphery showed higher MSD magnitudes as well as MSD exponent, which is consistent with our previous findings on 3T3 fibroblasts (Section 3.2). To quantify this, we show the MSD magnitude at τ = 10 s versus traction force on each post (**Figure 4.2** E). We found that the distribution of MSD magnitude can be classified based on the posts' traction force: posts with traction force < 2 nN cluster at lower MSD magnitude while posts with traction force > 10 nN scatter over larger MSD

magnitude. We segmented the microposts for each cell into subpopulations based on traction force, and show their distribution across the cell in **Figure 4.2** G. As expected, higher traction force posts were mostly present at the cell periphery while lower traction force posts were concentrated in the middle of the cell. Following the same notation as in the previous chapter, we associate these two classes of posts with stress fibers and the cell cortex, respectively. The same set of analysis was done for 3T3 cells on various substrate stiffnesses and for other cell types. Examples for each case are shown in **Figure 4.3 - Figure 4.6** (post stiffness variation) and **Figure 4.7-Figure 4.9** (other cell types).

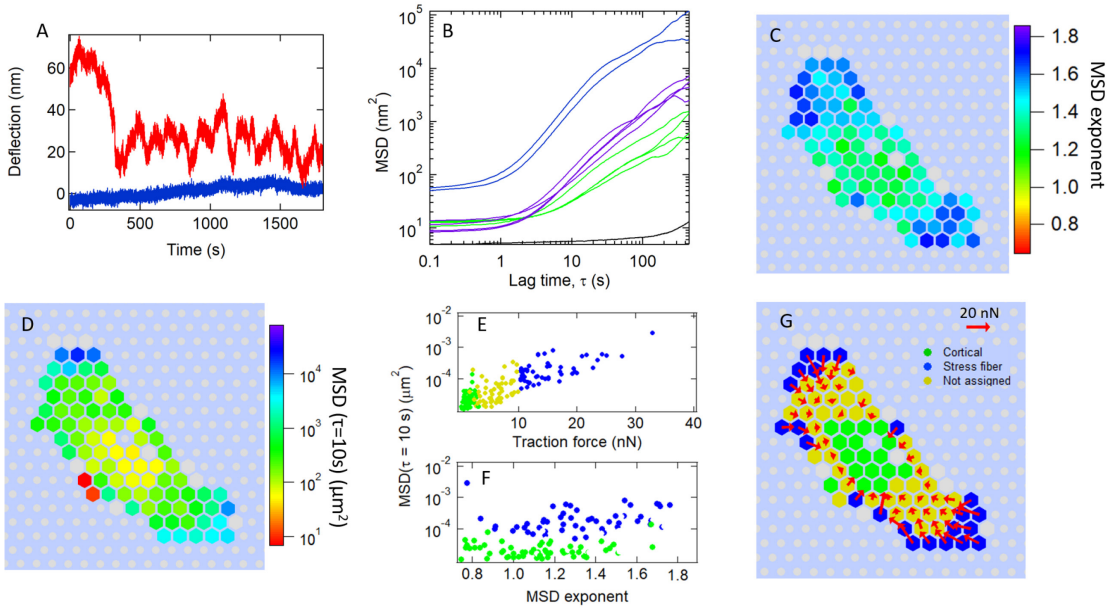

Figure 4.2 Micropost deflection fluctuations for a cardiac myofibroblast. (A) Deflection trace of a cardiac myofibroblast-associated micropost (red) and a background micropost (blue) over 30 minutes. (B) Mean square displacements calculated based on traces such as those in (A). The traces' color indicates the MSD power law exponent α over the range 5 s ≤ τ ≤ 10 s as given by the scale in panel C. The black trace is calculated based on the background post in A. (C) Distribution of power law exponent α over 5 s ≤ τ ≤ 10 s. Graph follows the same color code as in **Figure 3.4**. (D) Distribution of MSD magnitude at lag time = 10 s. Graph follows the same color code as in **Figure 3.4**.B and C. (E) Dependence of MSD magnitude on traction force. Color code is the same as in Fig **Figure 3.4** F. (F) Separation of MSD magnitude and MSD exponent after differentiated cortical and stress fiber associated posts. (G) Distribution of cortical and stress fiber posts across cell, and the associated traction force vector. Color code is the same as in **Figure 3.4** D.

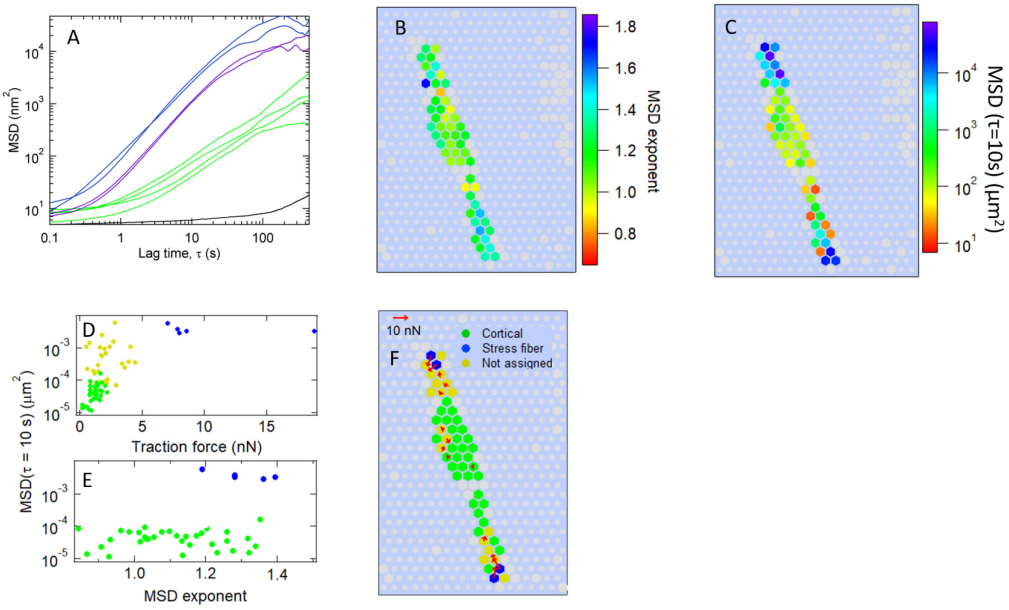

Figure 4.4 (A)-(F) Analysis of fluctuations for a 3T3 fibroblast on a substrate with micropost stiffness k = 22.3 nN/μm corresponding to **Figure 4.2** (B)-(G).

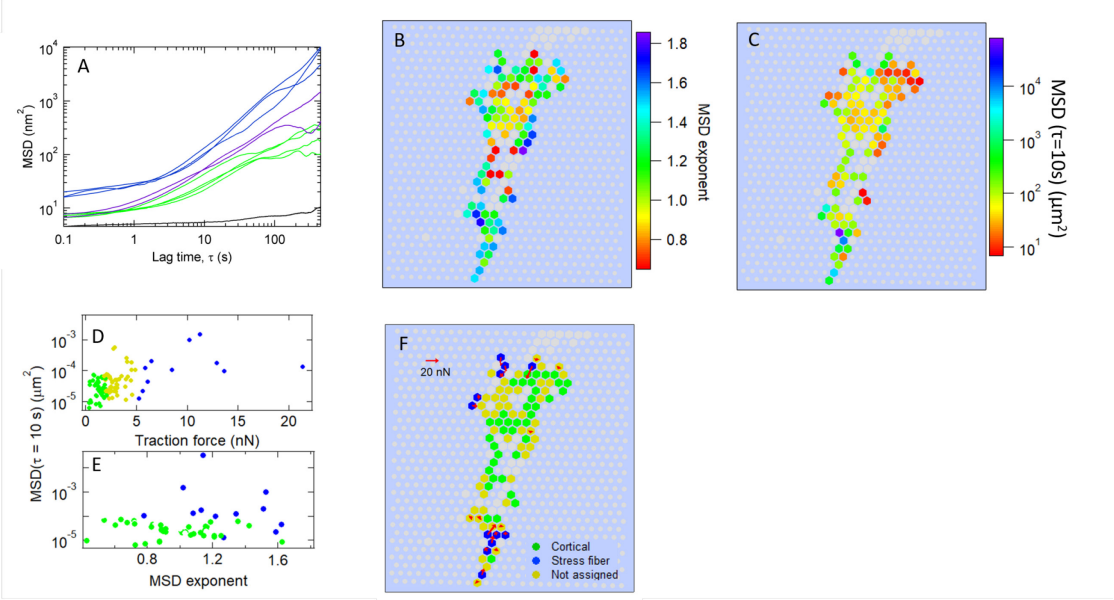

Figure 4.3 (A)-(F) Analysis of fluctuations for a 3T3 fibroblast on a substrate with micropost stiffness k = 18.2 nN/μm corresponding to **Figure 4.2** (B)-(G).

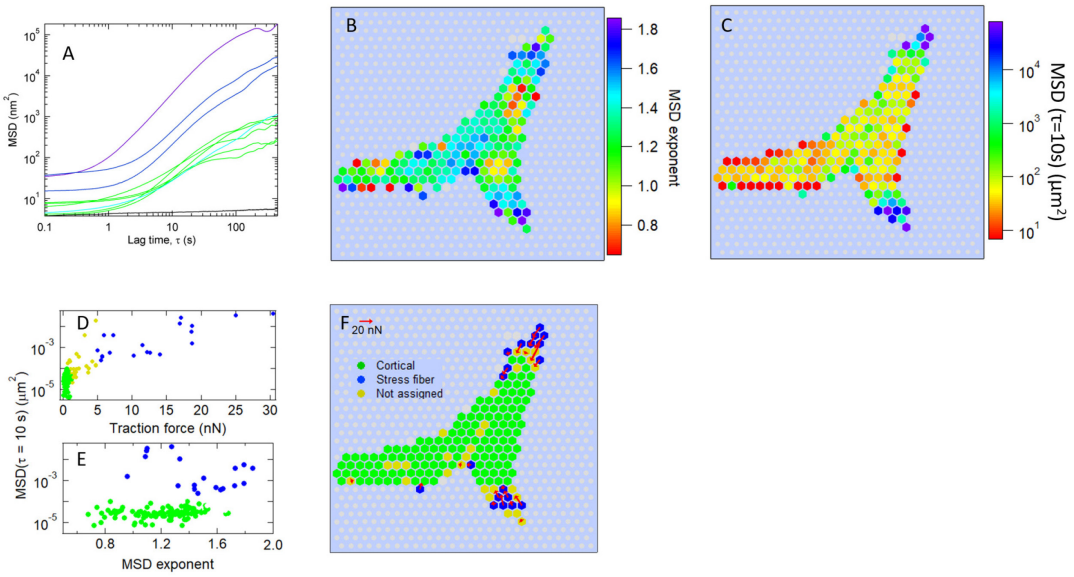

Figure 4.5 (A)-(F) Analysis of fluctuations for a 3T3 fibroblast on a substrate with micropost stiffness k = 11.5 nN/μm corresponding to **Figure 4.2** (B)-(G).

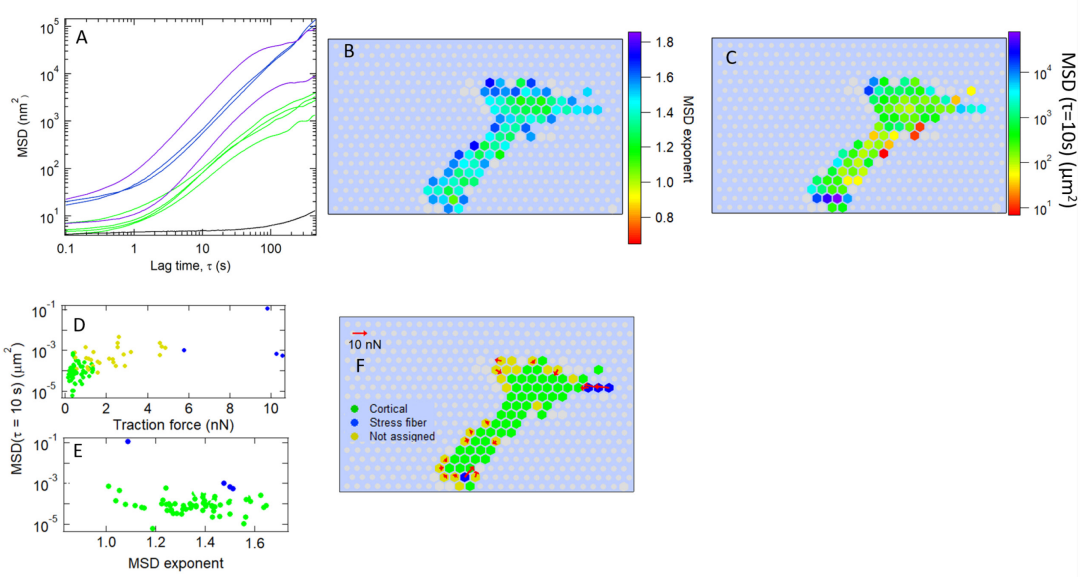

Figure 4.6 (A)-(F) Analysis of fluctuations for a 3T3 fibroblast on a substrate with micropost stiffness k = 5.5 nN/μm corresponding to **Figure 4.2** (B)-(G).

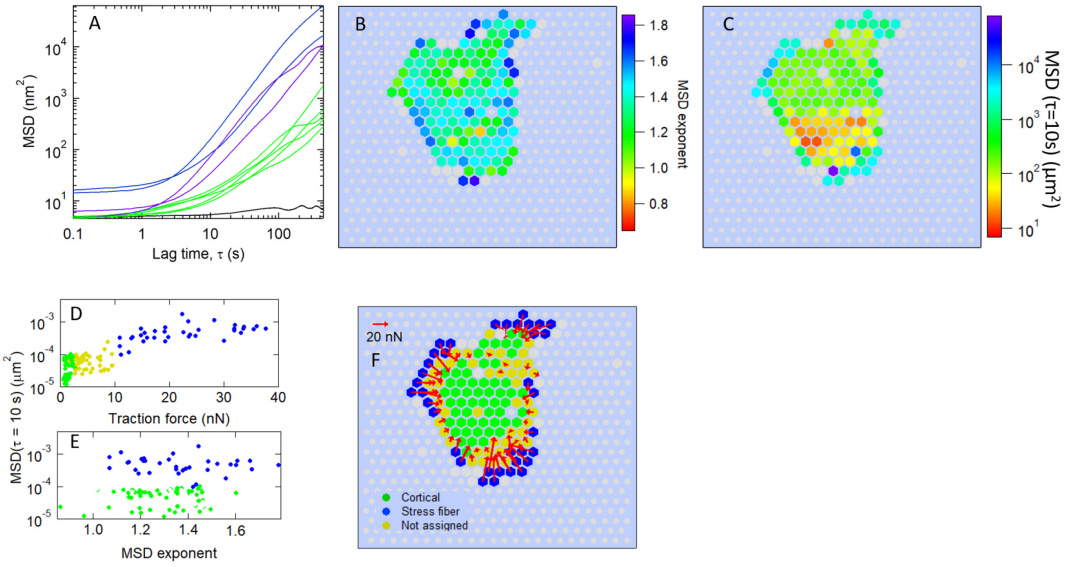

Figure 4.7 (A)-(F) Analysis of fluctuations for a cardiac fibroblast corresponding to **Figure 4.2** (B)-(G)

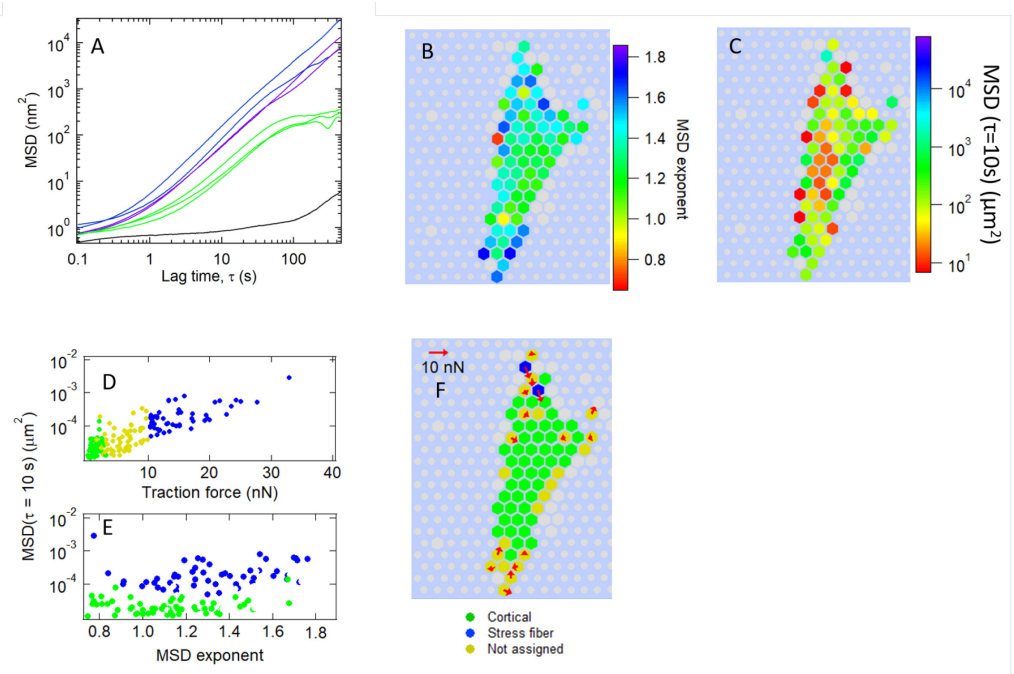

Figure 4.8 (A)-(F) Analysis of fluctuations for a HEK cell corresponding to **Figure 4.2** (B)-(G)

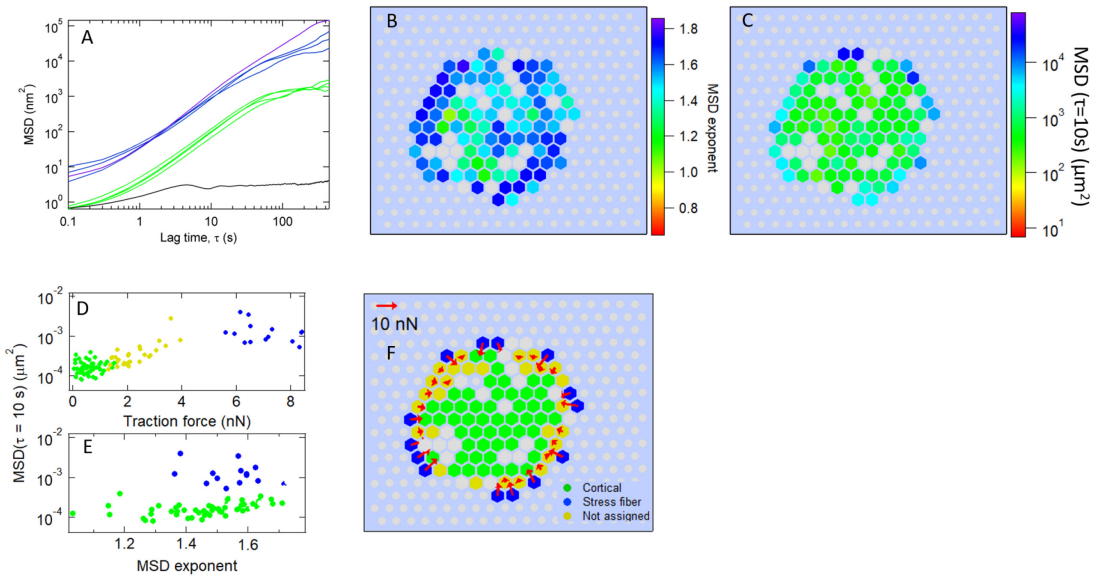

Figure 4.9 (A)-(F) Analysis of fluctuations for a U2OS cell corresponding to **Figure 4.2** (B)-(G)

To compare the dynamical properties across post stiffnesses, we calculated the average MSD magnitude at τ = 10 s (L_{10}) over all posts in each cell and also converted this measure to the force from fluctuations (kL_{10}). As illustrated in **Figure 4.10** A and B, we find that the fluctuation magnitude shows no clear trend with substrate stiffness, thus leading to an linear increase in fluctuation force with substrate stiffness. These results are consistent with cellular rigidity sensing [121, 122].

We also compared fluctuations across different cell types, using 3T3 fibroblasts on the corresponding substrate stiffness as a reference. As illustrated in **Figure 4.10** C, cardiac myofibroblasts have larger fluctuations compared with cardiac fibroblasts ($p<0.01$, N_{CF} = 8, N_{CMF} = 10), and U2OS have different fluctuational magnitude compared with 3T3 fibroblasts ($p<0.05$, N_{U2OS} = 11 and N_{3T3} = 19), however no significant differences were

observed between HEKs and 3T3 fibroblasts on the same substrate stiffness (N_{HEK} = 12, N_{3T3} = 12). These results indicate dynamical fluctuations vary in magnitude across cell types.

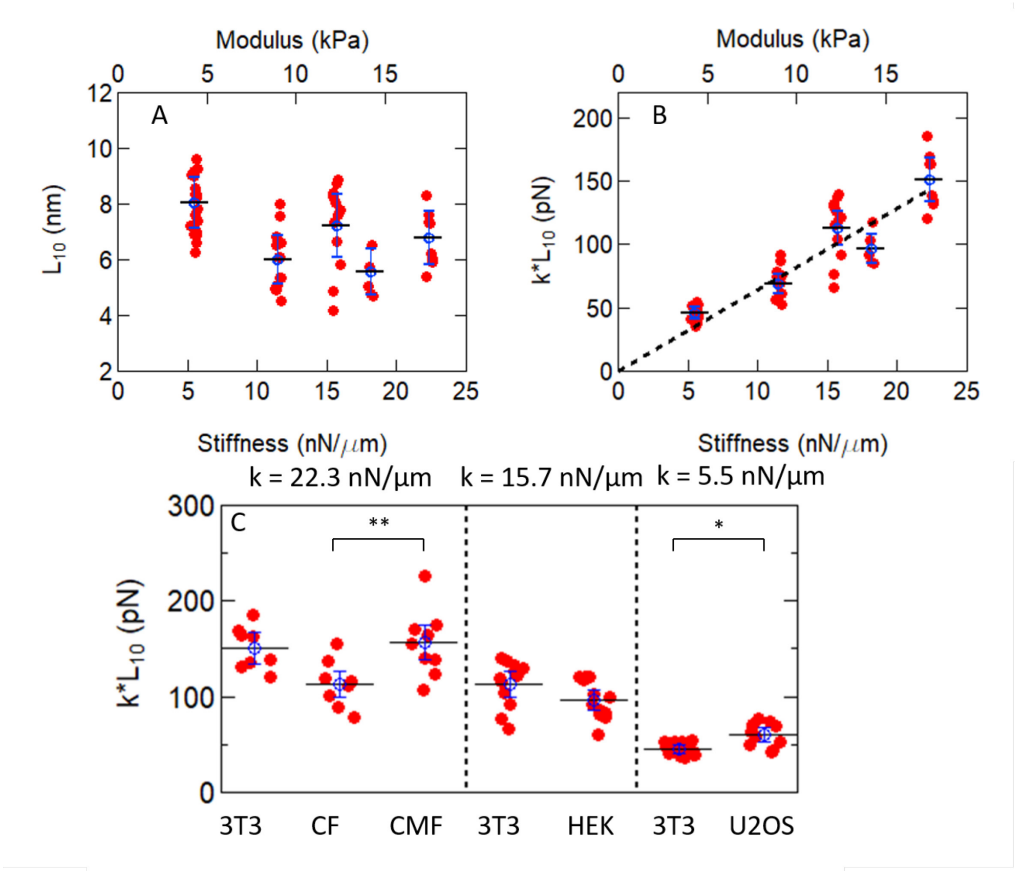

Figure 4.10 Dependence of (A) average fluctuation magnitude (L_{10}) and (B) converted fluctuational force from L_{10} on substrate stiffness. The black dashed line is a linear fit to the average fluctuational forces at different stiffnesses. (C) Dependence of fluctuational force on cell type. Each cell type was compared 3T3 fibroblast on the same substrate stiffness (*: $p < 0.05$, **: $p < 0.01$). Each data point corresponds to a cell.

We also examined the MSD exponent distribution for the cell types other than 3T3 fibroblasts (corresponding to **Figure 3.11** C). **Figure 4.11** shows the MSD exponents for cortical and stress fiber posts for four representative cells in each cell type. Similar to 3T3 fibroblasts, we observed large variations both within and between cells, and that the MSD exponents in the stress fiber posts α_{sf} are significantly larger than for cortical posts α_c ($p <$

0.01 for each cell type from paired T-tests comparing cortical and stress fiber posts in each cell).

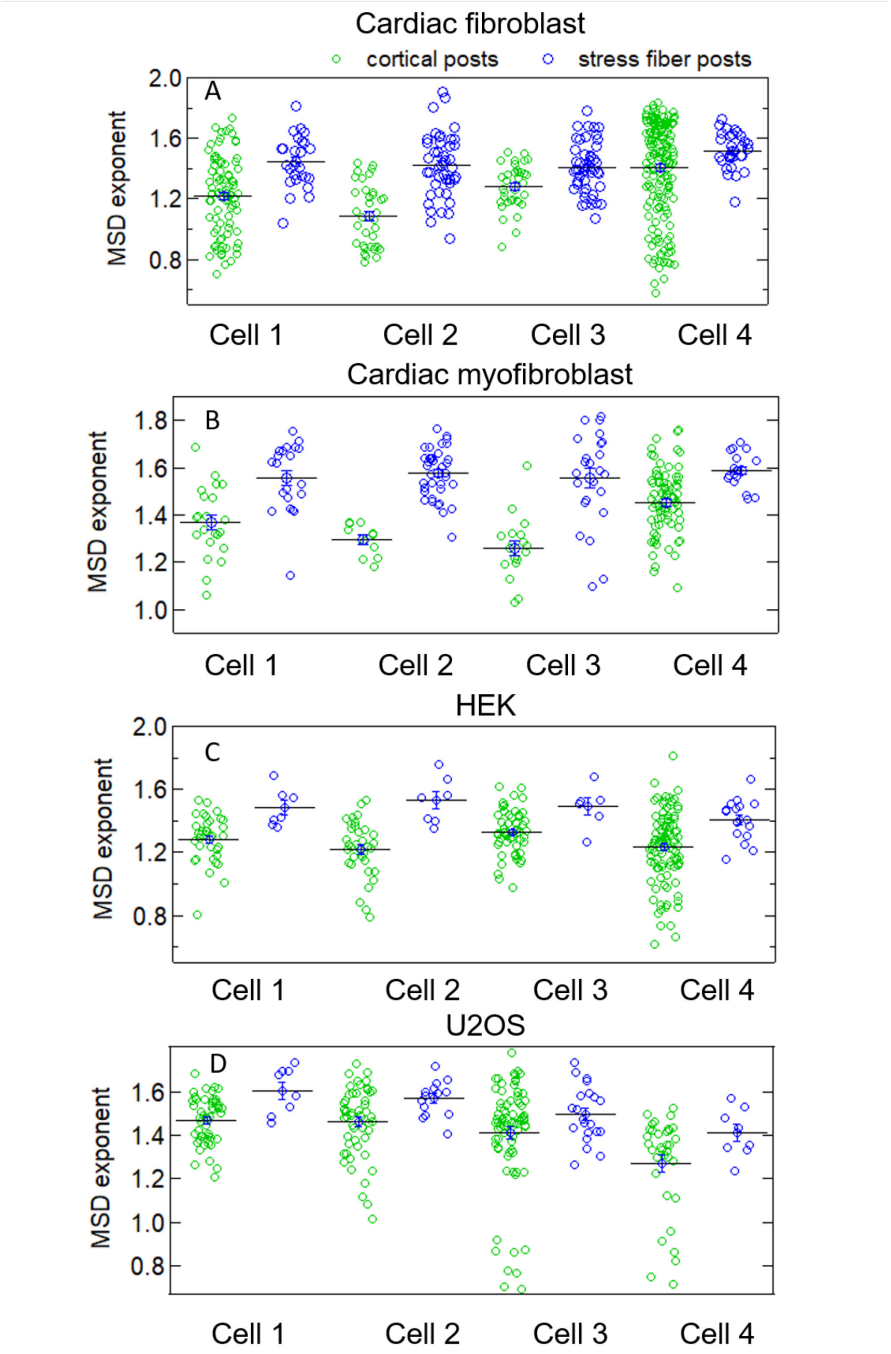

Figure 4.11 Scatter plot of MSD exponent for individual posts for four representative cells of different cell types. The black lines show the mean and the error bar shows the standard error of the mean. Statistical comparisons were done over all the cells for each cell type and presented as mean ± standard error. Significance tests were done to compare stress-

fiber (blue) and cortical (green) posts for each cell type by paired T-tests. (A) cardiac fibroblasts: α_{sf} = 1.42 ± 0.03, α_c = 1.27 ± 0.05, N_{cell} = 8, p < 0.01. (B) cardiac myofibroblasts: α_{sf} = 1.52 ± 0.03, α_c = 1.30 ± 0.02, N_{cell} = 10, p < 0.01 (C) HEK cells: α_{sf} = 1.45 ± 0.04, α_c = 1.23 ± 0.02, N_{cell} = 12, p < 0.01 (D) U2OS cells: α_{sf} 1.48 ± 0.04, α_c = 1.38 ± 0.04, N_{cell} = 11, p < 0.01.

4.4 Actin cortical fluctuations are highly non-Gaussian

So far, we have shown variations in the cytoskeletal fluctuations within cell types (Section 3.7) and between cell types (Section 4.3). In order to study the fluctuations in more detail, we need to study the distribution of displacements over a given lag time, also known as a Van Hove distribution curve. To reduce the experimental noise at shorter lag times, we averaged the fluctuation traces (measured at 10 frames/s) over every 10 frames and calculated the displacement distributions based on the resulting 1 sample/s data. In **Figure 4.12**, we present the Van Hove curves at lag times ranging from 1 s to 300 s for 3T3 fibroblasts on k = 15.7 nN/μm substrates. For particles driven by thermal fluctuations, their Van Hove curves will follow a Gaussian distribution whose width grows as $\sqrt{\tau}$. Interestingly in our experimental data, we found that the spread in the displacement distributions was highly non-Gaussian. However, as suggested by the discussion in Section 3.8, apparent non-Gaussian statistics can rise from aggregating a population with heterogenous Gaussian fluctuations. To rule that out, one needs to apply a dimensionless measurement of the posts' displacements that takes this heterogeneity into account.

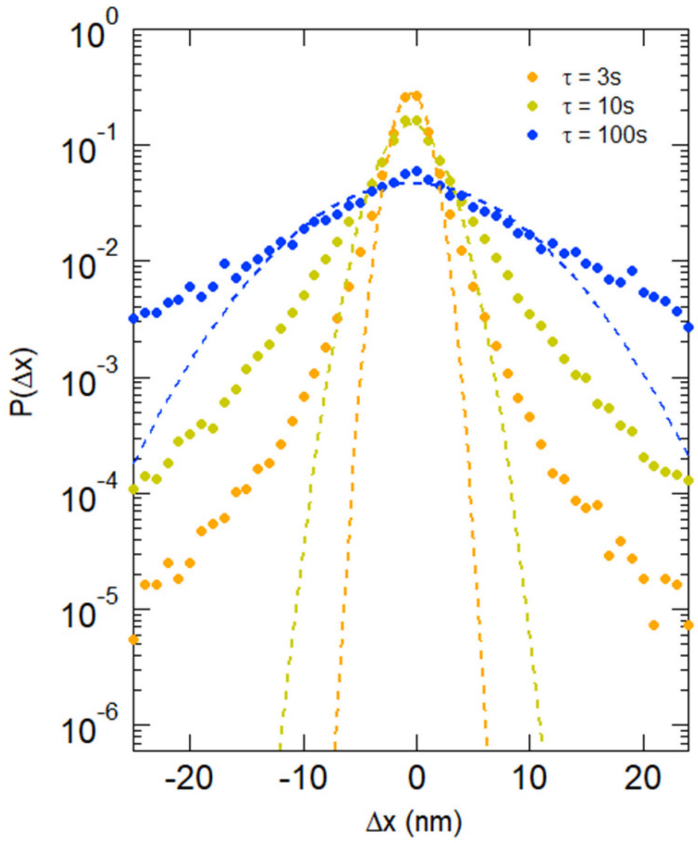

Figure 4.12 Unscaled displacement distribution (Van Hove) for 3T3 fibroblasts on k = 15.7 nN/μm substrates (N_{cell} = 14) at lag times τ = 3 s, 10 s and 100 s. Dashed lines show fits to Gaussian distributions at the lag time with the same color.

Since we found that the MSD magnitudes are power law distributed (**Figure 3.11** D and E), we scaled each individual post's displacements with a scaling factor $\xi(\tau) = e^{\langle \log(|\Delta x(\tau)|) \rangle}$, which is determined by the exponential of the log mean of the displacement of the post at a given lag time τ. For a Gaussian distribution, this scaling factor is proportional to the standard deviation of the distribution [123]. As illustrated in **Figure 4.13**, the scaling factor ξ increased with lag time following an approximate power-law. The scaling factor ξ was calculated separately at different lag times for each individual post, since the time dependence of ξ varies across different posts. We then

aggregated the scaled displacements $\Delta x_{scaled} = \Delta x / \xi$ from all cortical posts across multiple cells and plotted the resulting scaled Van Hove distributions. For a random walk with Gaussian distributed step sizes, the Van Hove will be a Gaussian distribution. **Figure 4.14** A shows the scaled Van Hove distribution at τ = 3 s, 10 s and 100 s for 3T3 fibroblasts on k = 15.7 nN/μm substrates on a semi-log scale. As illustrated, the experimental distributions possessed "fatter" tails in comparison to the Gaussian distribution (dashed line), indicating that the non-Gaussian behavior is intrinsic to the system's dynamics and is not an artifact of post-to-post heterogeneity. To better compare the displacement distributions across different lag times, it is helpful to plot them on a log – log scale, as shown in **Figure 4.14** B. From this it is apparent that the distributions show power law tails and appear to collapse onto a single curve. This scaled distribution can be parametrized by a Lévy distribution with tail exponent $\mu = 2.68 \pm 0.05$. (See Section 2.5 for the method used to determine the tail exponent). To better illustrate each individual curve at different lag times, we show the scaled Van Hoves at different lag times and the average Lévy distribution shifted vertically by a multiplicative factor of 0.5 consecutively (**Figure 4.14** B inset). To rule out whether such collapse is an artificial result due to over-parameterization, we also approximated the scaling factors at different lag times with fitted value from a power-law (lines in **Figure 4.13**) and found little variation in the resulting Van Hoves from **Figure 4.14** B. The data for 3T3 fibroblasts on other substrate stiffnesses and for other cell types are shown in **Figure 4.15** and **Figure 4.16**. Notably, even though the fluctuational force magnitude varied significantly as illustrated in **Figure 4.10**, we found all of these data are all non-Gaussian, and are well-parametrized by Lévy distributions with exponents in a narrow range near $\mu = 2.7$.

Since the Van Hoves are independent of lag time after scaling, we defined a master curve by the distribution of the aggregated scaled displacement across different lag times. We compared this master curve across multiple substrate stiffnesses for 3T3 cells (**Figure 4.17** A) and across multiple cell types (**Figure 4.17** B). These master curves are well-parametrized by Lévy distributions with exponents $\mu = 2.70 \pm 0.06$ for 3T3 fibroblasts across different substrate stiffnesses and $\mu = 2.75 \pm 0.04$ for different cell types. Such phenomena suggest that our previous finding of non-Gaussian fluctuations inside the actomyosin network (See Chapter 3) is likely to be an intrinsic property of the cellular actin cortex, and that the cortical fluctuations are governed by a Lévy process.

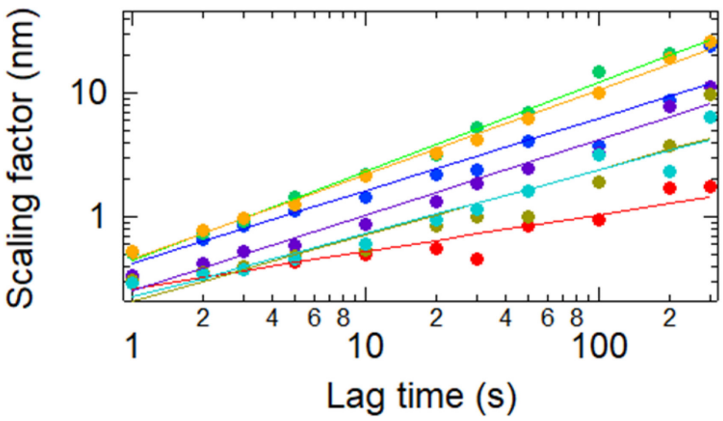

Figure 4.13 Time dependence of scaling factor $\xi(\tau) = e^{\langle \log(|\Delta x(\tau)|) \rangle}$ for a 3T3 fibroblast on a k = 15.7 nN/µm substrate. Lines are power-law fits to the data points. 7 sample cortical posts are shown.

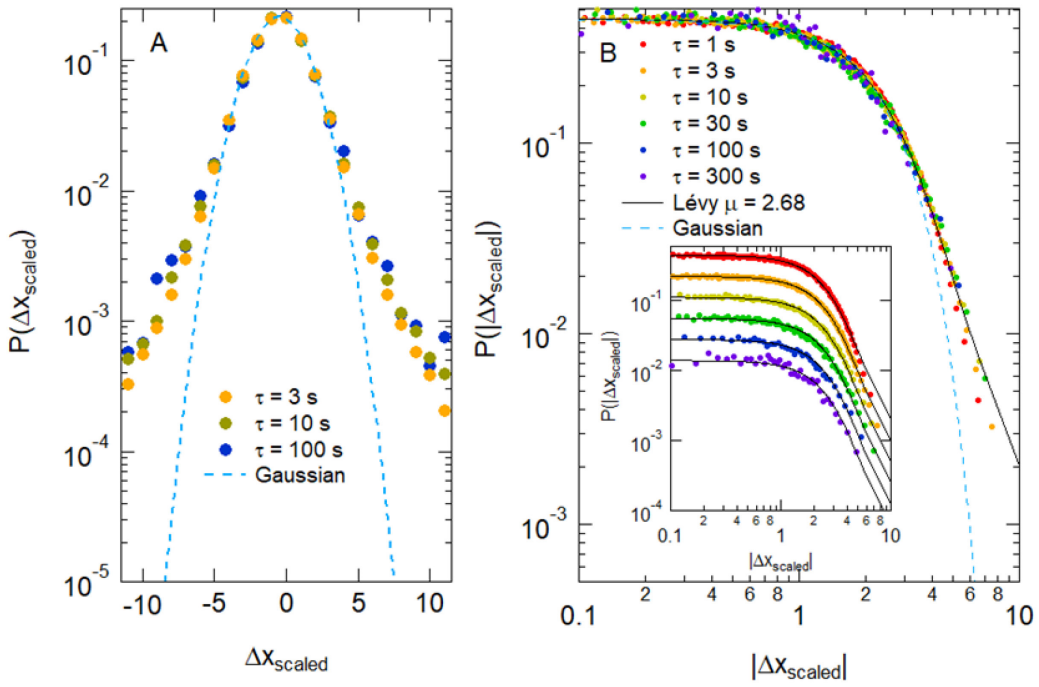

Figure 4.14 (A) Scaled displacement distributions across 14 3T3 fibroblasts on k = 15.7 nN/μm substrate for lag times τ = 3 s, 10 s and 100 s on a semi-log scale. Dashed line is a Gaussian distribution fit to the τ = 3 s displacement distribution. (B) Scaled displacement distribution on a log-log scale over lag times from τ = 1 s to τ = 300 s. The black line is a Lévy distribution fit to the aggregated data, parameterized with a tail exponent μ = 2.68 ± 0.05 (the tail exponent and its uncertainty were determined by the method described in Section 2.5). Inset shows the same distribution after shifting each curve along the y axis. The corresponding lines are the Lévy distribution in the main panel after shifting. The Gaussian curve from panel A is shown again for reference.

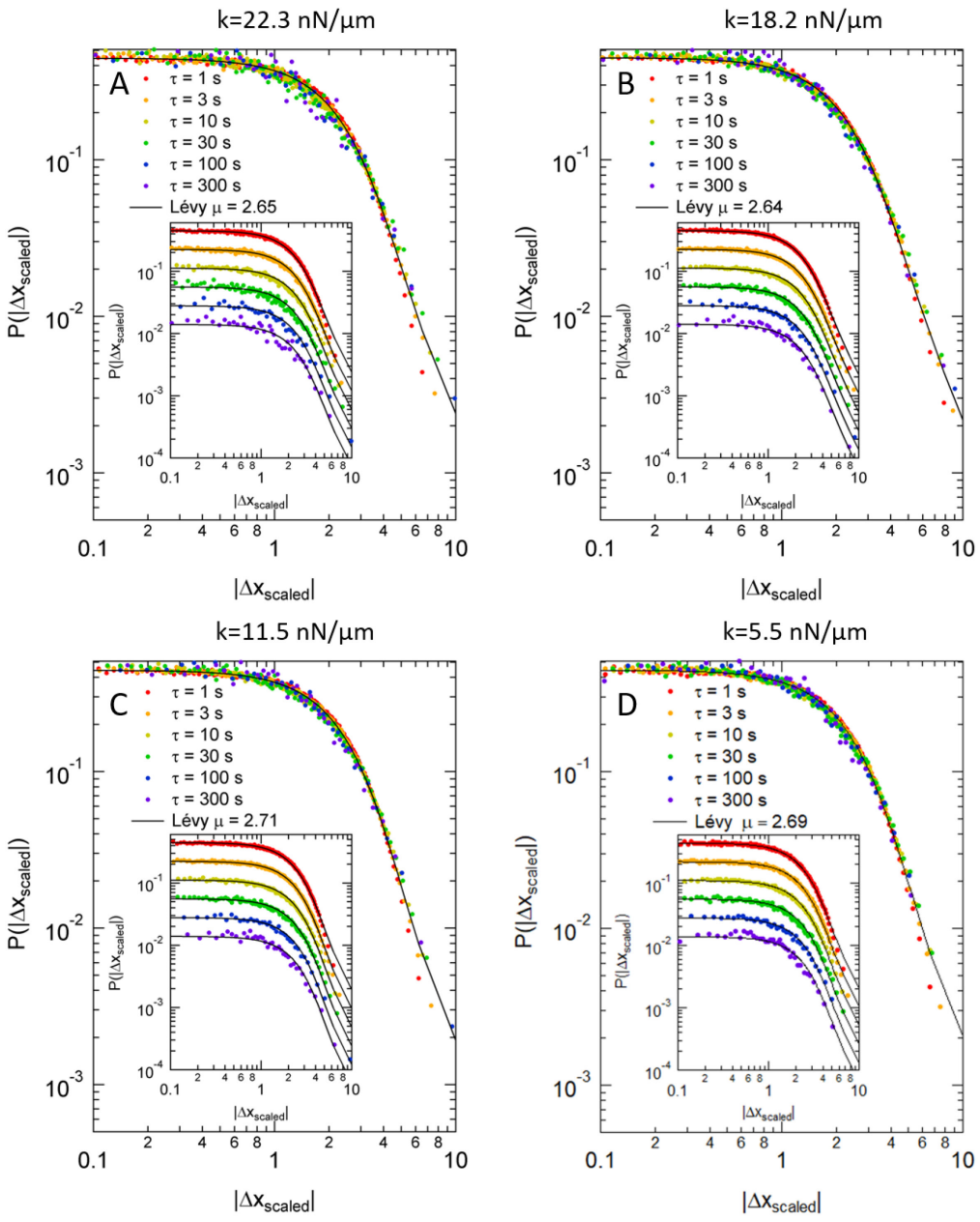

Figure 4.15 Scaled displacement distribution corresponding to **Figure 4.14** (C) for 3T3 fibroblasts on different stiffness substrates. The black curves show the Lévy distribution fit to the aggregated data, parameterized with a tail exponent μ (A) k = 22.3 nN/μm, μ = 2.65 ± 0.06 (B) k = 18.2 nN/μm, μ = 2.64 ± 0.04 (C) k = 11.5 nN/μm, μ = 2.71 ± 0.05 (D) k = 5.5 nN/μm, μ = 2.69 ± 0.04.

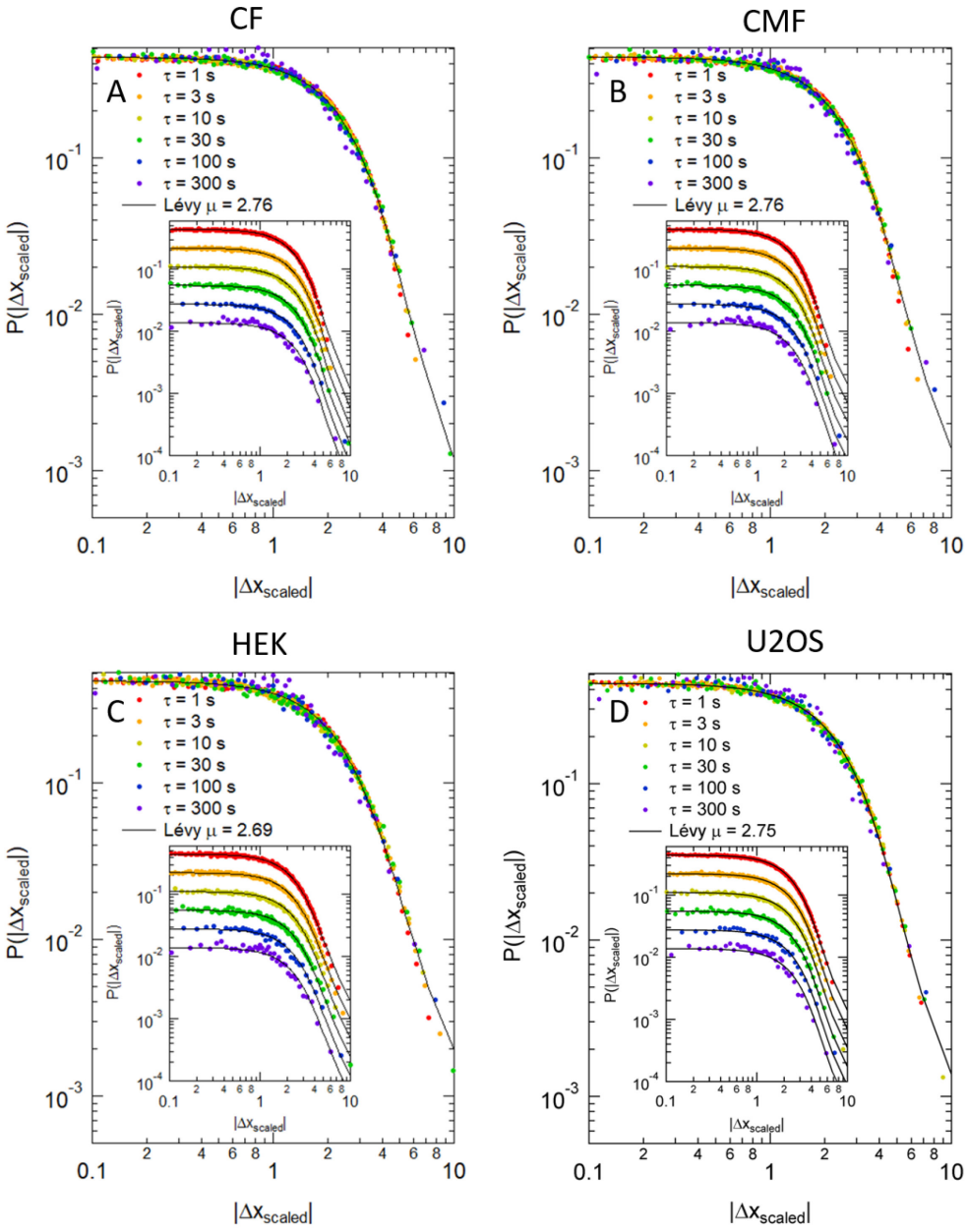

Figure 4.16 Scaled displacement distribution corresponding to **Figure 4.12** (C) for other cell types. The black curves show the Lévy distribution fit to the aggregated data, parameterized with a tail exponent μ (A) Cardiac fibroblasts, $\mu = 2.76 \pm 0.04$. (B) Cardiac myofibroblasts, $\mu = 2.76 \pm 0.05$. (C) HEK, $\mu = 2.69 \pm 0.05$. (D) U2OS, $\mu = 2.75 \pm 0.03$.

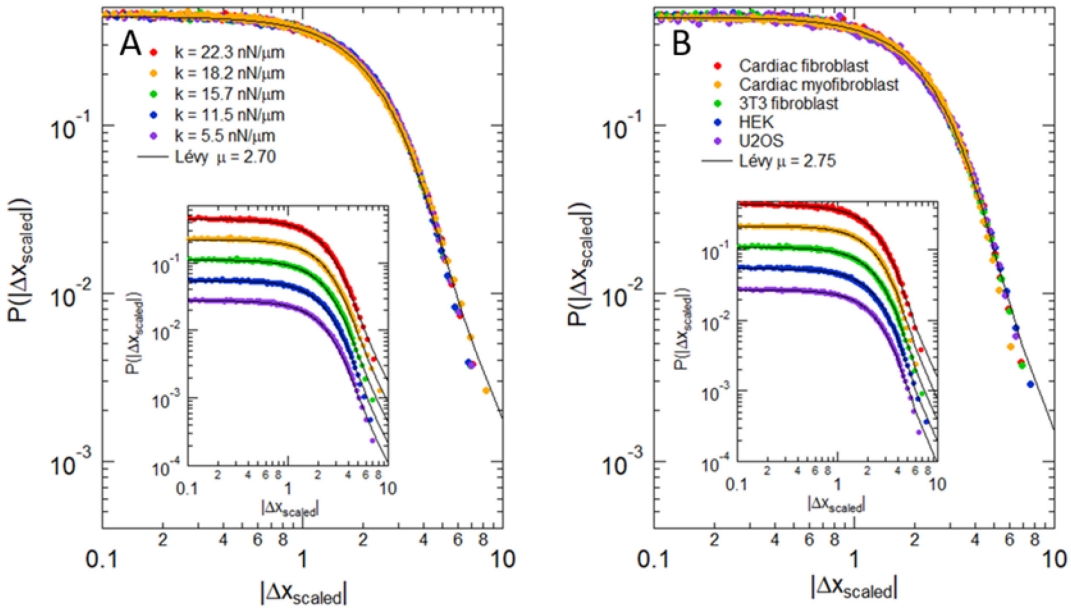

Figure 4.17 Scaled displacement distribution over multiple lag times for (A) 3T3 fibroblasts on different stiffness substrates and (B) different cell types. The tail exponent μ of the Lévy distribution was generated by fitting the aggregated data in each plot, with μ = 2.70 ± 0.06 in (A) and μ = 2.75 ± 0.04 in (B). Insets show individual traces offset by successive multiplicative factors of 0.5 for clarity.

4.5 Dimensionless measurements in actin cortex remain unchanged across cell type and stiffness

Given the non-Gaussian nature of fluctuations in the actin cortex, we next investigated its origin. Considering the heterogeneity within and between cells, we examined the anisotropy and the non-Gaussian parameter (Described in Section 3.8) of the fluctuations in the cellular actin cortex since they are both dimensionless and will be less affected by heterogeneity within and between cells. As described in Section 3.8, we calculated the eigenvalues of the moment of inertia tensor of the cortical-associated

microposts' trajectories over 90 s segments of the 1,800 s duration data sets, and present the trajectories' anisotropy using the ratio between the two eigenvalues λ_1/λ_2 ($\lambda_1 > \lambda_2$) that parametrize the trajectories (See **Figure 3.12** A and C for graphic demonstration). As shown in **Figure 4.18**, (and similar to **Figure 3.12** B), when compared with a simulated Gaussian random walk over the same time length, although the distribution of anisotropies for cortical posts remained similar to the random walk at lower anisotropy values, the subset with high anisotropy approximately followed a power-law tail with exponent around -3 and deviated significantly from the simulated random walk. The anisotropy distribution showed little variation across substrate stiffness (**Figure 4.18** A) and cell types (**Figure 4.18** B). Also, as shown in **Figure 3.12** D and E, the anisotropy direction is weakly correlated with the traction force direction (**Figure 4.19**), and the high anisotropy ($\lambda_1/\lambda_2 >$ 5) segments followed a Poisson distribution (**Figure 4.20**). As previously discussed in Chapter 3, the high anisotropy segments in the actin cortex are associated with large unidirectional motions, and these results indicate that the non-Gaussian fluctuations in actin cortex originate from intermittent processes that are randomly distributed both spatially and temporally. Here we see that such behavior is independent of cell type and substrate stiffness.

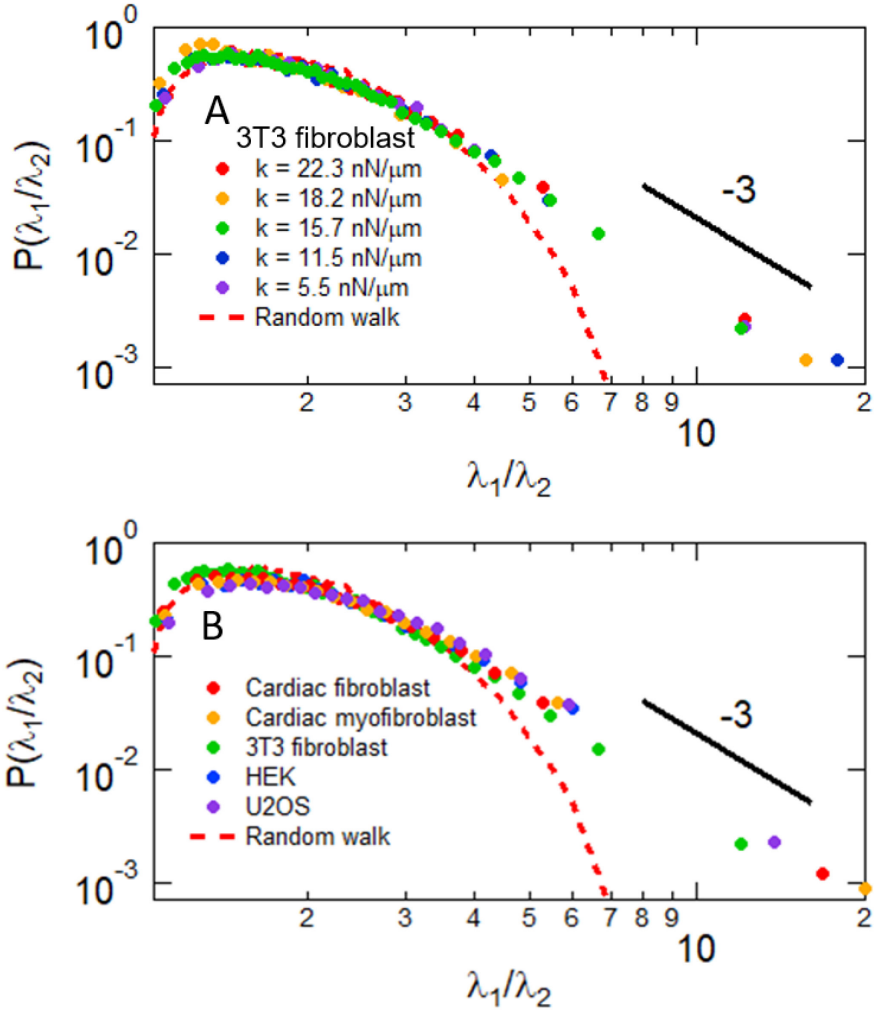

Figure 4.18 Anisotropy distribution (corresponding to **Figure 3.12** B) for (A) 3T3 fibroblasts on different substrate stiffness and (B) for different cell types.

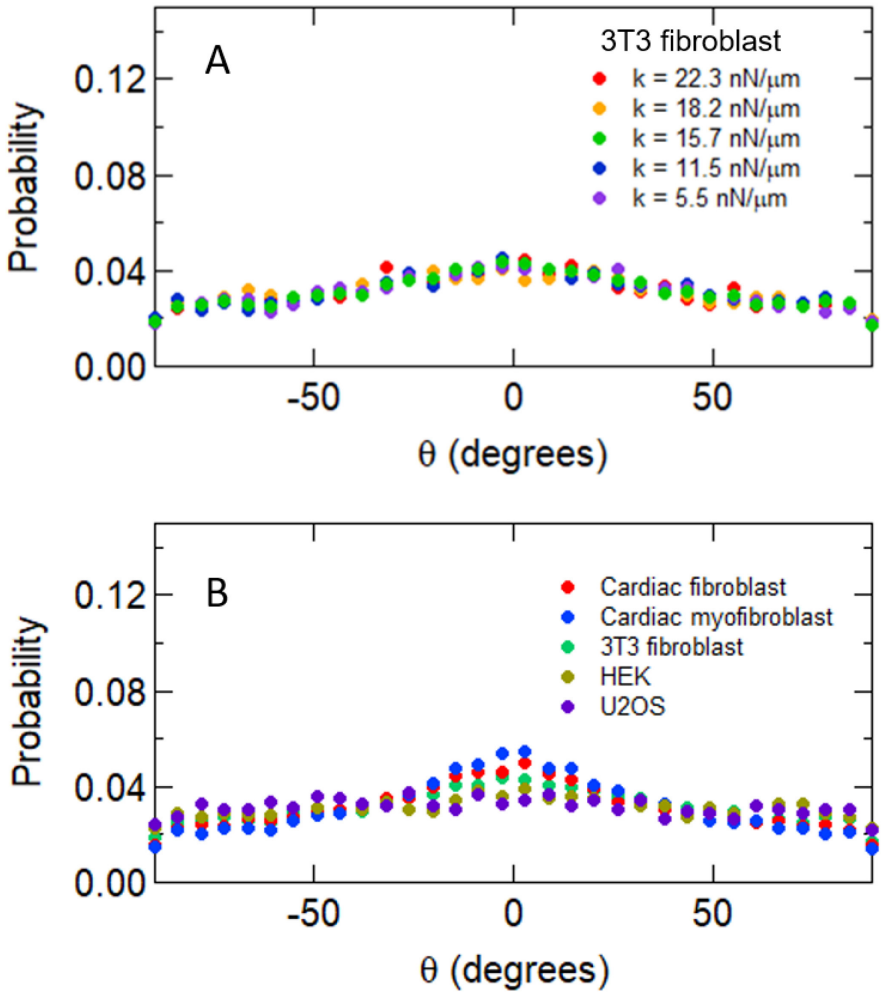

Figure 4.19 Distribution of the angle between traction force and λ_1 (corresponding to **Figure 3.12** C) for (A) 3T3 fibroblasts on different substrate stiffness and (B) for different cell types.

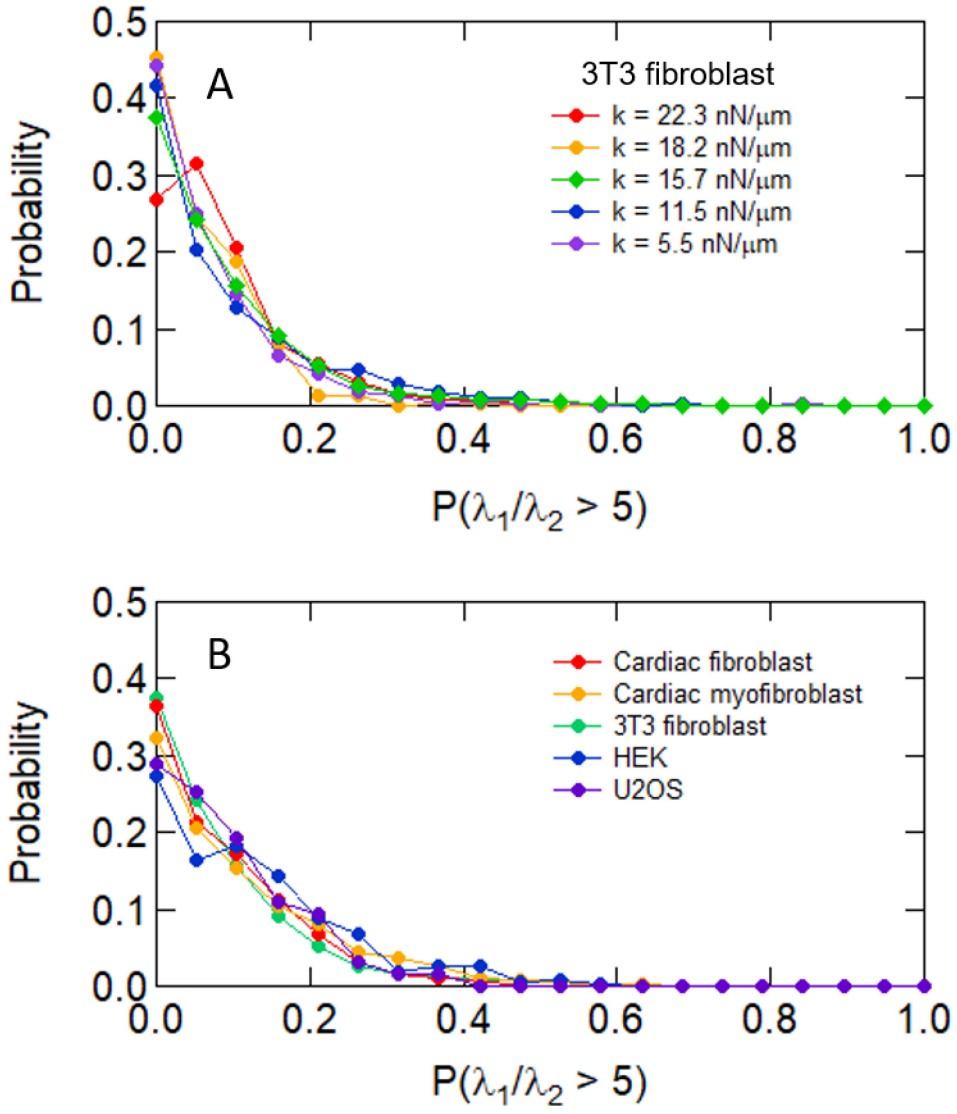

Figure 4.20 Distribution of high anisotropy portion (corresponding to **Figure 3.12** D) for (A) 3T3 fibroblasts on different substrate stiffness and (B) for different cell types.

To further illustrate this intermittent process within individual posts, we quantified the posts' fluctuations based on their trajectories over 1,800 s via the non-Gaussian parameter $\alpha_2 = \frac{\langle x^4 \rangle}{3\langle x^2 \rangle^2} - 1$, introduced in Section 3.8. Compared with the distribution calculated from a Gaussian random walk with trajectories of the same length, the

fluctuations in the actin cortex have a significantly larger portion of highly non-Gaussian motions (**Figure 4.21** A and B). We also found that the distribution of the non-Gaussian parameter revealed little variation across cell types and substrates stiffness. Therefore, although the magnitude of actin cortical fluctuations varies across individual cells, as well as between cells, its generic nature remains unchanged: large displacements appear randomly in time and space, and their magnitudes are power-law distributed, as shown in the anisotropy distribution in **Figure 3.12** A and C. These correspond to the non-Gaussian distributions in the Van Hoves and the observed intermittency in fluctuations.

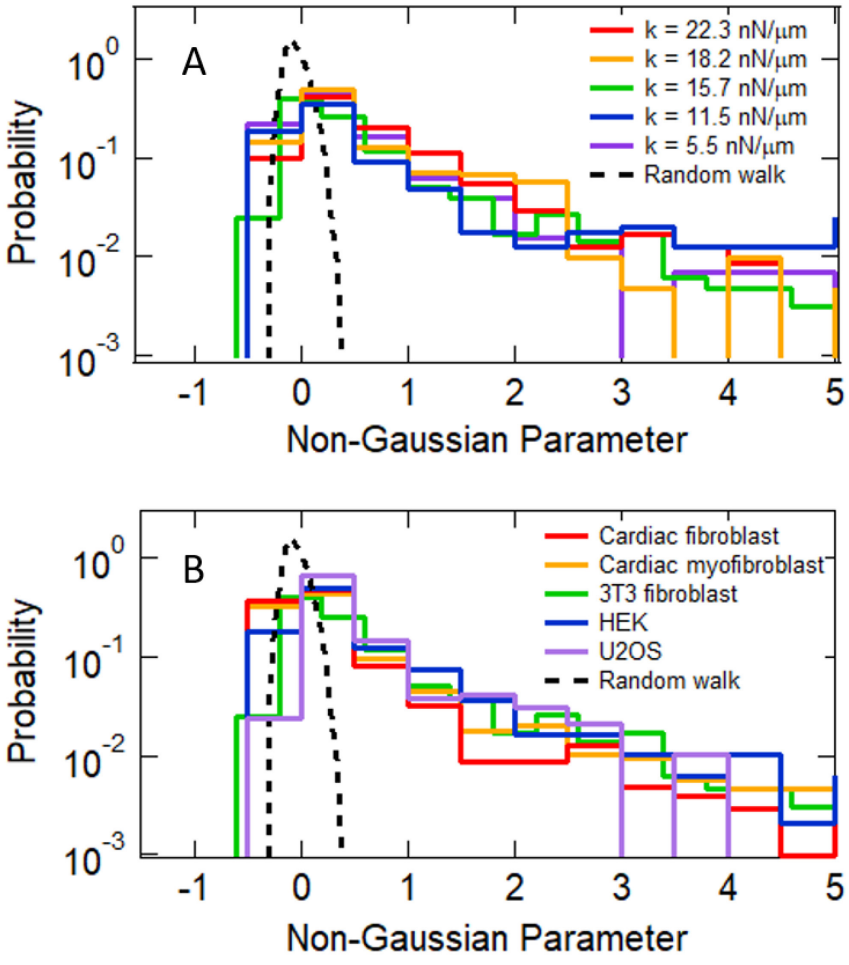

Figure 4.21 Distribution of non-Gaussian parameter (corresponding to **Figure 3.14** E) for (A) 3T3 fibroblast on different substrate stiffness and (B) for different cell types.

4.6 Actin cortex displays avalanche-like motion

As described in Section 3.9, the power law distribution we observed in the cortical fluctuations indicated the possibility of finding avalanches in our system. To illustrate this for the larger data set described in this chapter, we applied the data mining techniques described previously in Section 3.9 to reveal nearest neighbor microposts with correlated motions and synchronized step-like motions. We found such avalanche-type motions for 3T3 fibroblasts with all substrate stiffness we examined (**Figure 4.22**), and across all the cell types we studied (**Figure 4.23**).

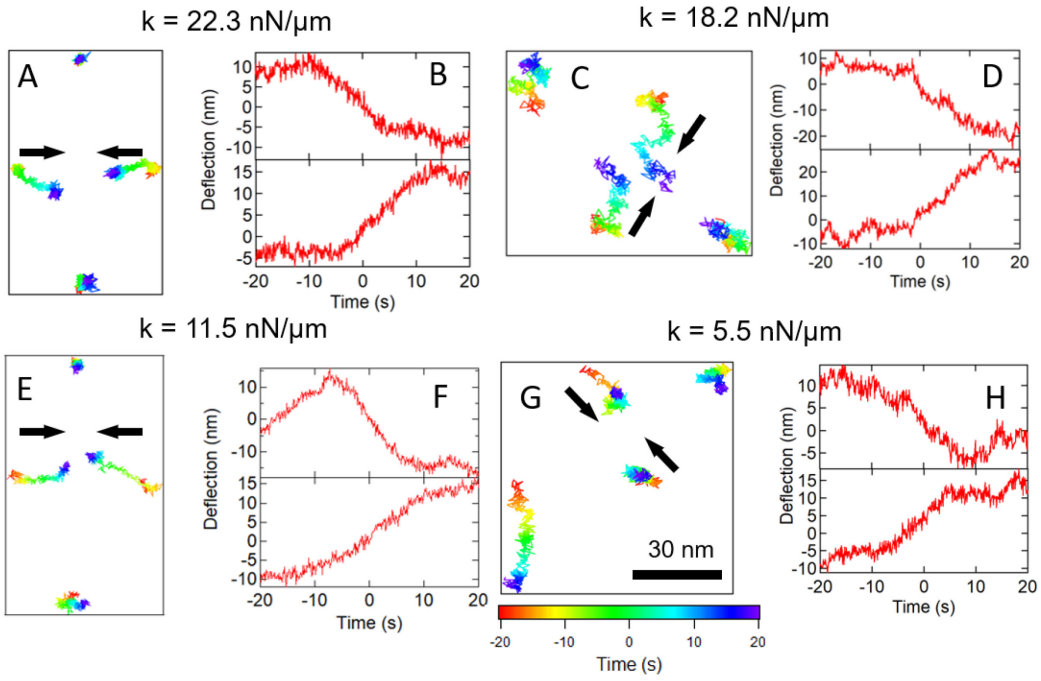

Figure 4.22 Sample avalanche events for 3T3 fibroblasts on different substrate stiffnesses. (A) 2D traces over 40 s for the nearest and the corresponding 2nd nearest neighbor posts on substrates with stiffness k = 22.3 nN/μm. (B) Deflection along the bond direction of the two nearest neighbor posts during avalanches. (C)-(D), (E)-(F) and (G)-(H) show sample avalanche events of 3T3 fibroblasts on substrates with stiffnesses k = 18.2 nN/μm, 11.5 nN/μm and 5.5 nN/μm, respectively.

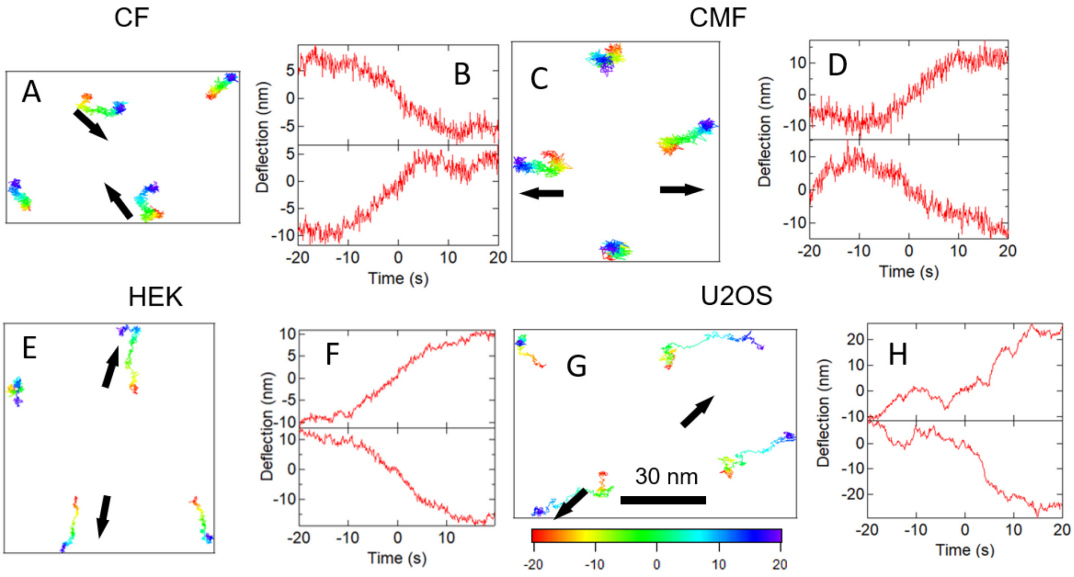

Figure 4.23 Sample avalanche events for different cell types. Description follows the same notation as **Figure 4.22** and **Figure 3.16** (A)-(D). (A)-(B) Cardiac fibroblast. (C)-(D) Cardiac myofibroblast. (E)-(F) HEK. (G)-(H) U2OS.

To parameterize these step-like motions, we used an error function to fit the curves and extract their heights and durations. (See detailed description in Section 3.9.) To verify whether the nature of these step-like events was due to complex spatial-temporal evolution as discussed in Section 3.9, we then calculated the averaged motion along the bond direction, as well as the step durations of the two posts within the same pair. As shown in **Figure 4.24** and **Figure 4.25**, we found these motions appear to be rather gradual processes, with durations on the scale of 10 s. Moreover, similar to our observation in **Figure 3.16** F, we found weak correlations in step durations between the two posts within the same pair. These observations suggest these processes display complex spatial-temporal evolution, and are consistent with the notion of avalanches rather than viscoelastic response to a single step stress.

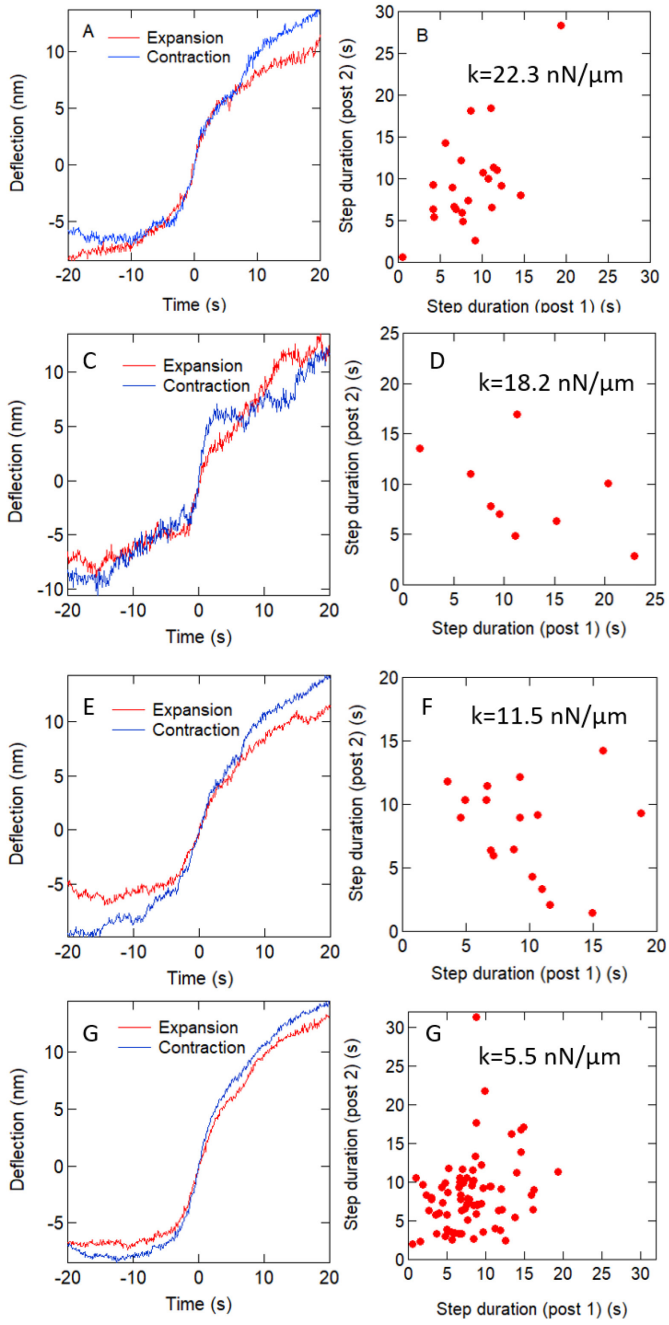

Figure 4.24 (A) averaged step profiles of post motions along the vector connecting the two posts within the same pair for 3T3 fibroblasts on k = 22.3 nN/µm substrates during avalanches. Expansion (red) and contraction (blue) events were averaged separately. (B) Scatter plot of step durations for pairs of posts, pooling the contracting and expanding pairs. Corresponding plots are shown for other substrate stiffnesses: (C) – (D) k = 18.2 nN/µm, (E)–(F) k = 11.5 nN/µm, (G)-(H) k = 5.5 nN/µm.

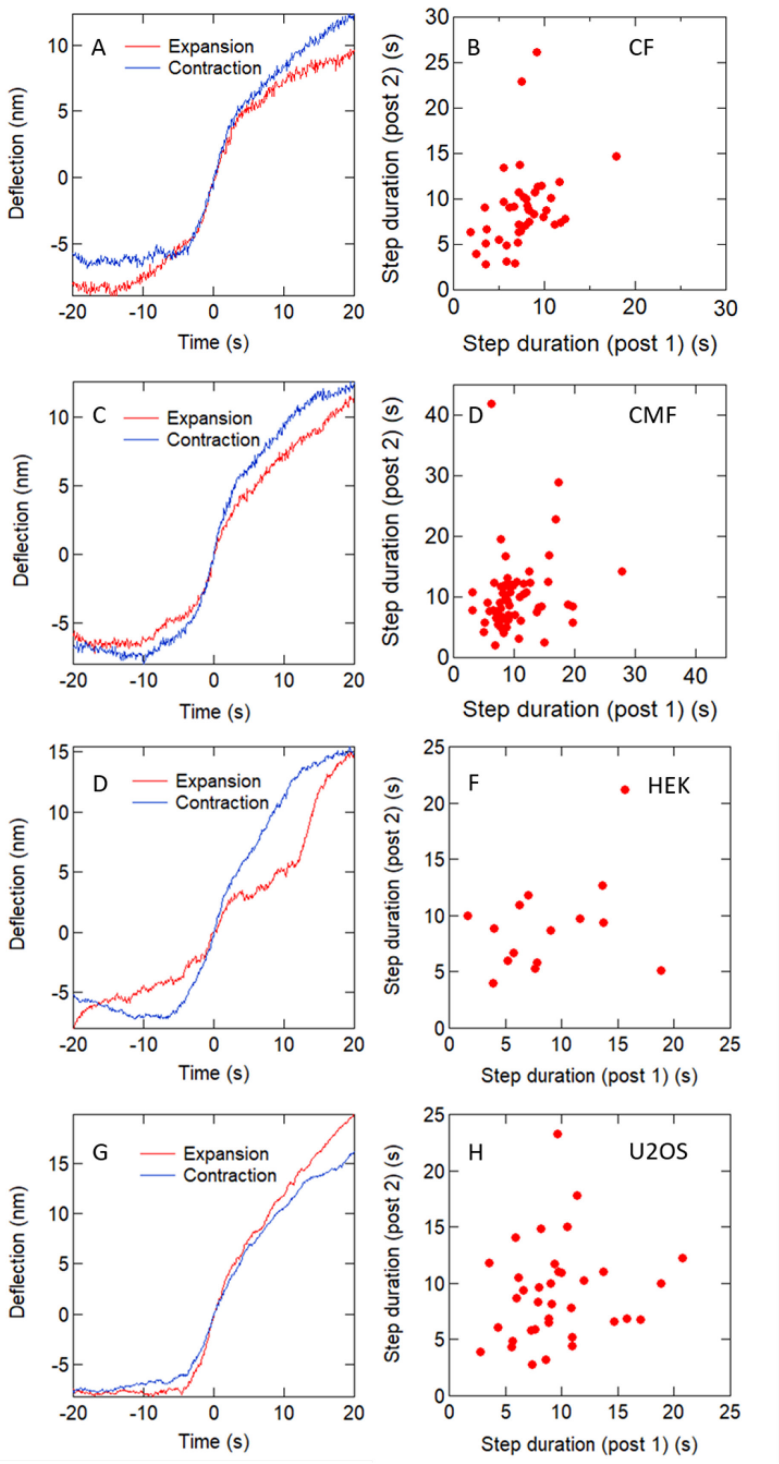

Figure 4.25 (A) averaged step profile of post motions along the vector connecting the two posts within the same pair for cardiac fibroblast (CF) during avalanches. Expansion (red) and contraction (blue) were averaged separately. (B) Scatter plot of step durations for pairs of posts, pooling the contracting and expanding pairs. (C) – (D) cardiac myofibroblast (CMF), (E)–(F) HEK, (G)-(H) U2OS.

We then compared the dependence of step heights and durations between substrate stiffnesses and cell types, extracted by fitting the posts' motion to an error function as described in Section 3.9. **Figure 4.26** A and B shows step height and durations for 3T3 fibroblasts for substrate stiffnesses from 5.5 nN/μm to 22.3 nN/μm. Since the distributions of step heights and step durations appear to be non-Gaussian, comparing their mean and standard error using a T-test will be hindered by the outliers. Therefore, to compare whether they follow the same distribution, we applied a Kolmogorov–Smirnov test (K-S test) [124]. We found no significant differences between the steps' heights and durations as the substrate stiffness varies. We also applied the same analysis of step height and step durations to the different cell types, as illustrated in **Figure 4.26** C and D and compared with 3T3 fibroblasts at the corresponding stiffness. Again, we found that the step durations showed no significant differences when compared to 3T3 fibroblasts, and between cardiac fibroblasts and their myofibroblast phenotype. However, for step heights, we found that non-fibroblast cells (HEK and U2OS) showed larger step heights compared with 3T3s ($p<0.05$ between HEK and 3T3 fibroblasts on $k = 15.7$ nN/μm, $N_{HEK} = 30$ and $N_{3T3} = 126$; $p<0.01$ between U2OS and 3T3 fibroblasts on $k = 5.5$ nN/μm, $N_{HEK} = 72$ and $N_{3T3} = 148$), and that cardiac myofibroblasts had larger steps compared with cardiac fibroblasts ($p<0.05$, $N_{CF} = 82$ and $N_{CF} = 122$).

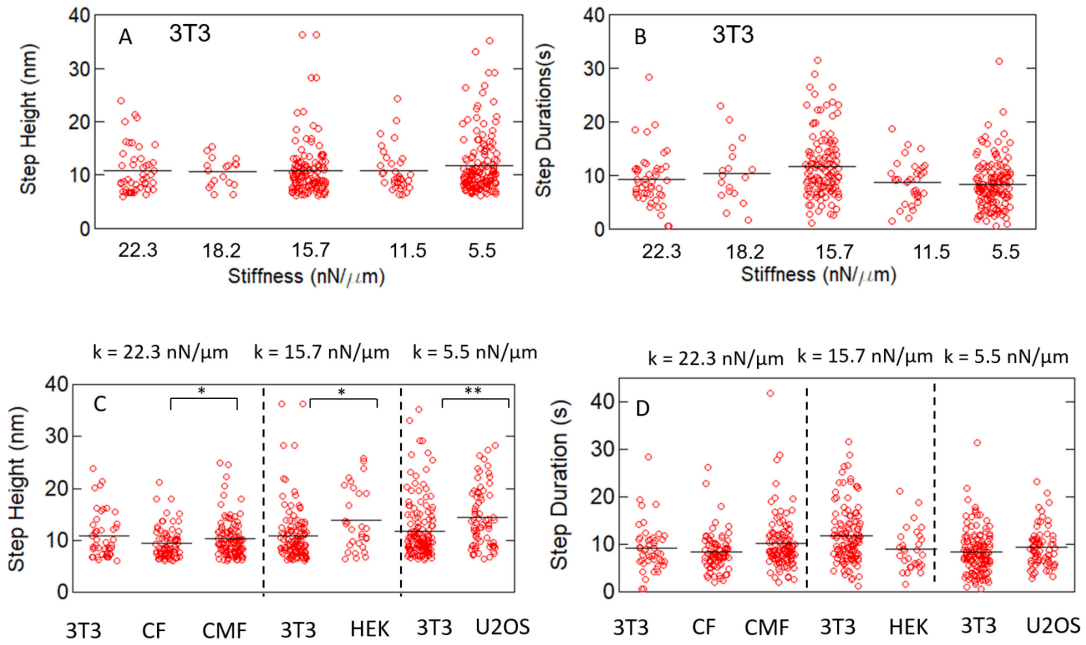

Figure 4.26 Scatter plot for (A) step height and (B) step durations of avalanche events found in 3T3 fibroblasts on different substrate stiffnesses. (C) and (D) show the corresponding data for different cell types, where CF = cardiac fibroblast and CMF = cardiac myofibroblast. Each cell type is compared with 3T3 fibroblasts on the corresponding substrate stiffness. (*: $p<0.05$, **: $p<0.01$)

4.7 Discussion

In this chapter, we explored the dynamics in the cellular actin cortex on substrates with different stiffnesses and across multiple cell types (fibroblast cells and non-fibroblast cells). Our findings suggest that fluctuational forces increase with substrate stiffness and varied across cell types. We also observed that fluctuational force increased as cardiac fibroblasts transformed into myofibroblasts.

However, despite of the variations in fluctuational magnitude, we found little variation in the underlying physics. Our results revealed similar Van Hove displacement distributions, anisotropy, and non-Gaussian parameter distributions across different cell

types and substrate stiffnesses. We also found the same type of cortical avalanches as described in Section 3.9 in all cell types and substrate stiffnesses we studied. These results indicate that non-Gaussian statistics and high intermittency are intrinsic characteristics of the dynamics of the cellular actin cortex.

Our studies of the displacement distributions (Van Hove plots) also revealed that fluctuations in actin cortex followed a Lévy distribution which showed little variation across lag times, substrate stiffnesses, and cell type. This suggests that the cortical fluctuations may be driven by a Lévy process. We also found that the Van Hove curves at $\tau < 3$ s appear to show faster decays compared with other lag times, which can be possibly attributed to the fact that the largest avalanches, which likely play a major role in determining the non-Gaussian character of the cortical fluctuations, have durations typically longer than 10 s (See Section 3.9 and Section 4.6) and so the displacement distributions at shorter lag times may be less sensitive to these processes.

To summarize, we have seen non-Gaussian fluctuations and intermittency in the dynamics of the actin cortex, as well as a large dispersion in MSD exponent both within and between cells for both different substrate stiffnesses and different cell types. These results suggest that cellular actin cortex is generically marginally stable, which lead to the observed fluctuations to resemble Lévy processes.

Chapter 5 Probing detailed structures of cortical avalanches with nanoposts

5.1 Introduction

As presented in Chapter 3 and 4, microposts with 1.8 μm diameter and 4 μm spacing revealed strong evidence of cortical avalanches. Here in this chapter, we seek to explore detailed structure of "avalanche" events. To perform such analysis, we applied nanopost arrays with a factor of four higher post density. Masters for these arrays were provided to us by Dr. Jianping Fu's group at the University of Michigan. In this chapter, I will describe the experimental approach for measuring cellular fluctuations with nanoposts which achieves a comparable spatial and temporal resolution as in Chapter 3. I will also present preliminary data for avalanches that spread across four nanoposts.

5.2 Imaging and analysis of actin cortical fluctuations

Nanopost arrays were fabricated and functionalized with fibronectin using the same protocol as for the micropost arrays (See Section 2.2 and 2.3). The nanoposts were 800 nm in diameter and had 2 μm center-to-center spacing, forming a hexagonal lattice. The nanoposts were 4.77 μm in height with a spring spring constant k = 1.39 nm/μm (**Table 2.2**).

3T3 fibroblasts on the nanoposts were imaged with a 40X objective with a 1.5X magnifier under bright field on a Nikon TE2000E microscope. Cells were recorded at 100 frames per second (fps) and then averaged over 10 frames to decrease background noise to 1 nm (measured by root mean square of the background nanopost fluctuations). As the cells were more motile on the nanoposts than on the microposts, they were imaged for 5 min rather than 30 min so that cells remained in a single field of view. **Figure 5.1** shows a sample trace of a nanopost under a 3T3 fibroblast and a background post not in contact with the cell. We then characterized the posts' mean square displacements and again found that most cell-associated posts showed super-diffusive fluctuations with posts near the cell periphery showing larger fluctuations (**Figure 5.2**).

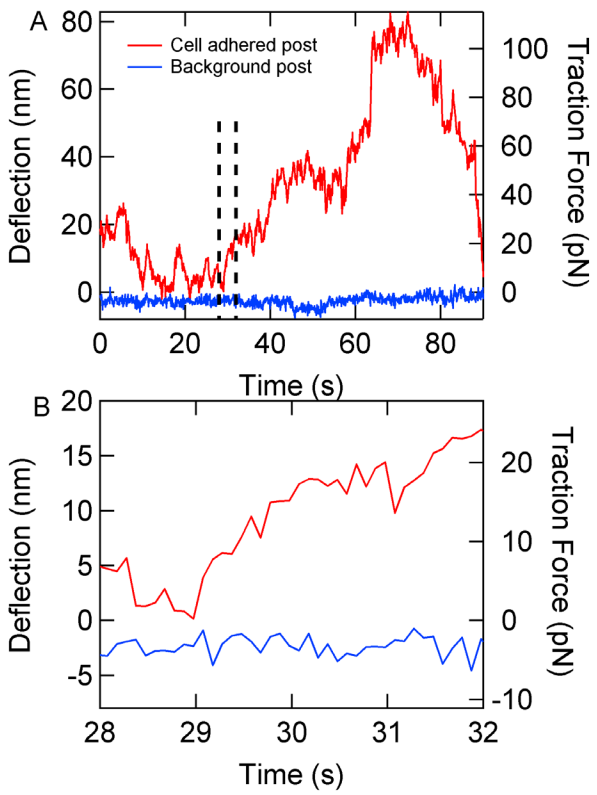

Figure 5.1 (A) Deflection of a 3T3 fibroblast-associated nanopost and a background post over 90 s. Traction force was converted using the spring constant. (B) Zoomed-in view of the region indicated by the black dashed lines in (A).

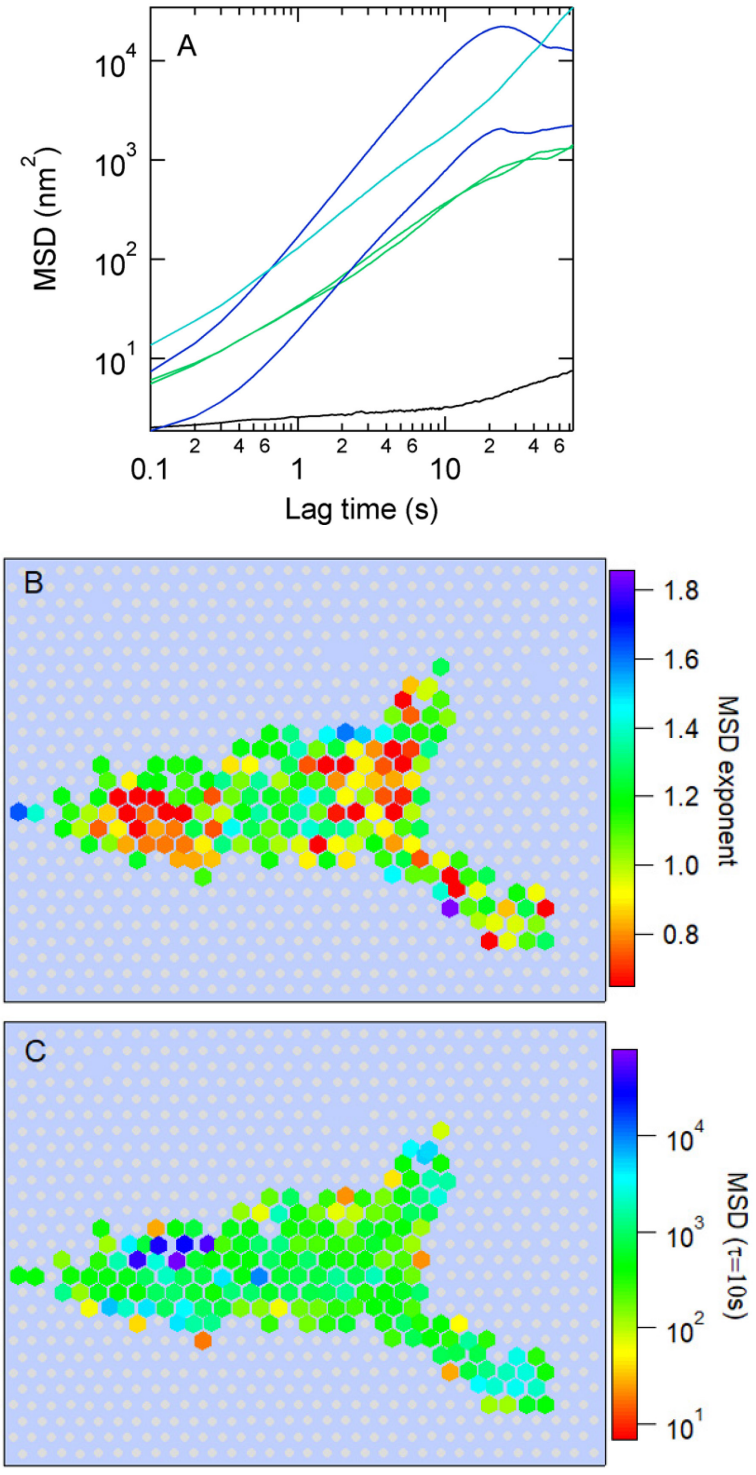

Figure 5.2 (A) Mean square displacement of nanoposts. Colors indicate the MSD exponents. Black curve is from the background post in **Figure 5.1**. (B) Distribution of MSD exponents. (C) Distribution of MSD magnitudes at $\tau = 10$ s.

5.3 Nanoposts reveals detailed symmetry of cortical avalanches

The smaller post to post distance of the nanopost arrays provide us higher spatial resolution to study the detailed symmetry of cortical avalanches found in Section 3.9 and Section 4.6. We started by looking for four-post units formed by two near neighbor posts and their corresponding second near neighbor posts. A coincidental detection technique, similar to the one described in Section 3.9, was then applied to these four-post units. We looked for anti-correlated step-like motions with velocity larger than 3 nm/s and occurred within 5 s among the near neighbor post pair and the second near neighbor post pair. Only units with simultaneous step-like motions in all four posts were identified as avalanches. We found 15 such units with avalanche out of 7587 four-post units in a preliminary dataset of 10 3T3 fibroblasts and did not found any when the four posts were randomly selected. **Figure 5.3** shows sample avalanches we found with different symmetries. As described in **Figure 3.17**, **Figure 5.3** A implies stress on an incompressible sheet (N = 6) and B and C imply uniaxial compression (N = 5) and expansion (N = 4) respectively. However, we did not find any avalanches with rotational motion. These preliminary results show the potential of nanopost arrays in revealing cortical avalanches discussed in Chapter 3 and 4 with greater detail. Therefore, follow-up studies should be able to apply these analyses to a larger dataset to study the detailed symmetry and spatial extension of these cortical avalanches with greater statistics.

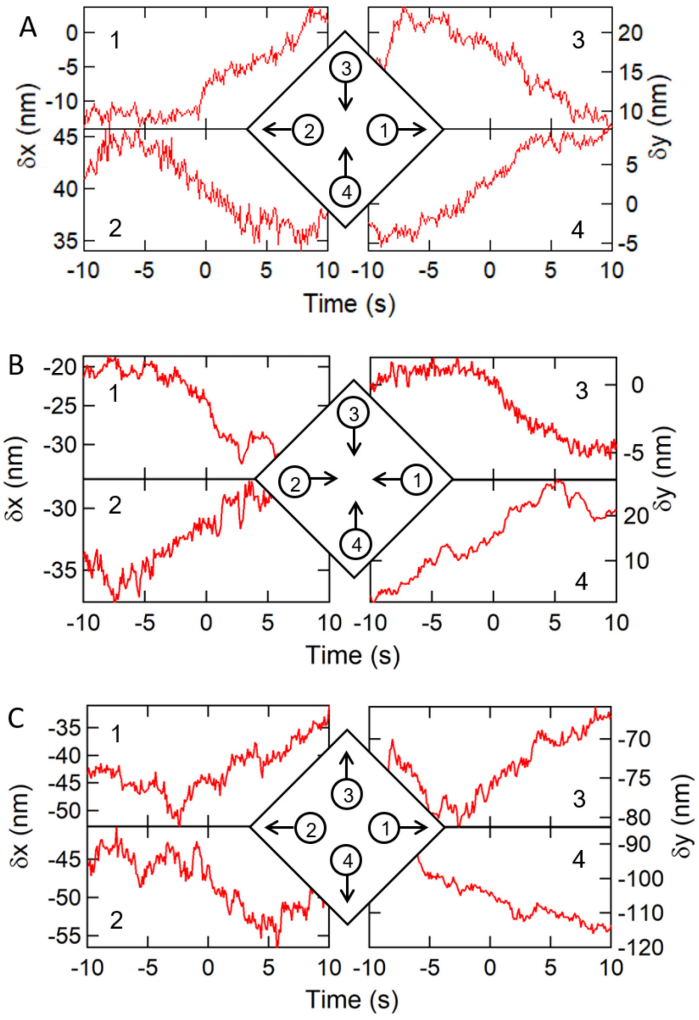

Figure 5.3 Avalanches within four posts revealed by nanopost arrays. Deflections are along the direction of the bonds over 20 s. The center diamond shows the relative position of the four posts. (A) contraction in one pair and expansion in another pair. (B) contraction in both pairs. (C) expansion in both pairs.

5.4 Discussion

In this chapter, I presented preliminary studies with nanopost arrays as an approach to reveal cortical avalanches with greater details. I showed that our imaging methodology can resolve actomyosin fluctuations with nanoposts at nanometer scale resolution,

comparable to what we have achieved with microposts in Chapter 3 and 4. I also used a small preliminary dataset to demonstrate the potential of using the nanopost arrays to reveal detailed symmetry of cortical avalanches.

In the future, one can apply this approach to study cortical avalanches with a larger dataset, to understand the avalanches' detailed symmetry and characteristic spatial extent.

Chapter 6 Cellular interactions between cardiac fibroblasts and myocytes

6.1 Introduction

This chapter describes experiments done with MPADs to measure mechanical outputs of neonatal rat ventricular cardiac fibroblasts (CF), cardiac myofibroblasts (CMF) and cardiomyocytes (CMs). After cardiac injury, CFs are activated to migrate to the wound site and differentiate into CMFs. However, the poor electrical connection between CMFs and CMs can significantly increase the risk of arrhythmia. The goal of these studies is to understand the mechanoelectrical coupling between CF/CMF and CMs and illustrate the role of fibroblast contractility in this process. While completed as part of a larger project in collaboration with Geran Kostecki from the Leslie Tung lab of the Johns Hopkins University Department of Biomedical Engineering and Shoshana Das from the Christopher Chen lab of the Boston University Department of Biomedical Engineering, taken alone, the measurements provide a characterization of the mechanical properties of neonatal rat ventricular CFs, CMFs and CMs.

In this chapter, I present studies of changes in mechanical properties in the CF to CMF transformation, which served as a support study for the project described above, and also present results on measuring the time dependent traction force of CMs and interactions between CMFs using micropost arrays.

6.2 Traction force increase with CF to CMF transformation

We seeded CMFs (TGF-β treated) and CFs (SD-208 treated) on microposts over night before measuring. 75 MFs and 61 CFs were measured for their total substrate strain energy calculated as $E = \sum \frac{1}{2} k \Delta r^2$ where Δr is the displacement of a micropost from its undeflected position, and the sum is over all microposts underneath the cell. As described in Section 2.2.3, there is a 4% variation in the micropost spring constant, which is ignored when we calculate the total strain energy. We found that CMFs were significantly more spread on the substrates, with average number of posts under cell N_{posts} = 196±89 for CMFs and N_{posts} = 88±53 for CFs (**Figure 6.1**). Also, the CMFs had a greater strain energy per post, with 1.11±0.67 fj/post for CMFs and 0.46±0.43 fJ/post for CFs (**Figure 6.2**). This indicates that mechanical properties undergo significant changes during the CF to CMF transformation, in that CMFs are more contractile as suggested by the previous result [120]. Moreover, compared with the results in [120], our results provided a better separation between CFs and CMFs since we treated CFs with SD-208 to prevent spontaneous CMFs transformation, therefore improving the purity of the CFs group.

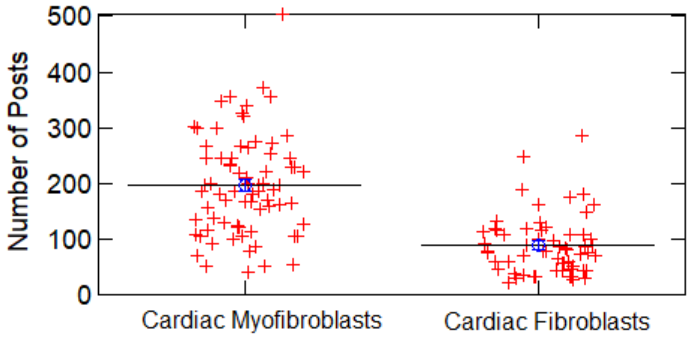

Figure 6.1 Number of posts underneath a single cell. Each data point represent data from one cell.

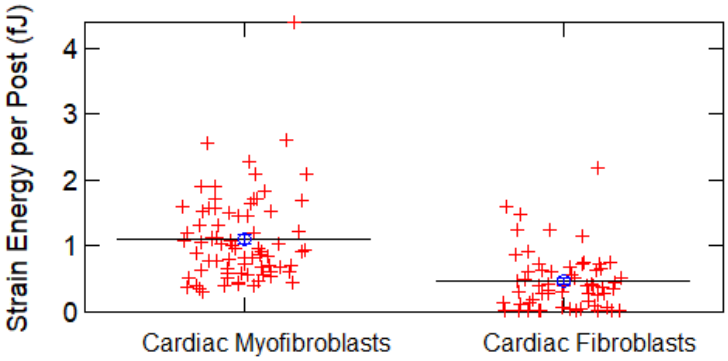

Figure 6.2 Averaged strain energy per posts. Each data point represent data from one cell.

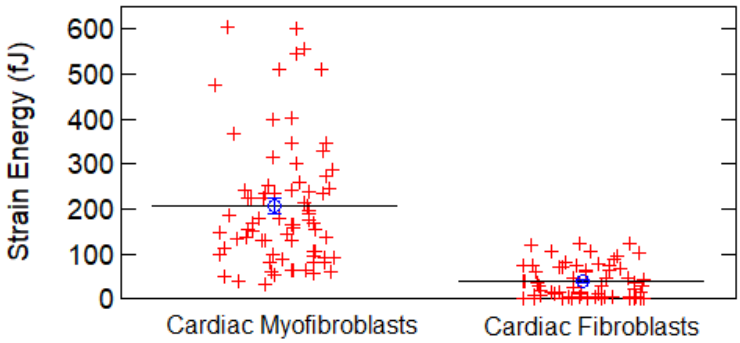

Figure 6.3 Total strain energy in each cell. Each data point represents data from one cell.

6.3 Measurements of traction force of cardiomyocytes

As part of the studies of mechanics in cardiac cells, we are also interested in quantifying the changes in traction force of cardiomyocytes during their contraction pulses. Since cardiomyocytes are less viable when seeded as single cells on microposts rather than in groups, we coated microposts with 200 μm square patterns of fibronectin to enable cells

forming clusters on microposts. In **Figure 6.4**, we fluorescently tagged fibronectin and imaged the patterned fibronectin distribution when stamped on top of the micropost arrays. As shown in **Figure 6.5** cellular traction force increased significantly when myocytes undergo contraction pulses, and pulses of cells in the same cluster were highly synchronized. To better quantify this, cells were measured by their total strain energy over 10 s. To control cardiomyocytes' beating frequency, we paced cells with an S48 stimulator (Astro Med. Inc.) by applying pulsed electric fields. **Figure 6.6** shows that the beating frequency of the cells correlated with the pacing frequency.

To verify the dependence of cellular contraction on calcium level, we also paced cells at various calcium concentrations. Cells were cultured in Tyrodes solution with glucose (5mM) and $CaCl_2$ (0.54,1.8 and 5.4 mM and paced at a constant 2 Hz frequency. We calculated the peak height of each pulse in total strain energy, and observed that it strongly correlated with calcium level (**Figure 6.7**), as expected from the previous results [125].

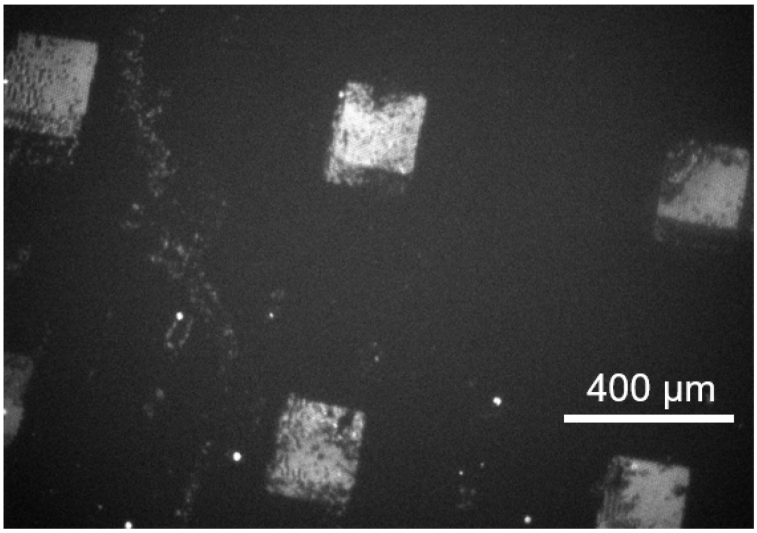

Figure 6.4 Micropost substrates coated with fibronectin in a pattern of 200 µm squares and 800 µm center to center distance between the two adhesive squares.

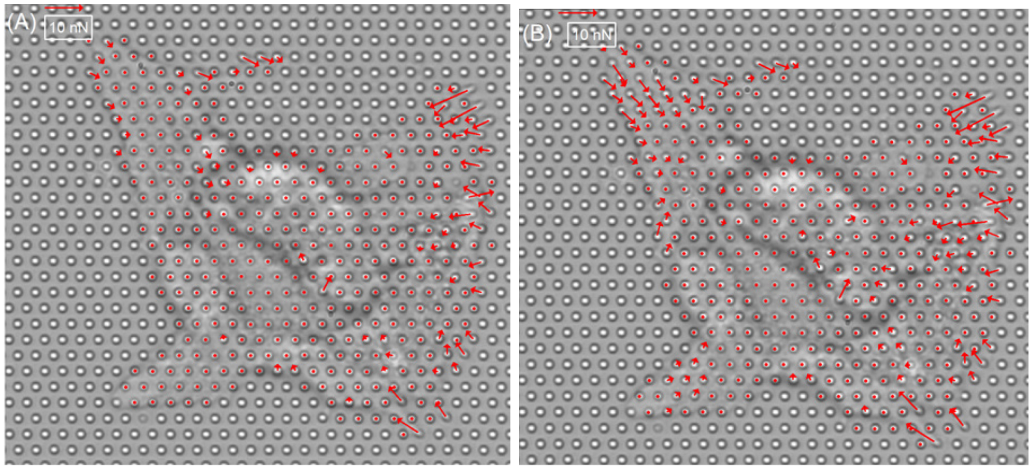

Figure 6.5 Traction force distribution of cardiomyocytes at (A) relaxed state and (B) contractile state.

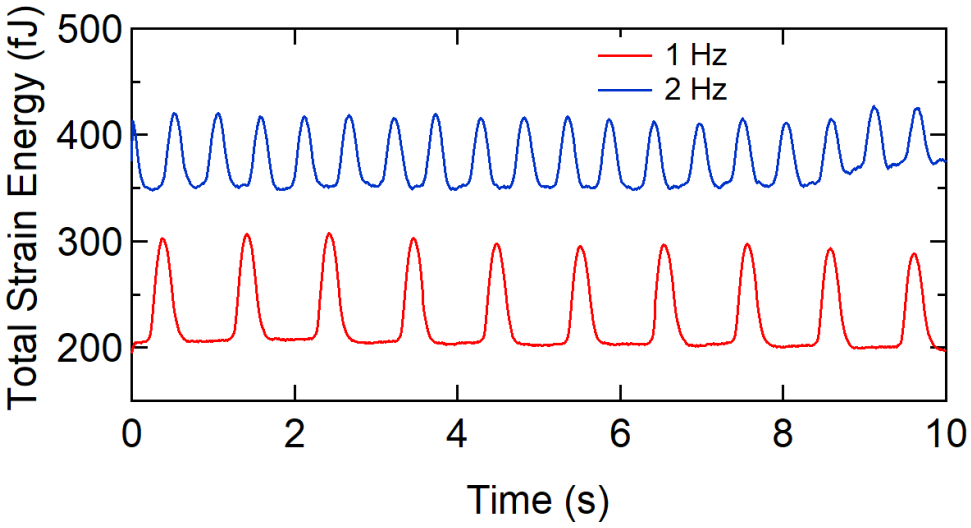

Figure 6.6 Cardiomyocytes' strain energy increase with driving pulse, with frequency corresponding to the driving frequency.

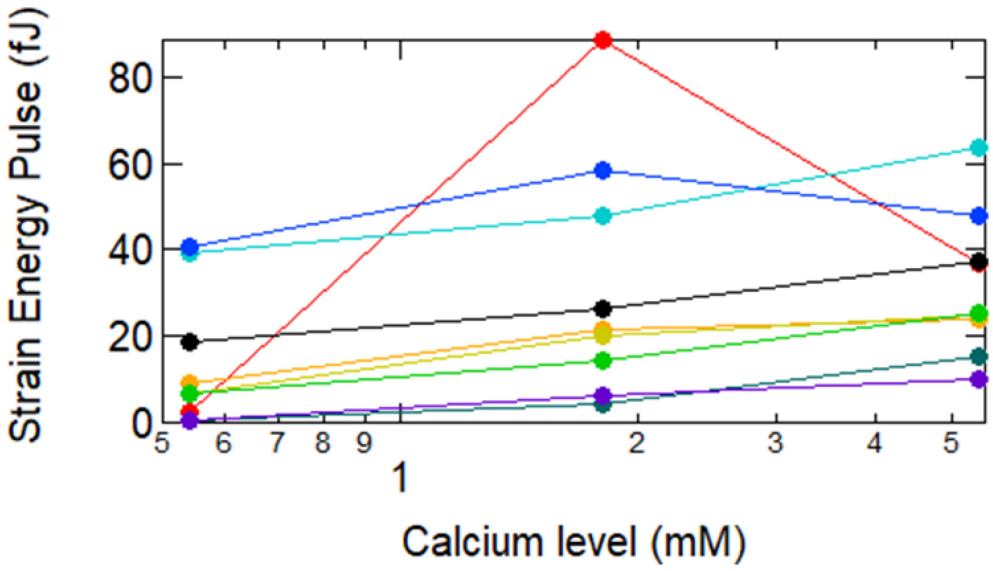

Figure 6.7 Dependence of pulse magnitude upon calcium level, where 1.8 mM is the standard level of culturing media. Each line shows an individual cell's strain energy pulse change over different calcium levels.

6.4 Measurements of fibroblast interactions

To measure cell-cell interactions of cardiac myofibroblasts, we seeded cells onto microposts at 5-times higher concentration than the one described in Section 2.6 (5×10^4 cells per dish). Cell solutions were rocked slightly before seeding to enhance cluster formation. Cells were then seeded onto microposts coated with fibronectin, and groups of 2-3 cells were imaged. We then measured average traction force per post in each cell of the cell pair/cluster over 30 minutes. As shown in **Figure 6.8**, a cluster of three cells showed a synchronized contraction pulse at t = 700 s, followed by a gradual relaxation. **Figure 6.9** shows the distance between two neighboring posts with distance color coated. At approximately t = 700 s, we observed a simultaneous decrease in intracellular post distance

in all three cells (more red dots in each cell's interior), indicating increases in the contractility of all three cells. Moreover, we also observed that the distances between neighboring posts across the cell boundaries increased (more purple dots across cell boundaries), suggesting intercellular boundaries being stretched. This cell-cell mechanical coupling for cardiac fibroblasts is also confirmed by staining cellular N-cadherin junctions. As shown in **Figure 6.10**, higher intensities of N-cadherin were found at boundaries between cells, which indicates the existence of cell-cell mechanical coupling between cardiac myofibroblasts [126]. These measurements therefore provide a direct evidence for the intercellular mechanical couplings between neighboring cardiac myofibroblasts.

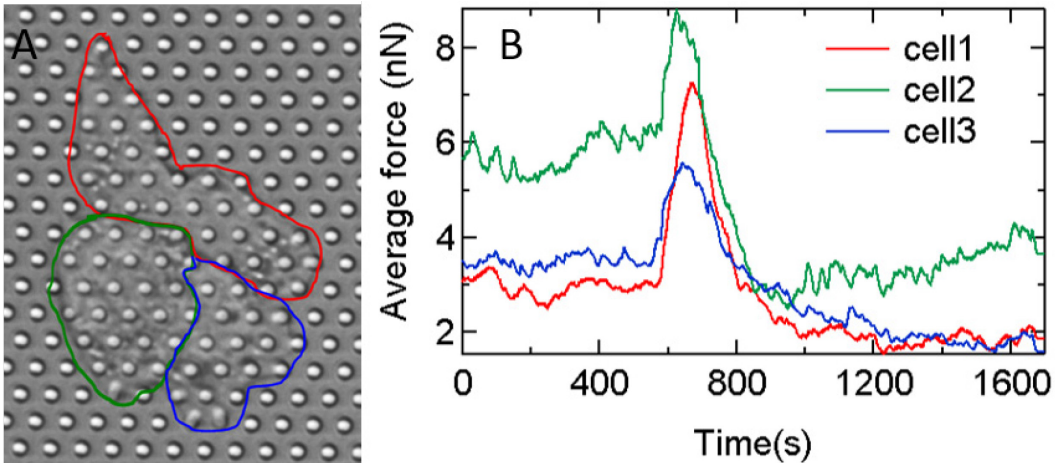

Figure 6.8 Cardiac myofibroblasts show synchronized contraction pulses. (A) a group of three cardiac myofibroblasts on microposts. (B) Average traction force of each cell, showing a simultaneous pulse over the course of 1,700 s. Color of each trace corresponds to the outline color of each cell in (A).

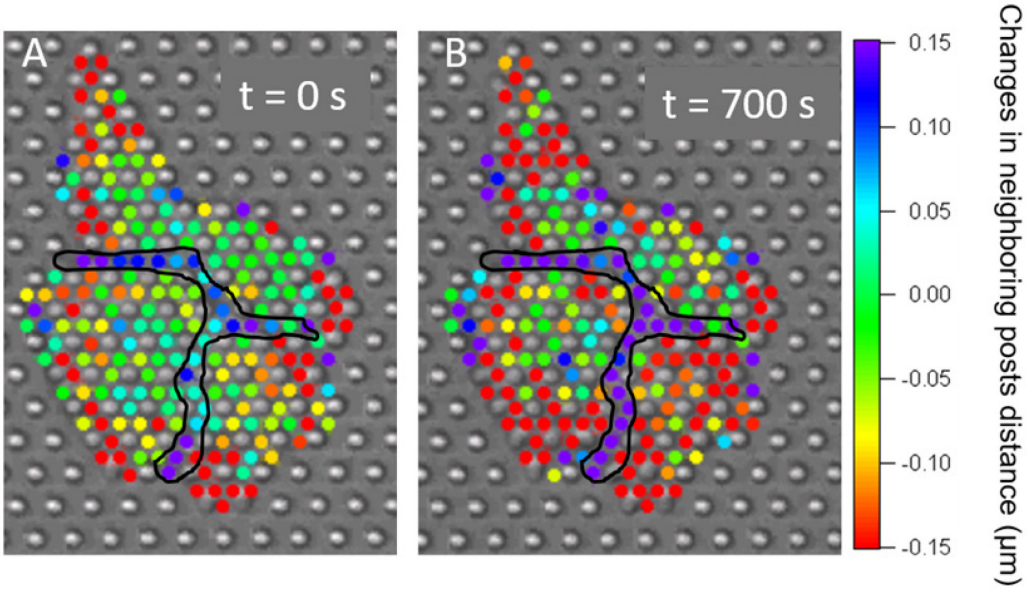

Figure 6.9 Color heatmap of neighboring posts distance relative to resting positions for the three cells shown in **Figure 6.7** A. Black outlines indicate the gaps between neighboring cells. (A) cells are in relaxed state. (B) cells are in contractile state.

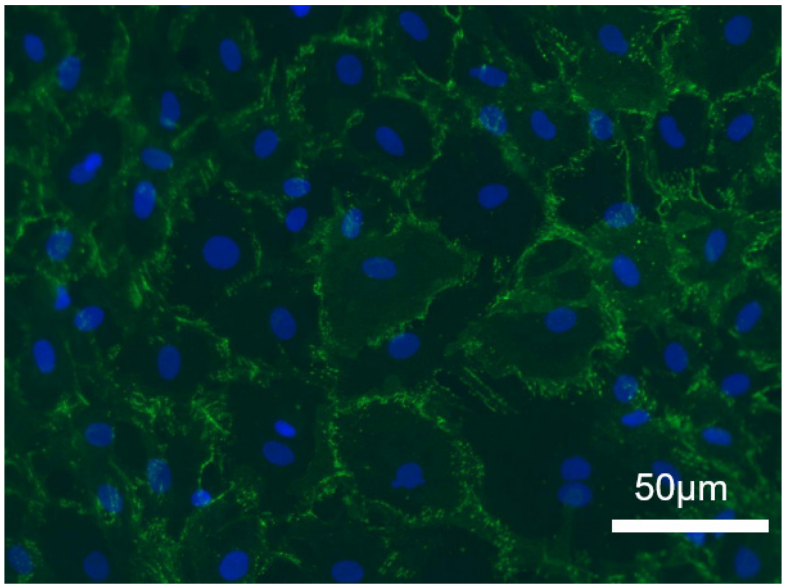

Figure 6.10 Distribution of N-cadherin of cardiac myofibroblasts. Nuclei were tagged blue and N-cadherin were tagged green, which is highly concentrated at cell-cell junctions.

6.5 Discussion

In this chapter, we applied micropost arrays to study the mechanical properties of neonatal rat cardiac fibroblasts, cardiac myofibroblasts and cardiomyocytes. We confirmed that the transformation from cardiac fibroblasts to cardiac myofibroblasts will increase cellular spreading area as well as traction force. We also successfully cultured and paced cardiomyocyte groups on micropost arrays, quantified their traction force changes during contraction pulses, and confirmed the dependence of the variation in contractility during these pulses on Calcium concentration. At the end, we observed cell – cell mechanical coupling between cardiac myofibroblast pairs cultured on micropost arrays.

Chapter 7 Summary and Future Directions

The cytoskeleton is a remarkable example of an active biomaterial and is at the heart of critically important problems in biology and medicine related to animal cells' mechanical sensing and function. To connect molecular machinery within cytoskeleton with cellular scale functions requires the ability to perform active and passive microrheology at high spatial and temporal resolution.

I applied micropost array detectors embedded with magnetic nanowires, also denoted as active micropost array detectors (AMPADs), to probe actomyosin dynamics. To measure the local cellular rheology, I actuated magnetic nanowires embedded in posts with an AC magnetic field and found that the actomyosin cytoskeleton is dominantly elastic with rheology following a power law frequency dependence. I also measured actomyosin fluctuations through tracking microposts' motion, characterized them using mean square displacements (MSD), and found microposts underneath the cell can be bifurcated into actin cortex associated posts and stress fiber associated posts. Close analysis revealed super diffusive fluctuations in both groups with highly dispersed magnitude, following a highly non-Gaussian "fat-tailed" distribution. By assessing dimensionless quantities such as the anisotropy and non-Gaussian parameter, I found that fluctuations in the actin cortex followed a highly intermittent process, with rare large step-like motions, which resembled reconfiguration processes in avalanches. Large avalanche events in the actin cortex were

then isolated through searching for highly spatial-temporal correlated motions in neighboring microposts. These results indicate the similarity between actin cortex and soft glassy materials and imply the cellular actin cortex is in a marginally stable state.

The passive microrheology measurements were also performed on 3T3 fibroblasts on different stiffness as well as multiple cell types. I found that traction force and fluctuational magnitude vary across cell types. However, when studying the displacement distribution after scaled by fluctuational magnitude, the distribution follows a Lévy distribution, and shows very little dependence on cell types and substrate stiffness. Similarly, when studying other dimensionless metrics such as anisotropy and non-Gaussian parameters, the fat-tailed distribution remains unchanged by cell types or substrate stiffness. These results indicate that the non-Gaussian statistics and resemblance to avalanches systems appear to be intrinsic characteristics of the actin cortex.

However, much still remains to be studied in actomyosin network dynamics. The AMPADs failed to reveal detailed structures of avalanches as they were only found within the nearest neighbor post pairs. Although I have done some preliminary work using nanometer-scale posts arrays and successfully isolated avalanches spreading over four nanopillars, they still need to be analyzed systematically. Moreover, the onset mechanism of these avalanches in the actin cortex remains unclear and requires chemical perturbation to deepen our understanding.

Finally, as part of a larger project probing mechanoelectrical coupling between neonatal rat ventricular cardiacfibroblast/myofibroblast and cardiomyocytes, I characterized the dynamical properties of these cell types. I found cardiac myofibroblasts are significantly more contractile and have large fluctuations compared with cardiac

fibroblasts and studied the intercellular mechanical coupling between cardiac fibroblast cells. I also incubated and paced cardiomyocytes on micropillar arrays and measured their traction force change during beating.

In summary, the AMPADs provide a new approach for dissecting actomyosin dynamics with high spatial and temporal resolution, and the capability of performing passive and active microrheology. With the help of this system, I found that cellular actin cortex dynamics resemble that of avalanches, suggesting that the cortex is in a marginally stable state. From a functional perspective, the marginal stability of the actin cortex enables cells to remodel their cytoskeleton when necessary while maintaining homeostasis under small perturbations. I believe the AMPADs are a tool with great potential to investigate this further. One question that remains to be answered is the mechanism for the microscopic onset of these avalanches. The magnetic nanowires inside the microposts allow local mechanical stimulation which should enable one to examine whether cortical avalanches can arise from the controlled mechanical perturbations. It will also be fruitful to apply chemical perturbations to the cellular cytoskeleton to understand the role of different cytoskeletal components for the onsets of the cortical avalanches. Answering these questions will greatly improve our understanding of the cellular cytoskeleton from a physics perspective, which will be beneficial for cell and tissue engineering in that it will shed light on modeling cellular cytoskeleton.

Bibliography

1. Chen, C.S., *Mechanotransduction - a field pulling together?* J Cell Sci, 2008. **121**(Pt 20): p. 3285-92.
2. McBeath, R., et al., *Cell shape, cytoskeletal tension, and RhoA regulate stem cell lineage commitment.* Developmental Cell, 2004. **6**(4): p. 483-495.
3. Huang, S., C.S. Chen, and D.E. Ingber, *Control of cyclin D1, p27(Kip1), and cell cycle progression in human capillary endothelial cells by cell shape and cytoskeletal tension.* Molecular Biology of the Cell, 1998. **9**(11): p. 3179-3193.
4. Sordella, R., et al., *Modulation of Rho GTPase signaling regulates a switch between adipogenesis and myogenesis (vol 113, pg 147, 2003).* Cell, 2003. **113**(4): p. 547-547.
5. Marchetti, M.C., et al., *Hydrodynamics of soft active matter.* Reviews of Modern Physics, 2013. **85**(3): p. 1143-1187.
6. Ramaswamy, S., *The Mechanics and Statistics of Active Matter.* Annual Review of Condensed Matter Physics, Vol 1, 2010. **1**: p. 323-345.
7. Prost, J., F. Julicher, and J.F. Joanny, *Active gel physics.* Nature Physics, 2015. **11**(2): p. 111-117.
8. Fabry, B., et al., *Scaling the microrheology of living cells.* Physical Review Letters, 2001. **87**(14): p. 148102.
9. Bursac, P., et al., *Cytoskeletal remodelling and slow dynamics in the living cell.* Nature Materials, 2005. **4**(7): p. 557-561.
10. Trepat, X., et al., *Universal physical responses to stretch in the living cell.* Nature, 2007. **447**(7144): p. 592-595.
11. Schweitzer, F., *Brownian Agents and Active Particles. Collective Dynamics in the Natural and Social Sciences*. 2003, Berlin: Springer.
12. Ramaswamy, S., *The Mechanics and Statistics of Active Matter.* Annual Review of Condensed Matter Physics, 2010. **1**(1): p. 323-345.
13. Dombrowski, C., et al., *Self-concentration and large-scale coherence in bacterial dynamics.* Physical Review Letters, 2004. **93**(9): p. 098103.
14. Kemkemer, R., et al., *Elastic properties of nematoid arrangements formed by amoeboid cells.* European Physical Journal E, 2000. **1**(2-3): p. 215-225.
15. Caussin, J.B., et al., *Emergent Spatial Structures in Flocking Models: A Dynamical System Insight.* Physical Review Letters, 2014. **112**(14): p. 148102.
16. Nishiguchi, D., et al., *Long-range nematic order and anomalous fluctuations in suspensions of swimming filamentous bacteria.* Physical Review E, 2017. **95**(2): p. 020601.
17. Klamser, J.U., S.C. Kapfer, and W. Krauth, *Thermodynamic phases in two-dimensional active matter.* Nature Communications, 2018. **9**: p. 5045.
18. Prymidis, V., H. Sielcken, and L. Filion, *Self-assembly of active attractive spheres.* Soft Matter, 2015. **11**(21): p. 4158-4166.

19. Chen, D.T.N., et al., *Rheology of Soft Materials.* Annual Review of Condensed Matter Physics, Vol 1, 2010. **1**: p. 301-322.
20. Chugh, P. and E.K. Paluch, *The actin cortex at a glance.* Journal of Cell Science, 2018. **131**(14): p. 186254.
21. Tojkander, S., G. Gateva, and P. Lappalainen, *Actin stress fibers - assembly, dynamics and biological roles.* Journal of Cell Science, 2012. **125**(8): p. 1855-1864.
22. Lodish H, B.A., Zipursky SL, in *Molecular Cell Biology. 4th edition*. 2000.
23. Sellers, J.R. and S.M. Heissler, *Nonmuscle myosin-2 isoforms.* Current Biology, 2019. **29**(8): p. R275-R278.
24. Lee, H., et al., *Passive and active microrheology for cross-linked F-actin networks in vitro.* Acta Biomater, 2010. **6**(4): p. 1207-18.
25. Bendix, P.M., et al., *A quantitative analysis of contractility in active cytoskeletal protein networks.* Biophysical Journal, 2008. **94**(8): p. 3126-3136.
26. Miller, C.J., et al., *Emergent mechanics of actomyosin drive punctuated contractions and shape network morphology in the cell cortex.* Plos Computational Biology, 2018. **14**(9): p. 1006344.
27. Wang, S.S. and P.G. Wolynes, *Active contractility in actomyosin networks.* Proceedings of the National Academy of Sciences of the United States of America, 2012. **109**(17): p. 6446-6451.
28. Malik-Garbi, M., et al., *Scaling behaviour in steady-state contracting actomyosin networks.* Nature Physics, 2019. **15**(5): p. 509-+.
29. Linsmeier, I., et al., *Disordered actomyosin networks are sufficient to produce cooperative and telescopic contractility.* Nature Communications, 2016. **7**: p. 12615.
30. Guo, M., et al., *Probing the stochastic, motor-driven properties of the cytoplasm using force spectrum microscopy.* Cell, 2014. **158**(4): p. 822-832.
31. Hoffman, B.D., et al., *The consensus mechanics of cultured mammalian cells.* Proceedings of the National Academy of Sciences of the United States of America, 2006. **103**(27): p. 10259-10264.
32. Fakhri, N., et al., *High-resolution mapping of intracellular fluctuations using carbon nanotubes.* Science, 2014. **344**(6187): p. 1031-1035.
33. Oakley, J.G., A.J. Giacomin, and J.A. Yosick, *Molecular origins of nonlinear viscoelasticity.* Mikrochimica Acta, 1998. **130**(1-2): p. 1-28.
34. Wirtz, D., *Particle-Tracking Microrheology of Living Cells: Principles and Applications.* Annual Review of Biophysics, 2009. **38**: p. 301-326.
35. Waigh, T.A., *Microrheology of complex fluids.* Reports on Progress in Physics, 2005. **68**(3): p. 685-742.
36. Mansel, B.W., et al., *Zooming in: Structural Investigations of Rheologically Characterized Hydrogen-Bonded Low-Methoxyl Pectin Networks.* Biomacromolecules, 2015. **16**(10): p. 3209-3216.
37. Einstein, A., *The theory of the Brownian Motion.* Annalen Der Physik, 1906. **19**(2): p. 371-381.
38. Lau, A.W.C., et al., *Microrheology, stress fluctuations, and active behavior of living cells.* Physical Review Letters, 2003. **91**(19): p. 198101.
39. Massiera, G., et al., *Mechanics of single cells: rheology, time dependence, and fluctuations.* Biophys J, 2007. **93**(10): p. 3703-13.

40. Wei, M.T., et al., *A comparative study of living cell micromechanical properties by oscillatory optical tweezers.* Optics Express, 2008. **16**(12): p. 8594-8603.
41. Smith, B.A., et al., *Probing the viscoelastic behavior of cultured airway smooth muscle cells with atomic force microscopy: Stiffening induced by contractile agonist.* Biophysical Journal, 2005. **88**(4): p. 2994-3007.
42. Hecht, F.M., et al., *Imaging viscoelastic properties of live cells by AFM: power-law rheology on the nanoscale.* Soft Matter, 2015. **11**(23): p. 4584-4591.
43. Kilpatrick, J.I., I. Revenko, and B.J. Rodriguez, *Nanomechanics of Cells and Biomaterials Studied by Atomic Force Microscopy.* Advanced Healthcare Materials, 2015. **4**(16): p. 2456-2474.
44. Li, M., et al., *Atomic Force Microscopy in Characterizing Cell Mechanics for Biomedical Applications: A Review.* Ieee Transactions on Nanobioscience, 2017. **16**(6): p. 523-540.
45. Lin, Y.C., et al., *Probing cellular traction forces with magnetic nanowires and microfabricated force sensor arrays.* Nanotechnology, 2012. **23**: p. 075101.
46. Hoffman, B.D. and J.C. Crocker, *Cell mechanics: dissecting the physical responses of cells to force.* Annu Rev Biomed Eng, 2009. **11**: p. 259-88.
47. Condeelis, J.S. and D.L. Taylor, *The contractile basis of amoeboid movement. V. The control of gelation, solation, and contraction in extracts from Dictyostelium discoideum.* J Cell Biol, 1977. **74**(3): p. 901-27.
48. Janmey, P.A., et al., *Resemblance of actin-binding protein actin gels to covalently cross-linked networks.* Nature, 1990. **345**(6270): p. 89-92.
49. Ingber, D.E., *Cellular tensegrity: defining new rules of biological design that govern the cytoskeleton.* J Cell Sci, 1993. **104 (Pt 3)**: p. 613-27.
50. Ingber, D.E., *Tensegrity I. Cell structure and hierarchical systems biology.* J Cell Sci, 2003. **116**(Pt 7): p. 1157-73.
51. Sollich, P., et al., *Rheology of soft glassy materials.* Physical Review Letters, 1997. **78**(10): p. 2020-2023.
52. Sollich, P., *Rheological constitutive equation for a model of soft glassy materials.* Phys Rev E, 1998. **58**(1): p. 738-759.
53. Bausch, A.R. and K. Kroy, *A bottom-up approach to cell mechanics.* Nature Physics, 2006. **2**(4): p. 231-238.
54. Hwang, H.J., R.A. Riggleman, and J.C. Crocker, *Understanding soft glassy materials using an energy landscape approach.* Nature Materials, 2016. **15**(9): p. 1031-1036.
55. Alcaraz, J., et al., *Microrheology of human lung epithelial cells measured by atomic force microscopy.* Biophysical Journal, 2003. **84**(3): p. 2071-2079.
56. Desprat, N., et al., *Creep function of a single living cell.* Biophysical Journal, 2005. **88**(3): p. 2224-2233.
57. Balland, M., A. Richert, and F. Gallet, *The dissipative contribution of myosin II in the cytoskeleton dynamics of myoblasts.* European Biophysics Journal with Biophysics Letters, 2005. **34**(3): p. 255-261.
58. Deng, L.H., et al., *Fast and slow dynamics of the cytoskeleton.* Nature Materials, 2006. **5**(8): p. 636-640.
59. Lenormand, G., et al., *Linearity and time-scale invariance of the creep function in living cells.* Journal of the Royal Society Interface, 2004. **1**(1): p. 91-97.

60. Mizuno, D., et al., *Nonequilibrium mechanics of active cytoskeletal networks.* Science, 2007. **315**(5810): p. 370-373.
61. MacKintosh, F.C. and A.J. Levine, *Nonequilibrium mechanics and dynamics of motor-activated gels.* Phys Rev Lett, 2008. **100**(1): p. 018104.
62. Gardel, M.L., et al., *Elastic behavior of cross-linked and bundled actin networks.* Science, 2004. **304**(5675): p. 1301-5.
63. Gardel, M.L., et al., *Prestressed F-actin networks cross-linked by hinged filamins replicate mechanical properties of cells.* Proceedings of the National Academy of Sciences of the United States of America, 2006. **103**(6): p. 1762-1767.
64. MacKintosh, F.C. and A.J. Levine, *Nonequilibrium mechanics and dynamics of motor-activated gels.* Physical Review Letters, 2008. **100**(1): p. 018104.
65. Morse, D.C., *Viscoelasticity of concentrated isotropic solutions of semiflexible polymers. 2. Linear response.* Macromolecules, 1998. **31**(20): p. 7044-7067.
66. Hoffman, B.D. and J.C. Crocker, *Cell mechanics: dissecting the physical responses of cells to force.* Annual Review of Biomedical Engineering, 2009. **11**: p. 259-288.
67. Frette, V., et al., *Avalanche dynamics in a pile of rice.* Nature, 1996. **379**(6560): p. 49-52.
68. Gutenberg, B. and C.F. Richter, *Magnitude and Energy of Earthquakes.* Nature, 1955. **176**(4486): p. 795-795.
69. Alencar, A.M., et al., *Non-equilibrium cytoquake dynamics in cytoskeletal remodeling and stabilization.* Soft Matter, 2016. **12**(41): p. 8506-8511.
70. Plotnikov, S.V., et al., *High-Resolution Traction Force Microscopy.* Quantitative Imaging in Cell Biology, 2014. **123**: p. 367-394.
71. Tan, J.L., et al., *Cells lying on a bed of microneedles: an approach to isolate mechanical force.* Proc. Natl. Acad. Sci. U. S. A., 2003. **100**(4): p. 1484-1489.
72. Fu, J., et al., *Mechanical regulation of cell function with geometrically modulated elastomeric substrates.* Nat Methods, 2010. **7**(9): p. 733-6.
73. Sniadecki, N.J., et al., *Magnetic microposts as an approach to apply forces to living cells.* Proceedings of the National Academy of Sciences of the United States of America, 2007. **104**(37): p. 14553-14558.
74. Tanase, M., et al., *Magnetic alignment of fluorescent nanowires.* Nano Letters, 2001. **1**(3): p. 155-158.
75. Kramer, C., *Probing the dynamics of cellular traction forces with magnetic and non-magnetic micropost arrays*. 2009, Johns Hopkins University.
76. Hultgren, A., et al., *High-yield cell separations using magnetic nanowires.* IEEE Transactions on Magnetics, 2004. **40**(4): p. 2988-2990.
77. Hultgren, A., et al., *Optimization of yield in magnetic cell separations using nickel nanowires of different lengths.* Biotechnology Progress, 2005. **21**(2): p. 509-515.
78. Fu, J.P., et al., *Mechanical regulation of cell function with geometrically modulated elastomeric substrates.* Nature Methods, 2010. **7**(9): p. 733-736.
79. Weng, S. and J. Fu, *Synergistic regulation of cell function by matrix rigidity and adhesive pattern.* Biomaterials, 2011. **32**(36): p. 9584-93.
80. Cheng, Q., et al., *PDMS elastic micropost arrays for studying vascular smooth muscle cells.* Sensors and Actuators B-Chemical, 2013. **188**: p. 1055-1063.
81. Crocker, J.C. and D.G. Grier, *Methods of digital video microscopy for colloidal studies.* Journal of Colloid and Interface Science, 1996. **179**(1): p. 298-310.

82. Sniadecki, N.J., et al., *Magnetic microposts for mechanical stimulation of biological cells: Fabrication, characterization, and analysis.* Review of Scientific Instruments, 2008. **79**(4): p. 044302.
83. Sniadecki, N.J., et al., *Magnetic microposts as an approach to apply forces to living cells.* Proceedings of the National Academy of Sciences, 2007. **104**(37): p. 14553-14558.
84. Massiera, G., et al., *Mechanics of single cells: Rheology, time dependence, and fluctuations.* Biophysical Journal, 2007. **93**(10): p. 3703-3713.
85. Dixon, P.K. and L. Wu, *Broad-band digital lock-in amplifier techniques.* Review of Scientific Instruments, 1989. **60**(10): p. 3329-3336.
86. Bevington, P.R., *Data Reduction and Error Analysis for the Physical Sciences*. 1969, New York: McGraw-Hill.
87. Guo, M., et al., *Probing the stochastic, motor-driven properties of the cytoplasm using force spectrum microscopy.* Cell, 2014. **158**: p. 822-832.
88. Shi, Y., et al., *Dissecting fat-tailed fluctuations in the cytoskeleton with active micropost arrays.* Proceedings of the National Academy of Sciences, 2019: p. 201900963.
89. du Roure, O., et al., *Force mapping in epithelial cell migration.* Proceedings of the National Academy of Sciences, 2005. **102**(7): p. 2390-2395.
90. Geng, Y.X. and Z.J. Wang, *Review of cellular mechanotransduction on micropost substrates.* Medical & Biological Engineering & Computing, 2016. **54**(2-3): p. 249-271.
91. Wolfenson, H., et al., *Tropomyosin controls sarcomere-like contractions for rigidity sensing and suppressing growth on soft matrices.* Nature Cell Biology, 2016. **18**(1): p. 33-42.
92. Rigato, A., et al., *High-frequency microrheology reveals cytoskeleton dynamics in living cells.* Nature Physics, 2017. **13**(8): p. 771-775.
93. Caspi, A., R. Granek, and M. Elbaum, *Enhanced diffusion in active intracellular transport.* Physical Review Letters, 2000. **85**(26): p. 5655-5658.
94. Yamada, S., D. Wirtz, and S.C. Kuo, *Mechanics of living cells measured by laser tracking microrheology.* Biophysical Journal, 2000. **78**(4): p. 1736-1747.
95. Mak, M., R.D. Kamm, and M.H. Zaman, *Impact of Dimensionality and Network Disruption on Microrheology of Cancer Cells in 3D Environments.* Plos Computational Biology, 2014. **10**(11): p. e1003959.
96. Robert, D., et al., *In vivo determination of fluctuating forces during endosome trafficking using a combination of active and passive microrheology.* PloS one, 2010. **5**(4): p. e10046.
97. Wyart, M., *Marginal stability constrains force and pair distributions at random close packing.* Physical Review Letters, 2012. **109**(12): p. 125502.
98. Held, G.A., et al., *Experimental-study of critical-mass fluctuations in an evolving sandpile.* Physical Review Letters, 1990. **65**(9): p. 1120-1123.
99. Nicolas, A., et al., *Deformation and flow of amorphous solids: An updated review of mesoscale elastoplastic models.* 2017: p. ArXiv1708.09194.
100. Ferrero, E.E., K. Martens, and J.L. Barrat, *Relaxation in Yield Stress Systems through Elastically Interacting Activated Events.* Physical Review Letters, 2014. **113**(24): p. 248301.

101. Puig-de-Morales, M., et al., *Cytoskeletal mechanics in adherent human airway smooth muscle cells: probe specificity and scaling of protein-protein dynamics.* American Journal of Physiology-Cell Physiology, 2004. **287**(3): p. C643-C654.
102. Gittes, F., et al., *Microscopic viscoelasticity: Shear moduli of soft materials determined from thermal fluctuations.* Physical Review Letters, 1997. **79**(17): p. 3286-3289.
103. Gisler, T. and D.A. Weitz, *Scaling of the microrheology of semidilute F-actin solutions.* Physical Review Letters, 1999. **82**(7): p. 1606-1609.
104. Palmer, A., et al., *Diffusing wave spectroscopy microrheology of actin filament networks.* Biophysical Journal, 1999. **76**: p. 1063-1071.
105. Van Citters, K.M., et al., *The role of F-actin and myosin in epithelial cell rheology.* Biophysical journal, 2006. **91**(10): p. 3946-3956.
106. Gerhardt, M., et al., *Actin and PIP3 waves in giant cells reveal the inherent length scale of an excited state.* Journal of Cell Science, 2014. **127**(20): p. 4507-4517.
107. Inagaki, N. and H. Katsuno, *Actin waves: Origin of cell polarization and migration?* Trends in Cell Biology, 2017. **27**(7): p. 515-526.
108. Giannone, G., et al., *Periodic lamellipodial contractions correlate with rearward actin waves.* Cell, 2004. **116**(3): p. 431-443.
109. Zaburdaev, V., S. Denisov, and J. Klafter, *Levy walks.* Reviews of Modern Physics, 2015. **87**(2): p. 483-530.
110. Harris, T.H., et al., *Generalized Levy walks and the role of chemokines in migration of effector CD8(+) T cells.* Nature, 2012. **486**(7404): p. 545-549.
111. Phillies, G.D.J., *In complex fluids the Gaussian Diffusion Approximation is generally invalid.* Soft Matter, 2015. **11**(3): p. 580-586.
112. Weron, R., *Levy-stable distributions revisited: Tail index > 2 does not exclude the Levy-stable regime.* International Journal of Modern Physics C, 2001. **12**(2): p. 209-223.
113. Gutenberg, B. and C.F. Richter, *Frequency of earthquakes in California* Bulletin of the Seismological Society of America, 1944. **34**: p. 185-188.
114. Zargar, R., et al., *Direct measurement of the free energy of aging hard sphere colloidal glasses.* Physical Review Letters, 2013. **110**(25): p. 258301.
115. Lemaitre, A. and C. Caroli, *Rate-dependent avalanche size in athermally sheared amorphous solids.* Physical Review Letters, 2009. **103**(6): p. 065501.
116. Kelly, P.A. *Mechanics Lecture Notes: An Introduction to Solid Mechanics*. 2019; Available from: http://homepages.engineering.auckland.ac.nz/~pkel015/SolidMechanicsBooks/Part_I/index.html.
117. Ferry, J.D., *Viscoelastic properties of polymers*. 3rd ed. 1980, New York: Wiley.
118. Lohner, J., et al., *Large and reversible myosin-dependent forces in rigidity sensing.* Nature Physics, 2019: p. https://doi.org/10.1038/s41567-019-0477-9.
119. Nagaraju, C.K., et al., *Myofibroblast Phenotype and Reversibility of Fibrosis in Patients With End-Stage Heart Failure.* Journal of the American College of Cardiology, 2019. **73**(18): p. 2267-2282.
120. Thompson, S.A., et al., *Mechanical Coupling Between Myofibroblasts and Cardiomyocytes Slows Electric Conduction in Fibrotic Cell Monolayers.* Circulation, 2011. **123**(19): p. 2083-U71.

121. Ghibaudo, M., et al., *Traction forces and rigidity sensing regulate cell functions.* Soft Matter, 2008. **4**(9): p. 1836-1843.
122. Gupta, M., et al., *Single cell rigidity sensing: A complex relationship between focal adhesion dynamics and large-scale actin cytoskeleton remodeling.* Cell Adhesion & Migration, 2016. **10**(5): p. 554-567.
123. Chen, J., et al., *Parameter Estimation of Stable Distribution Based on Zero - order Statistics.* Green Energy and Sustainable Development I, 2017. **1864**.
124. Chakravarti, Laha, and Roy, *Handbook of Methods of Applied Statistics*. Vol. I. 1967: John Wiley and Sons. 392-394.
125. Doyle, A.D. and J. Lee, *Simultaneous, real-time imaging of intracellular calcium and cellular traction force production.* Biotechniques, 2002. **33**(2): p. 358-364.
126. Chazeau, A., et al., *Mechanical coupling between transsynaptic N-cadherin adhesions and actin flow stabilizes dendritic spines.* Molecular Biology of the Cell, 2015. **26**(5): p. 859-873.

List of Publications

1. Fan Xu, Ruogang Zhao, Alan S. Liu, Tristin Metz, **Yu Shi**, Pransenjit Bose, Daniel H. Reich, "A microfabricated magnetic actuation device for mechanical conditioning of arrays of 3D microtissues." Lab Chip 15(11) (2015) 2496-2503.
2. **Yu Shi**, Christopher L. Porter, John C. Crocker, Daniel H. Reich: "Dissecting fat-tailed fluctuations in the cytoskeleton with active micropost arrays", PNAS 2019 116 (28) 13839-13846 (2019)
3. **Yu Shi**, Katherine Xiang, Shankar Sivarajan, John C. Crocker, Daniel H. Reich: "The role of substrate stiffness and cellular phenotype in the dynamic fluctuations of cellular actomyosin networks." (in preparation)
4. Geran Kostecki, **Yu Shi**, Shoshana Das, Daniel H. Reich, Christopher Chen, Leslie Tung: "Optogenetic currents in myofibroblasts produce acute changes in electrophysiology of cocultured myocytes." (in preperation)
5. Seungman Park, **Yu Shi**, Byoung Chul Kim, Myung Hyun Jo, Zheming Gou, Taekjip Ha, Li-Fan Lu, Daniel H. Reich, Yun Chen: "Force-Dependent Trans-endocytosis by Breast Cancer Cells Depletes Costimulatory Receptor CD80 and Attenuates T Cell Activation" (in preperation)

Appendix

Passive microrheology imaging protocol

1. Remove air bubbles underneath micropost substrates by taking substrates out of media and put back into culture dish 3 times.
2. Turn on microscope stage heating plate to 37 °C.
3. Use 10 X objective and phase ring to get the micropost substrates in focus.
4. Follow the Kohler illumination steps to focus and center the light path: minimize the field diaphragm size and get the condenser in focus and centered, then increase the field diaphragm size to cover the entire field of view.
5. Maximize the condenser aperture diaphragm size to maximize image resolution.
6. Rotate the substrate as needed to align microposts horizontally
7. Apply on-stage environmental chamber and turn on pre-mixed CO_2 gas
8. Switch to 40X objective, apply IR and UV filters, remove condenser phase ring
9. Switch light path to camera. In Norpix, set camera gain to be 0, and exposure time to 4,500 μs for 100 fps and 45,000 μs for 10 fps measurements.
10. Adjust light intensity to maximize illumination without over-saturating the image (use histogram module in Norpix to help)
11. Adjust the working distance of the 40X objective with its collar while keep the image in focus, until the minimum background intensity is reached.(can be referred to the peak in the histogram). Repeat step 10 every time the working distance of the objective is changed.

12. Turn off illumination and leave microposts on the microscope for 10-15 minutes to allow the temperature and CO_2 level to stabilize.
13. Record cells on microposts for 30 minutes (or other amount of time depending on the experiment)

Active microrheology imaging protocol

1. Leave the dual magnetic tweezer set up inside the on-stage incubator overnight to allow it to heat up to 37 °C.
2. Put micropost substrate inside the sample chamber of the customized dish
3. Fill dish with 2 mL of CO_2 independent media, close the lid carefully, and cover the dish with a PDMS ring to prevent media evaporation
4. Adjust the pole tips' position of the dual magnetic tweezer in the x-y plane until the two tips are located at approximately 1/4 and 3/4 of the way along the x axis of the field of view with a 10 X objective lens. (at 40X magnification the magnetic tweezers' tips will appear at the edge of the field of view)
5. Put the sample dish carefully underneath the two magnetic tweezers, and keep the magnetic tweezers tips 0.8 mm above the microposts' top. (this can be achieved by using the focal plane positions shown on the control panel for the microscope)
6. Repeat steps 3-12 from passive microrheology imaging to optimize image quality.
7. Load the "VoltageOutNin_sync_DF" module in Norpix
8. Edit scripts in "Tools"- "edit scripts": insert command "start" at event "post create AVI", insert command "increment" at event "frames saved" and insert command

"end" at event "recording stopped". These commands are under "DemoModule" group and can be reloaded after saving the scripts.

9. Go to streampix setting, enable "auto naming for new videos" in the "auto name" panel and load the recording script named "synchronizedscript" in the "recording rate" panel.
10. Turn on the Kepco BOP power supply for driving the magnetic tweezer and the power supply for the Hall sensor. Find an appropriate cell with magnetic microposts underneath (defects in micropost array can be used as reference).
11. Start recording, the script will run through a frequency sweep from 0.1 Hz to 135 Hz. The whole process will take approximately 30 minutes.
12. Remove the cells by applying trypsin to the sample for 10 minutes. Wash the substrate with PBS 3 times.
13. Go back to the same field of view and measure the microposts' rheology after cell removal.
14. Rinse the sample dish with ethanol 3 times to wash off remaining PBS in the dish, then transfer into UV cabinet for 30 minutes for sterilization.

Vita

Yu Shi was born in Dec 12th, 1989 in Wuhan, China to Mr. Genhuo Shi and Mrs. Hong Wang. He attended University of Science and Technology of China at Hefei, China for his undergraduate studies, where he graduated summa cum laude with a B.S. in Physics in May 2012. He attended Johns Hopkins University for his graduate studies where he received his M.S. in Physics in 2015, the Certificate of Advanced Study in Nano-Biotechnology in 2017, and his Ph.D. in 2020.